

# Crystallization in Confinement

Fiona C. Meldrum\* and Cedrick O'Shaughnessy

Many crystallization processes of great importance, including frost heave, biomineralization, the synthesis of nanomaterials, and scale formation, occur in small volumes rather than bulk solution. Here, the influence of confinement on crystallization processes is described, drawing together information from fields as diverse as bioinspired mineralization, templating, pharmaceuticals, colloidal crystallization, and geochemistry. Experiments are principally conducted within confining systems that offer well-defined environments, varying from droplets in microfluidic devices, to cylindrical pores in filtration membranes, to nanoporous glasses and carbon nanotubes. Dramatic effects are observed, including a stabilization of metastable polymorphs, a depression of freezing points, and the formation of crystals with preferred orientations, modified morphologies, and even structures not seen in bulk. Confinement is also shown to influence crystallization processes over length scales ranging from the atomic to hundreds of micrometers, and to originate from a wide range of mechanisms. The development of an enhanced understanding of the influence of confinement on crystal nucleation and growth will not only provide superior insight into crystallization processes in many real-world environments, but will also enable this phenomenon to be used to control crystallization in applications including nanomaterial synthesis, heavy metal remediation, and the prevention of weathering.

## 1. Introduction

Crystallization is a hugely important phenomenon that underpins processes as diverse as the production of nanomaterials, ceramics, and pharmaceuticals, the generation of bones, teeth, and seashells, ice formation and weathering in our environment, and the formation of scale in kettles and oil wells. Significant efforts are therefore made to understand how crystals nucleate and grow in order to develop strategies to control fundamental properties such as size, shape, and polymorph, and to inhibit or promote crystallization as desired.<sup>[1–10]</sup> Given the challenges associated with this goal, text book descriptions of


crystallization predominantly focus on simple models, such as crystal nucleation on perfect planar surfaces and in bulk solutions. Yet, the reality is that few crystallization processes occur in such idealized environments.

A common feature of many real-world crystallization processes is that they occur within small volumes rather than bulk solutions. Crystallization within porous media such as rocks and construction materials can lead to weathering and decay,<sup>[11,12]</sup> and offers a strategy for contaminant sequestration and remediation.<sup>[13–15]</sup> Biomineralization, a phenomenon that delivers remarkable structures such as bones and seashells, invariably occurs within confined volumes,<sup>[16–19]</sup> while many strategies for synthesizing nanomaterials rely on hard and soft templates to define size and shape.<sup>[9,20–24]</sup> Descriptions of crystallization within confined volumes are therefore distributed across the literature in relation to fields as diverse as pharmaceuticals, ice nucleation, protein crystallography, nucleation kinetics, nanomaterial synthesis, biomineralization, and nanogeochemistry.

Here, we present a review of the effects of confinement on crystallization—and the origins of these—where our goal has been to create a comprehensive picture of this phenomenon by bringing together information from these diverse fields. Together, these demonstrate that confinement can influence factors including nucleation rates, melting and freezing points, as well as crystal polymorph, size, morphology, and orientation. Effects operate over multiple length scales ranging from the atomic, such as in carbon nanotubes, through to hundreds of micrometers, as offered by droplet-based systems. The confining volumes can also provide a wide range of geometries, where systems comprising isolated volumes range from spherical droplets, to the cylindrical pores in anodic alumina and track-etched membranes, to the wedge-shaped pockets formed at the step edges on mica. Crystallization within a uniform network of pores can be studied using porous glasses and polymers, and media such as colloidal crystals. Given the huge interest in crystallization within rocks and building materials, a large volume of literature has also addressed crystallization within these heterogeneous porous media.

Building an understanding of the influence of confinement on crystallization is also dependent on being able to characterize the crystals either *ex situ* following their isolation from the confining medium, or ideally *in situ*, where techniques employed include microscopy and tomography-based methods, calorimetry,

Prof. F. C. Meldrum, Dr. C. O'Shaughnessy  
School of Chemistry  
University of Leeds  
Woodhouse Lane, Leeds LS2 9JT, UK  
E-mail: F.Meldrum@leeds.ac.uk

 The ORCID identification number(s) for the author(s) of this article can be found under <https://doi.org/10.1002/adma.202001068>.

© 2020 The Authors. Published by WILEY-VCH Verlag GmbH & Co. KGaA, Weinheim. This is an open access article under the terms of the Creative Commons Attribution License, which permits use, distribution and reproduction in any medium, provided the original work is properly cited.

DOI: 10.1002/adma.202001068

NMR, and X-ray and neutron diffraction. Finally, crystallization is a dynamic phenomenon, and is governed by the transport of material to the growing crystals. In order to create a truly comprehensive understanding of crystallization in these systems one also needs to determine the composition of the solution in the vicinity of growing crystals as a function of time.

Given the scope of the topic of crystallization in confinement, this review is not intended to be exhaustive, but instead provides the reader with a description of the salient topics and offers a gateway to the literature. Our definition of confinement is an environment that changes the kinetics or thermodynamics of crystallization by restricting the dimensions of the system in one, two, or three directions. As nucleation is almost always heterogeneous in nature, we do not consider the formation of crystals on a planar substrate to be confined. A focus is placed on systems that offer well-defined environments, where these ideally also provide the opportunity for systematic investigation of confinement effects, and studies that are purely synthetic in nature are excluded. Indeed, one of the challenges of studying crystallization in confinement is in identifying systems that meet these criteria. We also exclude investigations of the crystallization of polymers and liquid crystals, where these are extensive topics in their own right.

The article begins with a summary of the principal effects of confinement on crystallization, where this brings together evidence from systems with contrasting length scales and geometries. It is then structured into sections that address these systems in detail. The first of these describes the striking effects of confinement on crystal growth, where we show that growth of crystals within structured templates can lead to remarkable, noncrystallographic forms. We then consider the influence of confinement on freezing and melting phenomena, where this field provides some of the earliest evidence of confinement effects. Easy to create and study, and offering well-defined finite volumes, droplet-based environments have been extensively used to study nucleation processes and provide a valuable insight into the origin of many confinement effects. We then describe confining systems of increasing geometrical complexity including cylindrical pores, mesoporous solids, wedge-shaped pores, and manufactured reaction chambers, where these demonstrate how effects operate over different length scales and geometries. This is followed by an overview of crystallization within heterogeneous porous media, where this is offered from the perspective of the geosciences, and we finish with a description of the crystallization of colloidal particles in constrained volumes, where this can provide valuable insight into the behavior of crystals of atomic and molecular species.

Together, these studies demonstrate how investigation of confinement effects on crystallization can lead to an enhanced understanding of phenomena such as weathering and biomineralization, where in the latter case the emphasis is typically placed on the role of soluble additives in directing mineralization. Elucidation of confinement effects will also enable this strategy to be used to control crystallization processes, where this has a potential impact on topics including nanomaterial synthesis, heavy metal remediation, and the prevention of weathering. Finally, we can also exploit confinement to gain a superior understanding of nucleation and growth processes, and the factors that influence these in real-world environments.



**Fiona Meldrum** obtained her undergraduate degree from the University of Cambridge and her doctorate from the University of Bath. She held postdoctoral positions at the University of Syracuse, USA and the Max Plank Institute of Polymerforschung before joining the Australian National University as a Research Fellow. She took

up a lectureship at Queen Mary, University of London in 1998 and moved to the University of Bristol in 2003 and the University of Leeds in 2009. Her research focuses on crystallization, with particular emphasis on bio-inspired crystallization.



**Cedrick O'Shaughnessy** received a B.S. and an M.S. in earth and planetary sciences at McGill University after which he completed a Ph.D. in earth sciences from the University of Toronto. He is currently a Postdoctoral Research Fellow in the School of Chemistry at the University of Leeds. He is part of the Crystallization in

the Real World research consortium focused on bringing together insights from modelling and experimental work. His current research is focused on the crystallization of inorganic compounds in nanoporous media with an emphasis on crystal morphology, polymorph control, and the influence of pore surface chemistry.

## 2. Summary of the Effects of Confinement on Crystallization

Insight into the effects of confinement on crystallization has been gained from diverse systems offering length scales varying from the nanoscale to hundreds of micrometers, and geometries including sponge-like networks of pores and finite droplets. A wide range of compounds have also been studied including small organics, macromolecules, metals, organic compounds and even colloidal particles. It is therefore unsurprising that many effects on crystal nucleation and growth have been observed, some of which are quite general, and others that are system-specific. These can be both kinetic and thermodynamic in origin, where it is important to note that for a given volume, the geometry of the confining medium and the interfacial energy between the crystal and confining medium will ultimately dictate the effect on crystallization. The goal of this section is to provide the reader with an overview of confinement effects on crystallization

and their potential mechanistic origins. In-depth consideration of individual systems is then presented in the bulk of the review.

### 2.1. Crystal Morphologies

Growth of a crystal within a rigid environment frequently leads to templating effects where the morphology of the crystal is defined by the mold. This is observed over multiple length scales and occurs when the size of the crystal formed under the solution conditions employed exceeds the dimensions of the template. In this way confinement has been used to generate single crystals with both simple and complex noncrystallographic morphologies (see Section 3).

### 2.2. Orientation

Crystallization of compounds with anisotropic structures within anisotropic environments often leads to preferred orientations. This is frequently observed in cylindrical pores and is attributed to competitive growth effects, where unimpeded growth is only possibly parallel to the pore axis. Those crystals oriented with their direction of rapid growth coincident with the pore axis therefore grow at the expense of crystals in other orientations (see Section 7.2.1).

### 2.3. Freezing/Melting Points

The freezing/melting points of compounds are typically depressed in small volumes. This phenomenon has been recognized since early last century, and is thus one of the best characterized effects of confinement on crystallization. Occurring in nanoscale pores, this is a thermodynamic effect that originates from the free energy difference between a liquid and solid in a pore, in systems where superior wetting of the pore is achieved by the liquid than the solid. Freezing typically occurs at a lower temperature than melting, where this is a kinetic effect due to the barrier associated with the formation of a nucleus of the solid phase (see Section 4).

### 2.4. Nucleation Rates

Nucleation in small volumes usually gives rise to a reduction in the nucleation rate, where this can be attributed to a number of factors. i) The creation of small volumes is typically associated with the exclusion of impurities that promote nucleation in bulk solution (see Section 5). Nucleation rates can therefore approach homogeneous rates, where it is of course impossible to eliminate all interfaces. This effect can be seen in finite volumes in the  $\mu\text{L}$  regime and below, provided that the number of droplets vastly exceeds the number of impurities present. ii) The probability of nucleation scales with volume, where a 10-fold reduction in the volume of a spherical droplets reduces the mean nucleation time by a factor of  $10^3$  (see Section 5.1). This kinetic effect is again observed in volumes in the  $\mu\text{L}$  to

nL regime and below. iii) The consumption of ions that accompanies the formation of a crystal nucleus within a small, finite volume gives rise to a continuous depletion of the supersaturation, and thus the driving force for formation of a critical nucleus. This can limit the size of a nucleus that can form, and can even prevent nucleation from solution supersaturations that would yield crystals in bulk solution (see Section 5.1). This thermodynamic effect becomes important in volumes in the pL size regime for soluble compounds, and smaller volumes for insoluble compounds with higher surface energies.

The geometry of the site in which nucleation occurs can also influence the nucleation rate. Simulations of nucleation within atomically sharp wedges have shown that the nucleation rate varies as function of the wedge angle, and is significantly enhanced at angles where an FCC crystal bounded by  $\{111\}$  planes ideally fits within the wedge (see Section 9.4). Wedge-shaped pores have been shown to support capillary condensation, and thus offer favorable sites for nucleation from vapor (see Section 9.3).

### 2.5. Crystal Structure and Polymorph

Arguably one of the most interesting effects of confinement on crystallization is on the structures of the crystals formed and the stabilization of different polymorphs. While polymorph must be defined at nucleation, it is intriguing that effects are seen at length scales far exceeding those of a critical nucleus. Influence over crystal structure and polymorph has therefore been attributed to many factors, depending on the size and geometry of the confining environment and the compound studied.

Crystallization under extreme confinement can have a number of effects on crystal structures. The crystallization of simple inorganic compounds within inorganic nanotubes that have diameters of just a few nanometers can give rise to materials with modified (e.g., distorted) structures, polymorphs that are not seen under analogous bulk conditions, and even new crystal structures. These structural changes can be attributed to the interactions of the atoms within the nanotube with those atoms in the nanotube wall, and those in the melt outside the nanotube (see Section 7.1). As an interesting model system, the effects of extreme confinement can be readily studied in colloidal systems, where an evolution of crystal structures that yield optimal packing densities in the confined volume can be observed when the confining environments fall in the same size regime as the constituent particles (see Section 12).

Organic compounds in contrast—which usually have larger critical nuclei than simple inorganics—often fail to crystallize within very small pores and precipitate in an amorphous form (that lacks long-range order). They also frequently show a strong pore-size dependence on the polymorph formed. As different polymorphs can form critical nuclei of different sizes, and some compounds even exhibit a reversal in polymorph stability at small crystal sizes, crystallization within small pores can be used to select polymorph. The surface chemistry of the confining medium undoubtedly also plays a role in selecting polymorph during crystallization from solution. This has been observed in pores that are tens of nanometers in diameter,

where the effect was attributed to the influence of the surface on the distribution of ions in the pores (see Section 7.2.3).

As a thermodynamic effect on crystallization, selection of the most stable polymorph has been achieved by performing crystallization within finite volumes (emulsions) that contain just enough ions to form a critical nucleus. Since a more stable polymorph is less soluble than a polymorph of lower thermodynamic stability, and therefore grows to a larger size before the supersaturation is depleted, it is possible to select conditions that gives rise to nuclei of the stable polymorph only (see Section 6.1).

A number of kinetic effects can also contribute to polymorph selectivity in confinement, where this is evidenced by the stabilization of metastable polymorphs of inorganic compounds between surfaces separated by hundreds of nanometers (see Sections 7.2.2 and 9.2). The reduced diffusion rates within small pores can lead to slow kinetics, which can influence the first polymorph formed, as well as causing a slow conversion between polymorphs, and thus stabilization of metastable phases (see Section 7.2.2). An additional effect of confined volumes is that they can support the development of extremely high supersaturations due to the elimination of impurities, or by creating an environment in which the supersaturation evolves over time. The latter leads to the concept of a supersaturation threshold, which is kinetic in origin and is defined as the metastability limit that can be achieved under the specific reaction conditions (see Section 11). Very high supersaturations can be achieved which often give rise to the formation of metastable polymorphs (see Section 5.2). These effects are active even in large length-scale systems such as droplets and porous media.

## 2.6. Influence of Crystallization on the Confining Medium

Crystallization can also affect the medium in which crystals grow. This is well-known in the weathering of rocks and building materials, where a growing crystal can exert a so-called “crystallization pressure” on the pore walls and ultimately lead to fracture. This phenomenon is dependent on their being a liquid film between the crystals and pore walls, which is determined by the solution/crystal, solution/pore, and crystal/pore interfacial energies. To support crystal growth the thin film must also be supersaturated with respect to the adjacent crystal faces (see Section 11). The presence of a thin film at the interface between a crystal and the pore wall has also been identified in many systems studying freezing/melting in porous media (see Section 4).

## 2.7. Material Transport in Confined Media

Nucleation and growth processes necessarily depend on the transport of material to the developing crystal. While transport in bulk solution is principally via advection and convection, these processes are suppressed in small volumes such that diffusion is typically the dominant transport mechanism in volumes of  $\approx 10 \mu\text{m}$ . This can again result in an increase in induction times and a reduction in growth rates in confined systems as compared with bulk solutions, where this will also

depend on the geometry and dimensions of the confining medium. Transport through confined media, and the evolution of solution compositions during crystallization in confinement is typically very difficult to measure experimentally (see Sections 10.3 and 11).

## 3. Controlling Crystal Morphologies

One of the most obvious effects of confinement on crystallization processes is on crystal morphologies. While polycrystalline structures can readily exhibit a wide range of shapes, single crystals characteristically exhibit morphologies that reflect the structure of the crystal lattice.<sup>[20]</sup> Provided that the “natural” size of a crystal under the given growth conditions exceeds the length scale of the template, confined volumes will alter crystal morphologies and can give rise to forms that bear no resemblance to the crystals formed in bulk solution. Templates that offer nanoscale confinement have therefore been widely used to impose morphologies on single crystals. Simple structures such as nanorods can be generated within the cylindrical pores of anodic alumina oxide (AAO) membranes and track-etched membranes, where single crystals can form as a result of competitive growth (see Section 7.2). A range of more complex nanoscale templates have also been employed such as colloidal crystals<sup>[25–28]</sup> and mesoporous silica.<sup>[29,30]</sup>

The effects of confinement on crystal morphologies can be nicely illustrated with examples from the calcium carbonate system, where, with the production of biominerals, nature demonstrates that it is possible to create large single crystals of calcite with complex morphologies. This is beautifully exemplified by the skeletal elements of sea urchins, which exhibit a unique sponge-like, fenestrated structure, comprising continuous macropores of diameter  $15 \mu\text{m}$  and noncrystallographic curved surfaces. Profiting from the bicontinuous structure of this biomineral, a polymer replica was formed by infiltrating a section of the urchin test with a polymer monomer, curing and dissolving away the calcium carbonate (**Figure 1a,b**).<sup>[31,32]</sup> This polymer replica was then used as an environment in which to grow calcite crystals *de novo*. The structures of the crystals produced were strongly dependent on the solution supersaturation. While polycrystalline calcite particles were produced at high supersaturations (**Figure 1c**), low supersaturations yielded  $100\text{--}200 \mu\text{m}$  single crystals that perfectly replicated the morphology of the original sea urchin plate (**Figure 1d**). The surfaces in contact with the template were curved, while planar faces were present at the unrestricted growth front. This work therefore demonstrates that single crystals of calcite with complex form can be produced in the absence of additives, by external imposition of morphology.

The influence of the surface chemistry of the template was also investigated by coating the polymer with a thin layer of gold using electroless deposition, and further functionalizing with  $\omega$ -terminated thiols, or by plasma-treatment followed by adsorption of polyelectrolytes.<sup>[33]</sup> Hydrophobic methyl-terminated self-assembled monolayers (SAMs) and positively-charged surfaces supported the growth of templated single crystals identical to those formed in the native polymer template, while slightly smaller crystals formed in the presence of

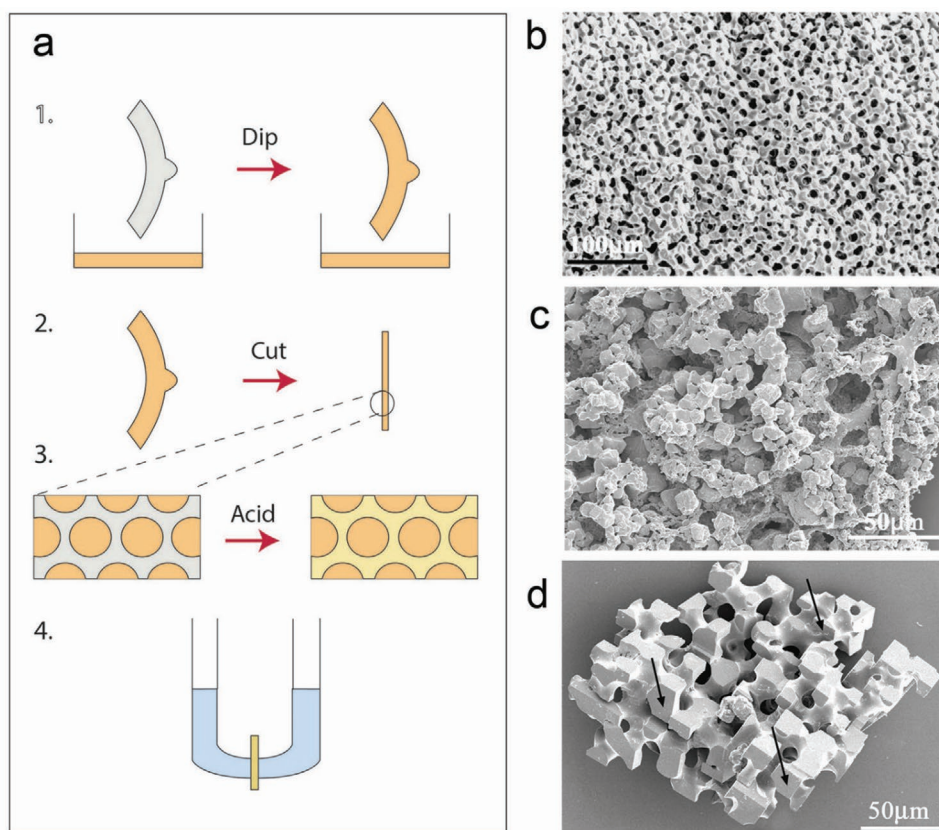


**Figure 1.** a) Schematic diagram describing the method used to template calcite crystals. 1: Urchin plate is dipped in polymer monomer and cured. 2: A thin section is cut. 3: The section is exposed to acid to remove the  $\text{CaCO}_3$ . 4:  $\text{CaCO}_3$  is precipitated within the polymer replica using a double diffusion setup. b) Cross section through a sea urchin skeletal plate. c) Polycrystalline calcite templated with 0.4 M reagents. d) Templated single crystal generated using 0.02 M reagents. a) Adapted with permission.<sup>[31]</sup> Copyright 2002, Wiley-VCH. b–d) Reproduced with permission.<sup>[31]</sup> Copyright 2002, Wiley-VCH.

hydroxyl-terminated SAMs. Negatively charged surfaces functionalized with carboxylic acid and sulfonic acid groups, in contrast, yielded polycrystalline particles. This strongly suggests that the formation of large, templated single crystals depends upon the existence of limited nucleation sites. In contrast, growth of  $\text{PbSO}_4$  and  $\text{SrSO}_4$  within the membranes—which also yields large, templated single crystals<sup>[34]</sup>—was independent of the surface chemistry. This could potentially be a supersaturation effect. While similar high initial supersaturations were used in all systems, calcium carbonate initially forms an amorphous calcium carbonate (ACC) phase. Subsequent crystallization then occurs via a dissolution/precipitation mechanism at a solution supersaturation defined by the solubility of the ACC phase. The influence of the surface is expected to be greater at this low supersaturation.

Effective morphological control can also be achieved by filling the template with ACC prior to crystallization.<sup>[27,35–38]</sup> This methodology is analogous to calcification mechanisms in many organisms, where it is now recognized that calcite and aragonite biominerals often form via the transformation of an ACC precursor phase.<sup>[39–42]</sup> This strategy was first employed using track-etched membranes as templates, where ACC was stabilized using a low temperature (4 °C) rather than soluble additives.<sup>[35,36]</sup> Calcite single crystals that replicated the shape of the pores were only achieved when ACC entirely filled the

pores prior to crystallization, where this was dependent on the pore size. Calcite single crystals with more complex morphologies were also generated by using vacuum filtration to fill a colloidal crystal of polystyrene (PS) spheres with ACC, allowing crystallization, and dissolving away the PS spheres (Figure 2a).<sup>[27]</sup> The resultant crystals exhibited dendritic external morphologies, but were internally patterned in the form of a reverse opal (Figure 2b,c). Notably, a subsequent article demonstrated that ACC is not essential to pattern calcite at these small length scales, where templating of colloidal crystals was achieved in the absence of significant quantities of a long-lived ACC cursor phase (Figure 2d–f).<sup>[25]</sup>

A final example of the use of confinement to template crystal morphologies is provided by a self-assembled polymer scaffold with a gyroid structure.<sup>[37]</sup> This template was created by adding a small amount of polystyrene (PS) homopolymer to a polystyrene-*b*-polyisoprene (PS-*b*-PI) block copolymer to create a thin film with a double gyroid structure of continuous PI channels in a PS matrix. Exposure of the sample to UV light partially degrades PI and crosslinks PS, and the PI can then be removed by washing with solvent (Figure 3a–d). This matrix was employed as a template for calcium carbonate, where ACC was imbibed into the structure (Figure 3e). Methanol was used to facilitate wetting, and also acted to stabilize the ACC phase. Calcite single crystals were subsequently isolated from the

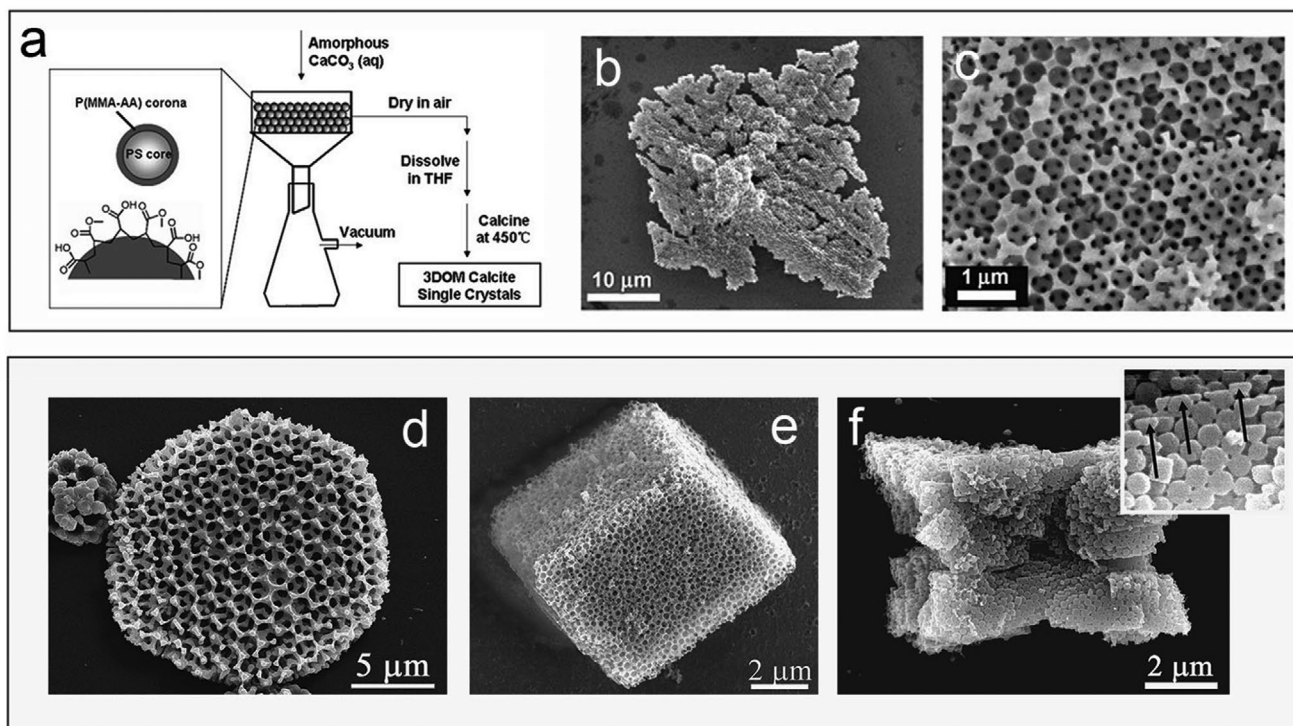


**Figure 2.** a) Schematic of method used to fabricate templated 3D ordered macroporous (3DOM) calcium carbonate crystals from an amorphous precursor. b,c) SEM images of 3DOM calcite single crystals formed from an ACC dispersion with a concentration of  $8 \times 10^{-3}$  M. a–c) Reproduced with permission.<sup>[27]</sup> Copyright 2008, Wiley-VCH. d,e) SEM images of calcite crystals precipitated within a colloidal crystal formed within a wedge with colloidal particles of sizes 1  $\mu\text{m}$  (d) and 200 nm (e). f) Calcite crystal precipitated within a reverse opal structure, where the inset shows a high-magnification image. d–f) Reproduced with permission.<sup>[25]</sup> Copyright 2011, Wiley-VCH.

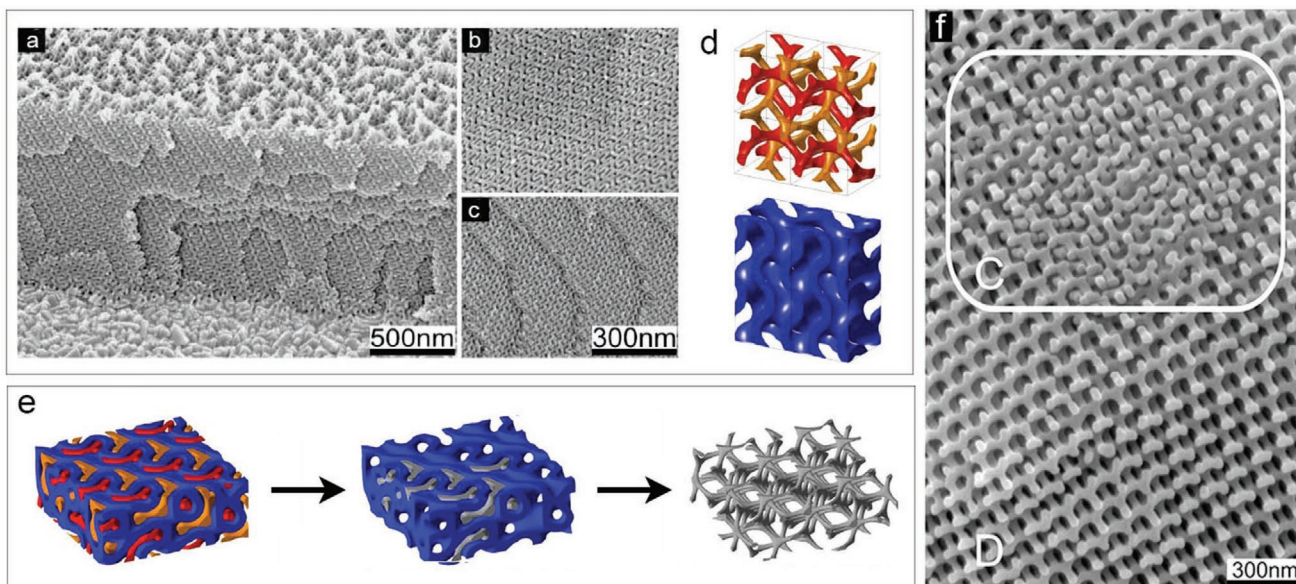


**Figure 3.** a) Cross-section of a patterned PS film showing the continuous matrix after PI removal, which exposes the two gyroid networks. b,c) High-magnification images of cross-sections through the porous PS film at the same magnification. d) The two intertwined, nonintersecting gyroid networks (PI, replicated by calcite). e) Schematic representation of the crystallization process. Left to right: films of the PS/PI copolymer self-assemble into a double-gyroid morphology. After removal of the two PI networks (red and orange) from the PS matrix (blue), calcium carbonate forms within the polymer film, leading to a gyroid-patterned single crystal. f) Examples of the replication of the full double gyroid (both networks) and just a single network, marked (C) and (D) respectively. a–f) Reproduced with permission.<sup>[37]</sup> Copyright 2009, Wiley-VCH.

polymer membrane and were shown to exhibit unique morphologies where crystals could either replicate just one, or both of the interpenetrating networks (Figure 3f). These structures therefore mimic the structure of sea urchin skeletal plates, but on a much smaller length scale.

#### 4. Effects of Confinement on Melting and Freezing

A large volume of experimental work has been conducted to investigate the effects of confinement on freezing and melting transitions, where this has been described in detail in a number of review articles.<sup>[43–46]</sup> Capillary condensation of liquid from undersaturated vapor is described by the Kelvin equation

$$r = -\frac{\gamma_{lv}v_m}{kT \ln [p/p_0]} \quad (1)$$

where  $\gamma_{lv}$  is surface tension of the liquid vapor interface,  $v_m$  is the molecular volume of the liquid,  $p$  is the actual vapor pressure, and  $p_0$  is the saturated vapor pressure above a flat surface. If the liquid–vapor interface is concave, the radius of curvature  $r$  of the liquid–vapor interface is negative and the vapor pressure over the droplet is reduced. Capillary condensation can also be considered as an effect of confinement on the vapor–liquid transition, where preferential wetting of the pore walls by the liquid over the vapor results in condensation at a different chemical potential to the bulk system. For an infinite slit of width  $H$ , the Kelvin equation can therefore be rewritten as

$$H = -\frac{2v_m [\gamma_{sv} - \gamma_{sl}]}{kT \ln [p/p_0]} \quad (2)$$

where  $\gamma_{sv}$  and  $\gamma_{sl}$  are the interfacial tensions of the solid–vapor and solid–liquid interfaces respectively. This expression can be more convenient to use than Equation (1) as no direct information is required about the liquid–vapor interface.

The effect of confinement on the solid–liquid transition can also be considered using similar arguments. If the liquid wets the pore walls better than the solid then the liquid will be thermodynamically favored in confinement. This results in a reduced melting point, as can be described in the following Gibbs–Thomson equation which is obtained by combining the Clausius–Clapeyron and Kelvin equations

$$\Delta T = \frac{\alpha T_m V_m \gamma_{sl}}{r \Delta H_f} \quad (3)$$

$\Delta H_f$  is the enthalpy of fusion (latent heat of melting),  $V_m$  is the molar volume of the solid,  $T_m$  is the bulk melting temperature of the solid,  $r$  is the radius of the pore, and  $\alpha$  is dependent on the geometry of the pore, equaling (3) for a sphere and (2) for a cylindrical pore. This expression can be used to describe melting in pores and the melting of small particles. The freezing transition, in contrast, will usually occur at a lower temperature than the melting transition, where there is a kinetic barrier associated with the formation of a critical nucleus of the solid phase. Indeed, impurity-free bulk liquids often exhibit significant supercooling.

A wide range of media have been used to investigate the freezing and melting of gases, organic liquids, water, and metals in nanoscale confinement including porous glasses,<sup>[47]</sup>

mesoporous solids, porous silicon, graphitic microfibers, and the surface forces apparatus. A depression of the melting and freezing temperatures is observed using techniques including calorimetry and NMR, while powder X-ray diffraction and neutron diffraction can be used to characterize the structures of the confined solids. Confinement can also influence the structure of the solid, where the effect is greatest in the smallest pores. The crystals formed often contain multiple stacking faults, as seen, for example, with krypton and xenon, which crystallized with their bulk FCC structure in 2.2–10 nm pores.<sup>[48]</sup> A study of the freezing of krypton and argon in 7 nm Vycor glasses revealed the formation of a disordered hexagonal close-packed (DHCP) structure and at very low temperatures the solid transformed to an FCC structure in coexistence with the DHCP structure.<sup>[49]</sup> An XRD study of the structure of nitrogen in the 5–75 nm pores suggested that the transition from an HCP to FCC structure, which occurs at 35 K in bulk, was absent in the porous structure,<sup>[50]</sup> and that the frozen nitrogen possessed a defect-rich HCP structure, with an amorphous component adjacent to the pore walls.

Small molecules such as cyclohexane often form crystalline phases that possess a high degree of molecular motion, where they are termed plastic crystals.<sup>[51]</sup> Confinement again affects the formation of these structures, where study of the freezing and melting of cyclohexane within 9 nm pores in porous glass revealed a depression of the melt–plastic crystal and plastic–brittle crystal transitions. A change in the molecular motion within these phases was noted in confinement as compared with bulk, as can be determined using NMR. In addition to depressing the melting point,<sup>[52]</sup> freezing of small molecules within small pores can also completely suppress crystallization such that a glass transition only is observed.<sup>[53]</sup>

Confinement can additionally lead to the formation of crystal structures not observed in bulk. Neutron diffraction studies of water freezing in porous glass and MCM-41 suggested that ice with a cubic structure—which is typically only seen under high pressure or in vapor deposition studies—can be generated in small pores.<sup>[54–58]</sup> Further, no crystalline ice was detected in very small (3 nm) pores.<sup>[57]</sup> Subsequent experimental and modelling studies have looked in greater detail at the structure of “cubic” ice and have shown that it is actually a “stacking-disordered” ice comprising cubic sequences interlaced with hexagonal sequences.<sup>[59–62]</sup>

With its low melting point, gallium is an attractive metal for studying the effects of confinement on freezing.<sup>[63]</sup> Synchrotron powder XRD of gallium freezing in porous glass revealed a complex phase behavior and the formation of two new structures, where the so-called  $\iota$ - and  $\kappa$ -Ga were observed in 7 and 3.5 nm pores, respectively. Estimation of the crystal size from the Scherrer equation showed that it exceeded the pore diameter, demonstrating that the crystals propagated through the network of pores. A significant depression of the melting and freezing points was also recorded.

The large surface/volume ratios of these systems, and a focus on the freezing/melting transitions also makes it possible to investigate the interface between the solid phase and the pore wall. XRD, neutron scattering and NMR studies of the phase transitions of water in a range of porous media including MCM-41 and mesoporous carbons have revealed the presence

of a few layers of water between the ice and pore walls.<sup>[56,58,64,65]</sup> Similar studies of the behavior of small organic molecules such as benzene and cyclohexane<sup>[66]</sup> and methane<sup>[67]</sup> have also revealed a liquid-like layer at the surface of the pore. The presence of a thin liquid film between a crystal and the pore wall is well-recognized in the field of geochemistry, and is a prerequisite to the development of crystallization pressure (see Section 11.2). It is hard to comment on the generality of this phenomenon, however, where the presence of such a thin interfacial film would be difficult to demonstrate conclusively in many systems, particularly those involving precipitation from solution. It does raise questions about heterogeneous nucleation however, where nucleation is invariably considered to occur on a substrate rather than on a bound solvent layer.

## 5. Crystallization in Droplets

Droplet-based systems are probably the most widely used environments for studying crystallization in confined volumes, and have found particular utility in investigating nucleation processes. There are multiple advantages to studying crystallization in these finite-sized systems as compared with bulk solution and very high supersaturations can be achieved. Crystallization within droplets enables the execution of large numbers of independent experiments, in identical environments and volumes. As nucleation is a stochastic process, where random fluctuations in a solution lead to the formation of a critical nucleus, this is essential to support a full statistical analysis.<sup>[68]</sup>

Droplets also avoid many of the problems encountered in bulk systems such as slow/inhomogeneous mixing, nonuniform temperatures, the influence of the reactor itself and the presence of impurities. When a solution is divided into small droplets, the impurities present are distributed over these volumes.<sup>[69]</sup> If the number of droplets is significantly larger than the number of impurities, then the majority will be impurity-free. With aqueous solutions prepared under typical laboratory conditions estimated as containing between  $10^6$  and  $10^8$  impurity particles per mL,<sup>[70]</sup> it is clear that droplets with diameters of  $\approx 50 \mu\text{m}$  or smaller are required if most are to be impurity-free.

### 5.1. Nucleation

The initial stage in the formation of a new crystal is termed nucleation, where this is a dynamic process involving the association (and dissociation) of atomic or molecular species into clusters.<sup>[71–74]</sup> The most widely used description of the nucleation of a crystal is that of classical nucleation theory (CNT), which considers the free energy change associated with the formation of a cluster. This was originally developed to describe the nucleation of a liquid from vapor,<sup>[75–78]</sup> such that many assumptions are made in order to translate it to crystalline systems.<sup>[79–81]</sup> These include assumptions that the nucleus grows one monomer at a time and that the nucleus essentially has the same properties as the bulk material, including the interfacial energy between the nucleus and solution. The use of continuum thermodynamics to model systems containing only a small number of units has also been questioned, and

alternative descriptions have been proposed to treat the thermodynamics of small systems.<sup>[82,83]</sup> However, due to its simplicity, and its reasonable qualitative agreement with experimental results, CNT remains a widely used framework for describing crystal nucleation, and forms the basis for most analyses of the effects of confinement on nucleation.

#### 5.1.1. Classical Nucleation Theory

The driving force required for nucleation is termed the supersaturation,  $S$ , where this is defined as the difference in chemical potential between a molecule in solution and one in the bulk of a crystal

$$\Delta\mu = kT \ln S \quad (4)$$

and

$$\Delta\mu = \mu_s - \mu_c \quad (5)$$

where  $\mu_s$  is the chemical potential of a molecule in solution and  $\mu_c$  is the chemical potential of the molecule in the bulk crystal. A supersaturation of  $S > 1$  is required for nucleation to occur, although in practice nucleation is not observed in many systems until far higher values are achieved. In an open system the supersaturation is the ratio between the activities of the free ions in solution versus the solubility product of the crystal, where it is noted the activities depend on the concentrations of all the main species in solution.

CNT considers the free energy change associated with the formation of a cluster to comprise two competing terms describing the free energy changes on forming the bulk and surface of the nucleus. While the former is favorable, molecules on the surface of the nucleus are only partially coordinated, making the formation of new surface energetically unfavorable. Given that these two terms have opposite signs, the change in free energy experiences a maximum as a function of the cluster size, and nucleation is associated with passage across a free energy barrier (**Figure 4a**). Considering the formation of a spherical cluster of radius  $r$  and containing  $n$  molecules, the change in free energy ( $\Delta G$ ) is described as

$$\Delta G = -n\Delta\mu + 4\pi r^2\gamma \quad (6)$$

where  $\gamma$  is the interfacial free energy. If the molecular volume in the bulk crystal is  $v_m$ , Equation (6) can be written as

$$\Delta G = -\frac{4}{3}\pi \frac{r^3}{v_m} \Delta\mu + 4\pi r^2\gamma \quad (7)$$

The first term is favorable and describes the free energy change associated with a molecule from solution becoming part of the bulk crystal, while the second term takes into account the interface between the cluster and the solution and is unfavorable. The nucleus size corresponding to the maximum in this function is termed the “critical nucleus” size,  $r_c$ , and is given as

$$r_c = \frac{2\gamma v_m}{\Delta\mu} = \frac{2\gamma v_m}{kT \ln S} \quad (8)$$

Beyond the critical nucleus, addition of a growth unit results in a reduction in the free energy such that it is energetically



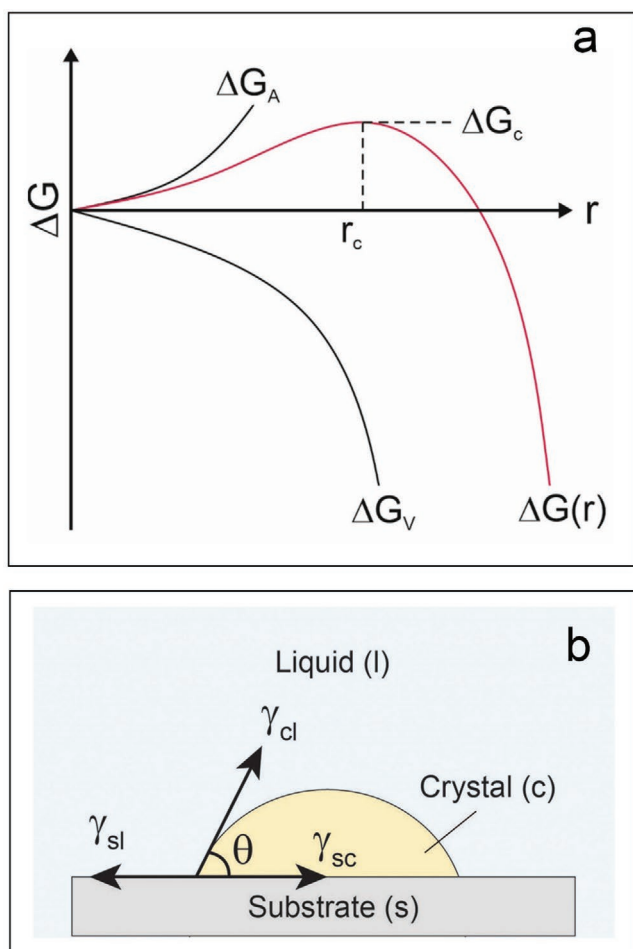


**Figure 4.** a) Schematic of the free energy ( $\Delta G$ ) of a growing crystal nucleus as a function of the radius ( $r$ ). The energy profile is a result of the favorable volume free energy ( $\Delta G_V$ ) and the surface free energy ( $\Delta G_A$ ). The maximum value ( $\Delta G_C$ ) is achieved at the critical radius ( $r_{crit}$ ). b) Illustration of the static equilibrium described by the Young equation. Three interfacial tensions,  $\gamma_{sl}$ ,  $\gamma_{cs}$ , and  $\gamma_{cl}$ , are balanced at a contact angle  $\theta$  between the nucleating phase and the substrate. In the example shown, favorable crystal/substrate interactions result in  $\theta < 90^\circ$  and a reduced barrier to nucleation.

favorable for the nucleus to grow in size. However, it is not until the nucleus reaches a size where  $\Delta G < 0$  does it become stable.

### 5.1.2. Nucleation Rate

While it is of course impossible to directly study the formation of a critical nucleus, information about nucleation can be obtained experimentally by measuring nucleation rates. According to classical nucleation theory, the volume-specific nucleation rate,  $J$ , of critical nuclei can be described in the form of an Arrhenius-type rate equation, where the nucleation rate is governed by the free energy barrier to nucleation

$$J = \frac{k}{V} = K \exp\left(-\frac{\Delta G_c}{k_B T}\right) \quad (9)$$

$\Delta G_c$  is the free energy change associated with the formation of a critical nucleus,  $V$  is the volume of solution,  $k_B$  is the Boltzmann constant, and  $T$  is temperature. This can also be written as

$$J = AS \exp\left(-\frac{B}{(\ln S)^2}\right) \quad (10)$$

The exponential term describes the barrier that the critical nucleus must overcome, where  $B$  is dominated by the interfacial energy between the crystal and the solution

$$B = \frac{16\pi\gamma^3 V_m^2}{3(k_B T)^3} \quad (11)$$

The pre-exponential term is a kinetic factor that relates to the transition from critical to supercritical nucleus growth and involves the diffusion of structural units to the surface of the nucleus.  $A$  is described as

$$AS = z f^* C_0 \quad (12)$$

where  $z$  is the Zeldovich factor related to Brownian motion,  $f^*$  is the attachment frequency, and  $C_0$  is the concentration of nucleation sites. For homogeneous nucleation,  $C_0 \approx V_m^{-1}$ .

It follows from this analysis that the nucleation rate depends strongly on the supersaturation and even more so on the interfacial energy. At high supersaturations, the critical nucleus is smaller and the nucleation rate higher. Similarly, for a given supersaturation, the smaller the interfacial energy, the smaller the critical nucleus and the higher the corresponding nucleation rate. A standard plot of the nucleation rate,  $J$ , against the supersaturation,  $S$ , shows that  $J$  is negligible until the supersaturation achieves a critical value termed  $S_{crit}$ . Once this value has been achieved the nucleation rate increases exponentially with further increase in supersaturation.

### 5.1.3. Heterogeneous Nucleation

Given the dominance of the interfacial energy in the expression for the nucleation rate, any process that reduces this quantity will increase the rate of nucleation. This is the driving force for heterogeneous nucleation—the formation of a nucleus on a foreign surface. Substrates on which the interfacial energy between a crystal and underlying substrate is lower than that between the crystal and solution can significantly enhance nucleation rates. The role of a substrate in reducing the energy barrier to nucleation can be described as

$$\Delta G'_c = \Phi \Delta G_c \quad (13)$$

where  $\Phi$  varies between 0 (no barrier to nucleation) and 1 (homogeneous nucleation).  $\Phi$  is defined by the interfacial energies of a crystal formed from solution on a solid substrate, where the Young equation describes the relationship between the contact angle of the crystal on the substrate, and the interfacial energies in the system

$$\gamma_{sl} = \gamma_{cs} + \gamma_{cl} \cos \theta \quad (14)$$

$\gamma_{sl}$ ,  $\gamma_{cl}$ , and  $\gamma_{sc}$  are the interfacial energies between the substrate (s) and liquid (l), the crystal (c) and liquid, and the substrate and crystal (Figure 4b). If the nucleus forms a solid cap on a substrate,  $\Phi$  is then defined as

$$\Phi = \frac{(2 + \cos\theta)(1 - \cos\theta)^2}{4} \leq 1 \quad (15)$$

It may therefore be expected that confined systems can exert a significant influence on crystallization processes, where the surface of the confining volume is of increasing importance as the volume decreases. It is noted, however, that the smooth, defect-free surfaces of many confining systems such as nanoporous media may not significantly stabilize a foreign nucleus.<sup>[43]</sup> The depression of freezing points observed in nanoporous media has therefore been associated with homogeneous nucleation within the center of the pores. As an alternative effect of confinement, impurities that can act as effective nucleating agents in bulk solution are frequently excluded from small volumes, which can lead to a significant reduction in nucleation rates.

#### 5.1.4. Effect of Finite Reservoirs on Crystal Nucleation

The exclusion of impurities from a crystallization environment has a significant effect on the induction times measured and it is in principle possible to study homogeneous nucleation within these environments.<sup>[84]</sup> The finite volume also has two additional effects on nucleation. The probability of nucleation necessarily depends on the total volume of the solution, where the probability that a droplet contains a crystal is given by

$$P(t) = 1 - \exp(-JV_d N_d t) \quad (16)$$

in which  $J$  is the nucleation rate,  $V_d$  is the volume of a droplet,  $N_d$  is the number of droplets, and  $t$  is the time.<sup>[85]</sup> The probability of observing nucleation within an array of droplets  $P(t)$ , is therefore significantly smaller than within a bulk experiment, where for example, 1000 spherical droplets of diameter 100  $\mu\text{m}$  have a total volume of just 0.5  $\mu\text{L}$ . The time taken to observe nucleation therefore scales with the volume, such that a  $10^3$ -fold reduction in the volume—equivalent to just a 10 fold reduction in the droplet radius—also reduces the mean nucleation time by a factor of  $10^3$ .

A second important effect arises from the consumption of ions during nucleation. This has a negligible effect on the supersaturation in bulk solution, such that nucleation effectively occurs at a constant supersaturation. The development of a nucleus within a small, finite volume, in contrast, leads to a continuous depletion of the reservoir of solute, and thus a parallel reduction in the driving force for formation of a critical nucleus. Theoretical consideration of nucleation within finite reservoirs reveals some interesting effects, where nucleation of both liquids and solids has been considered.<sup>[86–91]</sup>

Following the analysis presented by Grossier et al.,<sup>[92]</sup> classical nucleation theory describes the total decrease in the free energy of forming a nucleus of  $n$  solute molecules in an infinite reservoir (where the initial supersaturation,  $S_0$  remains constant during the formation of the nucleus) as

$$\Delta G_{\text{bulk}}(n) = -nk_B T \ln S_0 + An^{2/3} \quad (17)$$

where

$$A = 4\pi\gamma \left( \frac{3v_m}{4\pi} \right)^{2/3} \quad (18)$$

$\gamma$  is the interfacial energy and  $v_m$  is the molecular volume. This equation has to be modified for crystallization within a finite volume, where the depletion of solute gives rise to a continuous decrease in the supersaturation as

$$S(n) = \left( \frac{S_0 N_s - n}{N_s} \right) \quad (19)$$

where  $N_s$  is the number of solute molecules the droplet has at saturation (the equilibrium state). The change in the free energy of a forming nucleus with respect to a change in the number of constituent solute molecules can then be expressed as

$$dG_{\text{conf}}(n) = -k_B T \left( \frac{S_0 N_s - n}{N_s} \right) dn + \left( \frac{2}{3} An^{-1/3} \right) dn \quad (20)$$

leading to a total free energy change of

$$\Delta G_{\text{conf}}(n) = -k_B T \int_0^n \left( \frac{S_0 N_s - n}{N_s} \right) dn + An^{2/3} \quad (21)$$

This equation describes the change in free energy on forming a nucleus containing  $n$  solute molecules in a finite system as a function of the initial supersaturation  $S_0$ . Plotting this function for lysozyme crystallization from a  $0.78 \times 10^{-15}$  L droplet (diameter 10  $\mu\text{m}$ ) containing  $10^4$  molecules at different initial supersaturation levels illustrates the influence of confinement on nucleation (Figure 5). At low initial supersaturations, the depletion of supersaturation as the nucleus grows is too great and a growing nucleus can never achieve a size that is commensurate with the supersaturation. It is impossible for a critical nucleus to form under these conditions. It is not until the supersaturation exceeds a critical value ( $S_0 = 1.998$  for the considered lysozyme system) that a critical nucleus can form. Once this critical size has been achieved, the nucleus then continues to grow under conditions of depleting supersaturation until it reaches a second critical size associated with a potential well in the energy curve. Growth beyond this size again fails to yield a nucleus whose size is commensurate with the solution supersaturation. These thermodynamic effects can therefore limit the size that a nucleus can attain within a finite reservoir, or even prevent nucleation from solution supersaturations that would yield crystals in bulk solution.

#### 5.1.5. Alternative Nucleation Mechanisms

Advances in analytical techniques and computational resources have enabled significant advances in our understanding of crystal nucleation, such that it is now well-recognized that a range of mechanisms can operate depending on the system and reaction conditions. Two important categories are the two-step nucleation and prenucleation cluster pathways. Two-step nucleation refers to the observation that crystallization can occur in dilute systems (typically solution or vapor) via an initial fluid/fluid

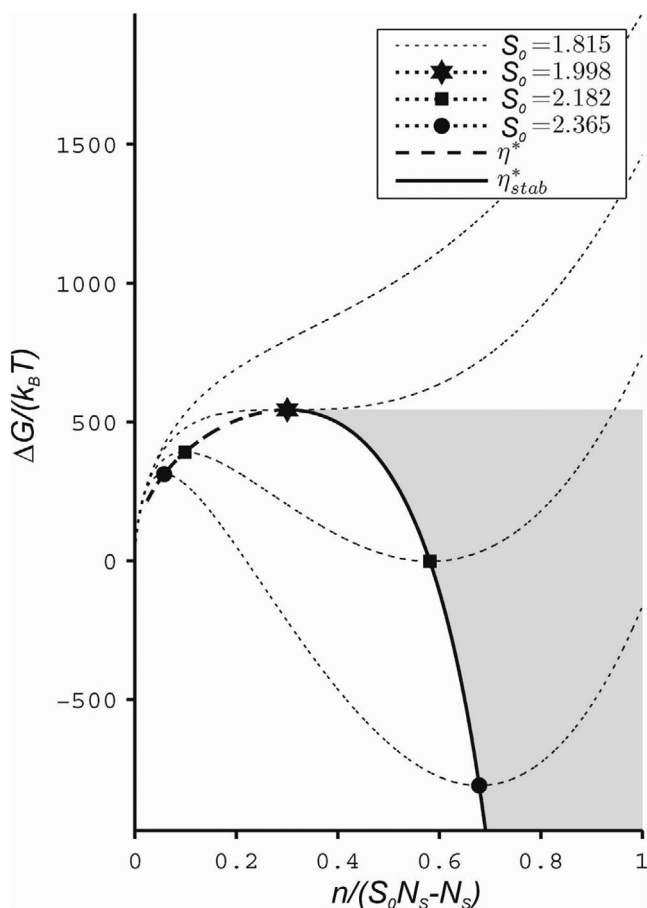


**Figure 5.** The evolution of free energy ( $\Delta G$ ) during the formation of an “ $n$ -sized cluster” for different initial supersaturations ( $S_0$ ). Reproduced with permission.<sup>[92]</sup> Copyright 2009, American Chemical Society.

transition.<sup>[79,80,93,94]</sup> In the case of a vapor this is the formation of a liquid phase, while from a dilute solution it is the formation of a concentrated solution phase. Crystallization then occurs within the intermediate liquid/concentrated phases, where these are metastable with respect to the crystalline phase.<sup>[80]</sup>

Considering crystallization from solution, the dense solution phase can be more stable or less stable than the initial dilute solution. In the former case, macroscopic quantities of the dense phase can form, and these can be long-lived. While this dense phase often accelerates nucleation, this does not occur if it is either too stable, or not stable enough, or if it is highly viscous such that diffusion/reorientation of the molecules is extremely slow. When the dense intermediate phase is less stable than the initial dilute solution, dynamic, and short-lived mesoscopic clusters form.<sup>[93,95]</sup> For these to support nucleation, they must be large enough to accommodate a nucleus, and have a sufficient lifetime to allow the nucleus to form. Nucleation is therefore expected to be very slow unless the barrier to nucleation is very low in these environments. Such two-step nucleation has been in a range of systems including proteins,<sup>[96–98]</sup> small organic molecules,<sup>[99,100]</sup> some inorganics,<sup>[101]</sup> and colloidal crystals.<sup>[102,103]</sup>

Prenucleation cluster pathways are often classified under “non-classical nucleation” mechanisms.<sup>[1,81,104]</sup> Following observations

of a population of clusters in solution prior to the nucleation of calcium carbonate,<sup>[105]</sup> it is now well-recognized that stable solute species form prior to nucleation in many systems including calcium carbonate,<sup>[104–107]</sup> calcium phosphate,<sup>[108,109]</sup> and iron oxides.<sup>[110]</sup> These have been termed prenucleation clusters and are thermodynamically stable solutes that are significantly larger than ion pairs, and which exhibit no phase boundary with surrounding solution. They are highly dynamic, and can possess structural motifs resembling those in the product crystal. As the supersaturation increases, the proportion of larger clusters increases, and these ultimately undergo a structural rearrangement, rendering them postnucleation species.

Characterization of nucleation mechanisms remains extremely difficult, even in bulk solution. This becomes even more challenging in confined systems, where many systems are poorly suited to in situ analysis. In common with classical nucleation mechanisms, however, a reduction in the volume of solution and thus the number of available precursor species would be expected to retard nucleation.

## 5.2. Experimental Investigations of Crystallization within Droplets

This section provides an overview of experimental studies of crystallization in droplet-based systems, where the emphasis is placed on the investigation of crystallization mechanisms rather than material synthesis. While early studies of the solidification of molten tin<sup>[69]</sup> and mercury<sup>[111]</sup> recognized the benefits of using droplets to study nucleation kinetics, dispersing the metal in a suitable fluid<sup>[111]</sup> or using commercial powders<sup>[69]</sup> gave large variations in the diameters of the droplets. Advent of techniques such as droplet levitation and microfluidics has overcome this problem and given convenient access to large populations of identical droplets. Further, each droplet can be characterized in situ, giving unique information about the crystallization process. This can be particularly valuable in studies of nucleation as the droplet defines a small volume in which nucleation will occur.<sup>[112]</sup> Droplet levitation and segmented-flow microfluidics create droplets suspended in a carrier fluid (liquid and gas respectively) and are considered first. More complex systems in which droplets are situated on solid substrates are then described.

### 5.2.1. Levitated Droplets

As the name suggests, the technique of “droplet levitation” creates suspended droplets whose only interfaces are with the surrounding air. Levitation can be achieved using electrostatic, electromagnetic, ultrasonic and aerodynamic techniques,<sup>[113–115]</sup> and droplets typically range from 50 pL to 5  $\mu$ L in size (equivalent to diameters of  $\approx$ 50  $\mu$ m to  $\approx$ 2 mm).<sup>[84,116,117]</sup> The droplets are maintained under conditions of controlled humidity and temperature, and crystallization can be induced through a change of temperature<sup>[118,119]</sup> (for example to investigate a freezing transition) or through evaporation.<sup>[116,117,120–122]</sup> A facile exchange of gases occurs between the droplet and its environment, and evaporation can be controlled leading to a concomitant increase in supersaturation and resultant crystallization.

These systems can be used to study nucleation, where techniques such as optical microscopy,<sup>[123]</sup> and angle-resolved light scattering<sup>[118–120]</sup> allow nucleation rates to be determined. The entire crystallization pathway occurring within individual droplets can also be characterized using in situ analytical techniques including IR,<sup>[124]</sup> UV–vis spectroscopy,<sup>[125]</sup> Raman spectroscopy and synchrotron X-ray diffraction<sup>[116,122,126]</sup> and images of the crystals forming within the droplets can be recorded using a high-speed camera.<sup>[121,124]</sup> This is particularly attractive for compounds that are polymorphic, or that form via metastable phases, and enables the entire process—from the evaporation of the solvent, to the formation of transient metastable and their ultimate transformation into stable crystalline forms—to be characterized.<sup>[116,122,124]</sup> Droplet levitation has also been used to study crystallization processes that are difficult to follow in bulk solution including the formation of clathrate hydrates,<sup>[121]</sup> and the amorphous to crystalline transition of ibuprofen.<sup>[124]</sup>

A nice example of the use of droplet levitation to study crystallization mechanisms is provided by an investigation into the precipitation of 5-methyl-2-[(2-nitrophenyl) amino]-3-thiophenecarbonitrile (also known as ROY) (Figure 6). ROY is often used as a model compound to investigate polymorphism in molecular systems,<sup>[126]</sup> where many of the polymorphs exhibit different characteristic colors. Use of in situ XRD and Raman spectroscopy to study the crystallization of ROY in a range of organic solvents in levitated droplets showed that crystallization occurred on evaporation of the droplets to yield yellow prisms (Y), red prisms (R), yellow needles (YN), or orange needles (ON). Pure polymorphs were generated in all cases, where their identity depended on the solvent employed and the concentration of ROY in the droplet. In most cases, complete evaporation of the droplet yielded an amorphous phase which subsequently transformed to a crystalline product. The one exception was Y, where this polymorph sometimes also formed directly as the droplet was evaporating. That different polymorphs formed on transformation of the amorphous phase in the presence of different solvents is intriguing. Extensive investigation of the amorphous phase using Raman spectroscopy found no evidence for residual solvent, suggesting that amorphous phases generated under different conditions could exhibit different short-range structures that could in turn provide a blue-print for different crystalline structures. A similar study of the precipitation of nifedipine also revealed a dependency of the crystallization pathway on the solvent, and showed that the  $\alpha$ -polymorph formed via different intermediates according to the solvent.<sup>[122]</sup>

Investigation of the crystallization of potassium dihydrogen phosphate (KDP) within levitated droplets using in situ Raman spectroscopy and X-ray scattering demonstrated that crystallization took place at exceptionally high supersaturations within these confined environments, and that the supersaturation level achieved at the onset of nucleation governed the crystallization pathway and polymorphs formed.<sup>[127]</sup> High supersaturations were obtained on evaporation of levitated droplets under conditions of controlled humidity, where the supersaturation at nucleation was estimated from the dimensions of the droplets recorded using video microscopy (Figure 7a). Notably, the interfacial energy estimated from the induction times was significantly higher than previously reported.

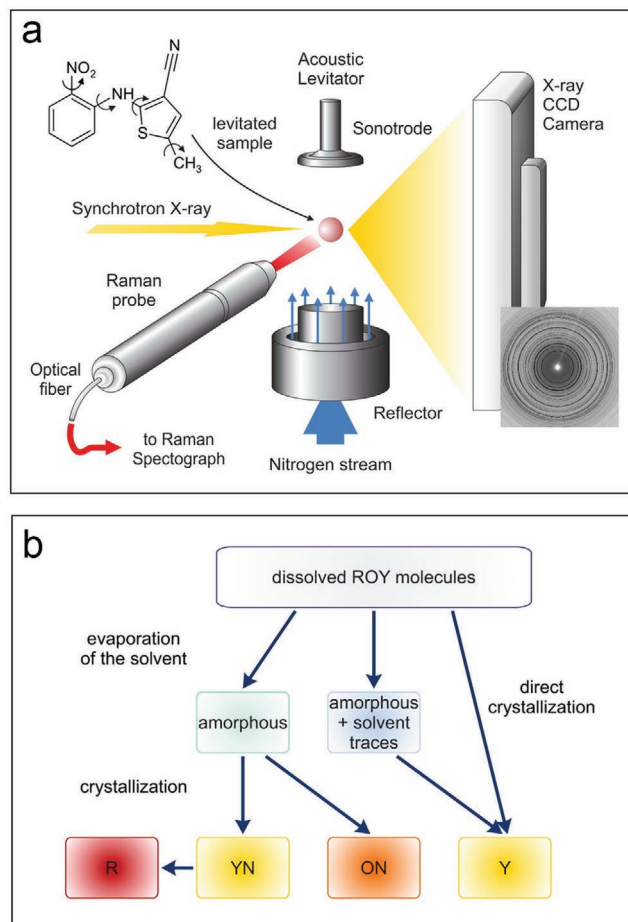


**Figure 6.** a) Schematic diagram of the setup and structure of ROY (5-methyl-2-[(2-nitrophenyl)amino]-3-thiophenecarbonitrile). The arrows indicate intramolecular degrees of freedom of the ROY molecule and display the rotational and torsional angles that differ in the molecular conformation of the molecule in the polymorphs. b) Summary of the crystallization pathways of ROY from different solutions. a,b) Reproduced with permission.<sup>[126]</sup> Copyright 2014, American Chemical Society.

Analysis of over 100 experiments revealed a bimodal distribution of crystallization probability with respect to supersaturation, and showed that KDP crystallization could proceed via two distinct pathways (Figure 7b). At supersaturations under  $S \approx 3.0$  crystallization proceeded slowly (taking  $>20$  s) and yielded a KDP crystal with the stable tetragonal structure. At  $S$  values of  $>3.2$ , in contrast, crystallization occurred within 1–3 s, and yielded a metastable KDP crystal with monoclinic structure. This polymorph had previously only been observed at high or low temperatures and ultimately transformed into the stable tetragonal structure. The solution also exhibited different local structures prior to crystallization in these supersaturation regimes, and a structural similarity was observed between the clusters present and the monoclinic form into which they transformed.

Studies with levitated droplets also give insight into the role of the droplet surface in the crystallization process. In situ investigation of the mechanism of calcium carbonate precipitation in droplets revealed that a liquid-like amorphous precursor

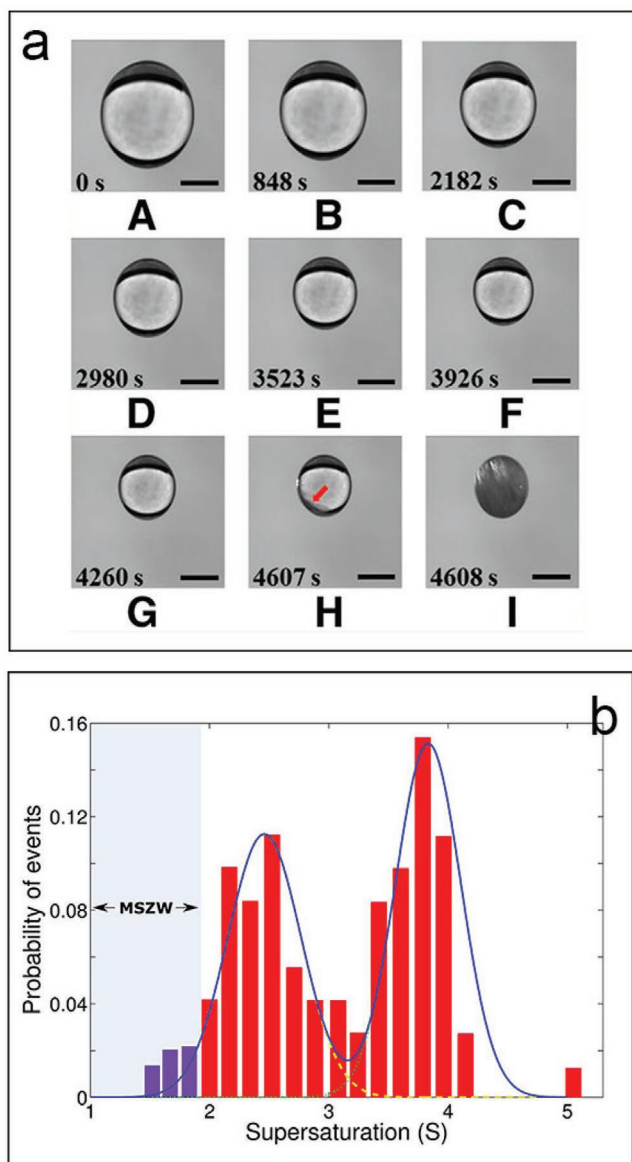


**Figure 7.** a) Sequence of optical microscopy images showing droplet shrinkage and the formation of KDP crystals as the droplet evaporates. During evaporation, the diameter of the droplet shrinks from 2.5 to 1.25 mm and the contactless environment enables unprecedentedly high degree of supersaturation ( $S \approx 4.1$ ), where very rapid crystallization can be observed within 1 s (scale bar: 1 mm.) b) The probability of crystallization events in drops as a function of supersaturation. The first and second peaks at around  $S = 2.45$  and  $S = 3.83$  form more Gaussian-like distributions. A blue line is a cumulative curve with two Gaussian fitting curves. The metastable zone width (MZSW) is shown below  $S = 2.0$ . a, b) Adapted with permission.<sup>[127]</sup> Copyright 2016, National Academy of Sciences, USA.

phase initially forms homogeneously throughout the droplet and that it then transforms to calcite via a dissolution/reprecipitation mechanism.<sup>[116]</sup> Ex situ transmission electron microscopy (TEM) suggested that precipitation of the amorphous phase is not initiated at the air/water interface. Weidinger et al studied the nucleation of *n*-alkanes with chain lengths of 14–17 by cooling droplets of the liquid alkanes.<sup>[118]</sup> Measurement

of nucleation rates and induction times demonstrated supercooling and suggested that nucleation occurs at the ordered solid layer that forms at the surface of the droplets. Turnbull investigated the solidification of 2–8  $\mu\text{m}$  droplets of mercury coated with species including mercury acetate, stearate, laurate, and iodide using dilatometry.<sup>[111]</sup> While droplets coated with mercury laurate solidified at rates consistent with homogeneous nucleation, nucleation in most other systems was heterogeneous, influenced either by the droplet surface or particulate impurities suspended in the droplets.

Electrodynamic levitation of droplets also provides a unique opportunity to investigate the influence of the excess surface charge (ESC) of the droplets on crystallization. Investigation of NaCl crystallization showed that an increase in the ESC resulted in an increase in the number of NaCl crystals formed, where this was partially attributed to the increase in the rate of evaporation of droplets with higher charge.<sup>[117]</sup> This was accompanied by a change from a cubic to a dendritic crystal morphology when the ESC exceeded a critical value. Similar results were obtained for two organic compounds, trihydroxyacetophenone monohydrate (THAP), and *R*-cyano-4-hydroxycinnamic acid (CHCA).<sup>[117]</sup> Hermann et al. also investigated NaCl precipitation and observed that nucleation occurred at higher relative humidities in droplets with higher negative charges.<sup>[128]</sup> Molecular dynamics simulations suggested that the negative charge carrier is  $\text{OH}^-$  and that this promotes the formation of clusters adjacent to the surface of the droplet.

A number of studies have also used levitated droplets to obtain nucleation kinetics of compounds ranging from alkanes<sup>[118]</sup> and ice,<sup>[119]</sup> to soluble inorganics,<sup>[84,120]</sup> and proteins,<sup>[123]</sup> where data is obtained from hundreds of experiments with identical droplets. These are conducted under isothermal conditions, and with controlled humidity such that a constant supersaturation is maintained during the measurement. Under these conditions, the nucleation rate ( $k$ , units  $\text{s}^{-1}$ ) can be determined by recording the number of droplets that have crystallized after a given time. The probability that crystallization has *not* occurred within a droplet ( $P$ ) after a given time ( $t$ ), is then given by

$$P(t) = \frac{N(t)}{N} \quad (22)$$

where  $N(t)$  is the number of droplets that do not contain crystals after time ( $t$ ) and  $N$  is the total number of droplets. In the simplest scenario when nucleation occurs at a constant rate (i.e., there is a unique nucleation frequency), the nucleation rate is readily derived from  $P(t)$  as

$$P(t) = -\exp(kt) \quad (23)$$

where a plot of  $P$  versus  $\ln(t)$  therefore gives a straight line. Deviation of the data from a straight line demonstrates more complex behavior. This usually derives from the presence of active impurities, or the droplet surface, which can introduce multiple nucleation pathways. Readers are directed to a super review by Sear that describes the range of models used to analyze such nucleation data.<sup>[129]</sup>

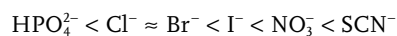
Measurement of nucleation rates at different supersaturations and application of classical nucleation theory then enables parameters such as the interfacial energy between the crystal

and the solution to be determined (see Section 5.1). Analysis of water freezing yielded a straight-line relationship between  $\ln P$  and  $t$ , which is consistent with homogeneous nucleation.<sup>[119]</sup> The nucleation of potassium nitrate, in contrast, showed non-linearity and the curve was fitted with a two-exponential function that yielded two volume-dependent rates that varied by one to two orders of magnitude.<sup>[120]</sup> The faster rate undoubtedly corresponds to heterogeneous nucleation on impurities in the droplets. Extraction of the pre-exponential factor for the slower rate yielded a lower value than that expected for homogeneous nucleation, suggesting that it also corresponded to heterogeneous nucleation, possibly governed by the droplet interface rather than impurities. Investigation of the nucleation of alkane crystals,<sup>[118]</sup> and proteins,<sup>[123]</sup> also showed nonlinearity in the simple exponential plot, where the study of alkane freezing also implicated the solution/air interface in the nucleation process.

### 5.2.2. Pendant Droplets

A simple approach to studying crystallization within individual droplets is offered by a strategy in which a single droplet is created on the tip of a nanopipette within oil.<sup>[130,131]</sup> The nanopipette can be created using standard procedures and hydrophobized using silanes to prevent wetting of the glass surface by the aqueous solution (Figure 8).  $K_2SO_4$  was precipitated in the presence of  $K_2HPO_4$ , KCl, KBr, KI,  $KNO_3$  within droplets bounded by surfactants and immersed in 1-decanol. Stearic acid and undecanol had no templating effect on  $K_2SO_4$  nucleation while 1-octadecylamine (ODA) induced nucleation at a lower supersaturation, an effect that was attributed to the concentration of ions at the ODA/solution interface. ODA was also

the only surfactant to support the formation of a single crystal product, as reflects the lower onset supersaturation. The influence of the ODA monolayer was altered by the addition of ions, where the magnitude of the effect followed the Hoffmeister series



such that the onset supersaturation and crystal morphologies obtained in the presence of  $NO_3^-$  and  $SCN^-$  were comparable to those formed in the absence of the monolayer. These chaotropic ions are therefore expected to disturb the templating ability of the ODA monolayer. The same system was also used to study the precipitation of potassium hexacyanoferrate(II) trihydrate (KFCT) in surfactant-stabilized droplets,<sup>[130]</sup> where this material exhibits a range of polymorphs and crystal habits. Here, the choice of surfactant had little influence on the supersaturation at the onset of crystallization, but different proportion of hexagonal and octagonal crystals—which were suggested to correspond to different polymorphs—were observed.

### 5.2.3. Droplets Using Microinjection

Microinjection provides a convenient route for accessing droplets suspended in an oil phase. A microinjector can be used to create an array of surfactant-free aqueous droplets immersed in an oil and supported on a hydrophobic substrate.<sup>[86]</sup> Variation of the speed of movement of the translation stage on which the substrate is mounted gives control over the droplet size, where this falls within the picoliter to femtoliter regime. This technique was used to form droplets of NaCl solution, and nucleation occurred as water evaporated from the droplets into

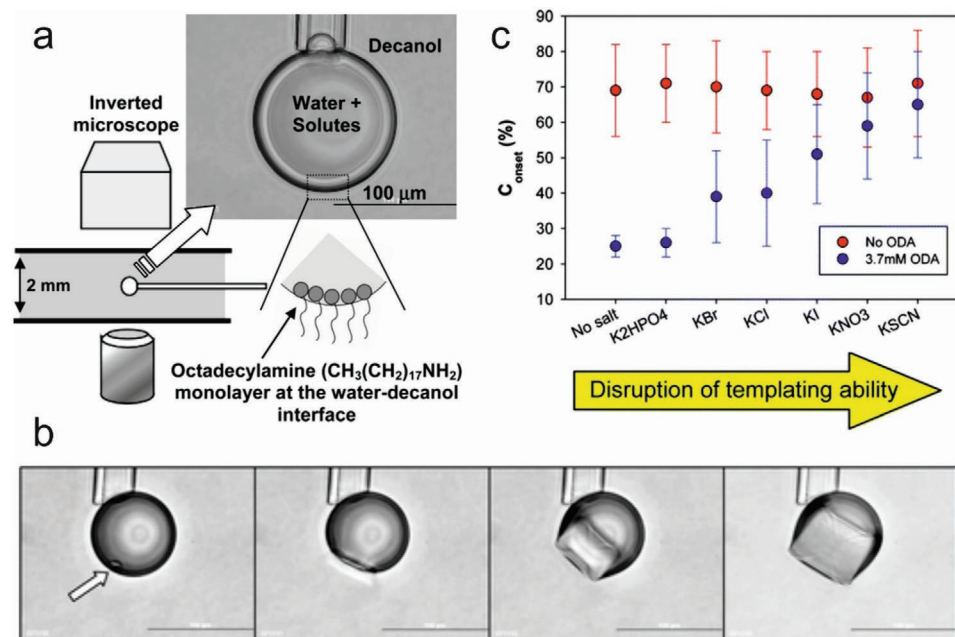


**Figure 8.** a) Schematic representation of an isolated aqueous microdroplet based crystallization. b) Videomicrographs of crystallization process in a microdroplet containing  $K_2SO_4$  surrounded by decanol containing 1-octadecylamine (ODA). c) Anion effects on the crystallization onset ( $C_{onset}$ ) of  $K_2SO_4$  crystallization in the presence of ODA and absence of ODA in decanol. a–c) Reproduced with permission.<sup>[131]</sup> Copyright 2010, American Chemical Society.

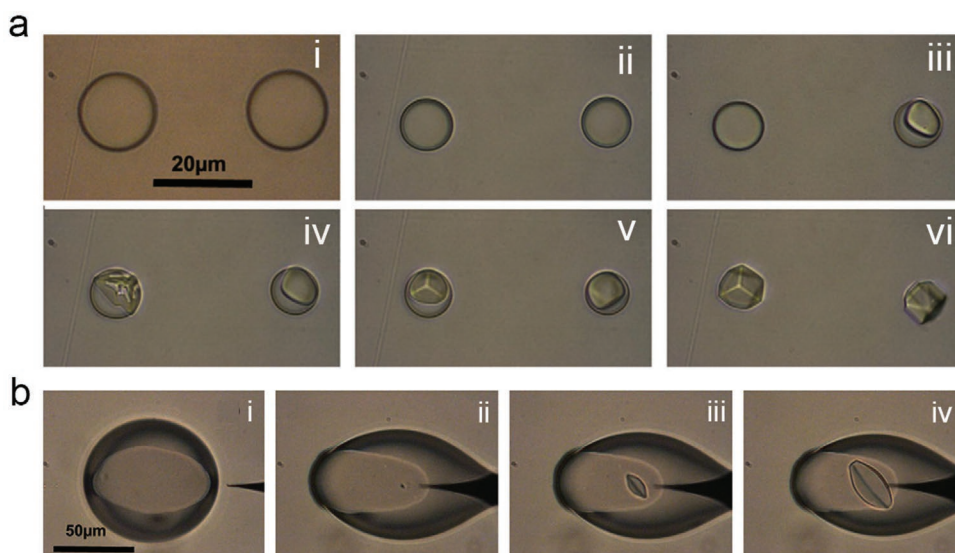


**Figure 9.** a) Nucleation and growth of  $\text{KNO}_3$  in  $\text{H}_2\text{O}$  in FC-70 oil: i) droplet size  $15\ \mu\text{m}$  ( $2\ \text{pL}$ ) at  $t = 0$ , ii) droplet size  $9.3\ \mu\text{m}$  ( $0.48\ \text{pL}$ ),  $t = 8\ \text{min}\ 29\ \text{s}$ , iii)  $t = 9\ \text{min}\ 15\ \text{s}$ , iv)  $t = 9\ \text{min}\ 17\ \text{s}$ , v)  $t = 10\ \text{min}\ 18\ \text{s}$ , and vi)  $t = 12\ \text{min}\ 12\ \text{s}$ . b) Initiation of nucleation of a crystal of bovine pancreatic trypsin inhibitor (BPTI) by insertion of a sharp probe at: i)  $t = 0$ , ii)  $t = 30\ \text{min}$ , iii)  $t = 80\ \text{min}$ , and iv)  $t = 130\ \text{min}$ . a,b) Reproduced with permission.<sup>[133]</sup> Copyright 2013, Elsevier Masson SAS.

the surrounding oil, resulting in high supersaturations.<sup>[132]</sup> The NaCl concentration, and thus supersaturation of the droplets at any point in time was estimated by monitoring the change in optical contrast between the droplets and surrounding oil.

Nucleation within  $10\ \text{pL}$  droplets occurred at supersaturations of  $\approx 1.3$ , as compared with  $1.03$  in bulk solution, where this was attributed to a kinetic effect. Once the crystals nucleated, they grew very rapidly at an estimated rate of  $10\ \mu\text{m}\ \text{s}^{-1}$ , which is orders of magnitude faster than in bulk solution. Nucleation of NaCl was proposed to occur via a two-step mechanism, where the confined system achieves a metastable, highly supersaturated state. This supports the formation of a dense liquid phase in which nucleation can occur very rapidly. Comparable experiments were conducted for the crystallization of  $\text{KNO}_3$ , where nucleation occurred during the evaporation of droplets of supersaturated solutions at room temperature (Figure 9a).<sup>[133]</sup> Interesting, although the authors do not comment on it, it is clear from the morphologies of the crystals that they are the calcite rather than the aragonite polymorph, where the latter is stable under ambient conditions.

A microinjector approach was also used to precipitate calcium carbonate by injection of equimolar droplets of  $\text{Na}_2\text{CO}_3$  solution into  $\text{CaCl}_2$  droplets at different volume ratios.<sup>[134]</sup> A viscous sol initially formed under all solution conditions and remained stable until the droplet evaporated in  $\approx 2/3$  of the droplets. The remainder transformed to calcite, or vaterite in a few cases within minutes to hours. Transformation was rapid following the appearance of crystals of the more stable phase, and the stability of the precursor phase was greatest in droplets with a  $\text{Ca}^{2+}/\text{CO}_3^{2-}$  ratio of 1. Calcite seed crystals were also injected into droplets containing the precursor phase, where these again triggered a rapid transformation. The precursor phase was identified as ikaite ( $\text{CaCO}_3 \cdot 6\text{H}_2\text{O}$ ), a surprising result given that the solution was supersaturated with respect to ACC.

By carrying out nucleation experiments within droplets, the position where nucleation occurs is also localized, offering the possibility of studying an individual nucleation event. Experiments to induce nucleation were performed by inserting a sharp tip into droplets containing metastable KCl or NaCl solutions.<sup>[86,112]</sup> High speed imaging of the induction of NaCl nucleation within  $60\ \mu\text{m}$  droplets showed that nucleation occurred within  $5\ \text{ms}$  of insertion of the tip, and the subsequent growth rate was  $>200\ \mu\text{m}\ \text{s}^{-1}$ . A transition in the morphology of the crystal from rough to faceted occurred in under  $1\ \text{s}$ . An identical effect was demonstrated for the small protein bovine pancreatic trypsin inhibitor (BPTI) (Figure 9b).<sup>[133]</sup> Crystals adhered to the tip can be removed from the droplets for further analysis as required.

#### 5.2.4. Segmented-Flow Microfluidic Systems

Providing a straightforward means of rapidly creating very large numbers of identical droplets, segmented-flow microfluidic devices have found increasing application in crystallization studies.<sup>[135,136]</sup> They can also be prepared such that they are optically-transparent and can be coupled to a range of analytical techniques, allowing crystallization processes to be monitored in situ. Crystallization can be induced by a range of methods. Highly soluble compounds are readily precipitated by forming droplets of the desired compound and then changing the temperature or allowing evaporation to increase supersaturation. Poorly soluble compounds have been generated by a range of methods including combining reactant solutions at the point of droplet formation,<sup>[137]</sup> creating streams of droplets that alternate in content and subsequently merging pairs of droplets,<sup>[138]</sup> or directly injecting one solution into flowing droplets.<sup>[139]</sup>

Initial studies of crystallization in droplet microfluidic devices focused on the development of strategies to generate

large, high quality protein single crystals for structural analysis.<sup>[140]</sup> Ideal solution conditions were determined by preparing large numbers of droplets containing different concentrations of the protein and precipitant,<sup>[140]</sup> where this was achieved by varying the flow rates of the input fluids at the point of droplet formation, such that different volumes of these solutions were combined. The droplets are then stored and the protein crystals can be screened in situ using techniques including synchrotron X-ray diffraction.<sup>[141]</sup> More elaborate chips that are designed to give separate control over crystal nucleation and growth can be used to generate high quality protein crystals.<sup>[142]</sup> Seed crystals were formed in plugs in the “nucleation zone” by combining high concentrations of protein and precipitant, and further solutions of proteins and precipitant were then added in a second zone on the chip such that growth of the seeds occurred at low supersaturation. Microfluidic crystallizers have also been developed to produce protein crystals with uniform size distributions, where control over the number and size of the crystals in each droplet was achieved by varying solution concentrations and the incubation temperature.<sup>[143,144]</sup>

These well-defined environments provide an excellent means of investigating crystal polymorphism and solubility. In common with other confined systems, metastable polymorphs can be generated within these environments and show exceptional lifetimes. Droplets of potassium nitrate solution were formed and stored on-chip, and droplets were quenched to  $\approx 10$  °C below their solubility (Figure 10). The temperature was then gradually reduced to induce crystallization.<sup>[68,145]</sup> A single crystal formed in most droplets and two polymorphs were observed, where the solubility of each polymorph could

be determined by stepwise increase of the temperature. Comparable results have been obtained in a range of other systems including the precipitation of glutamic acid, phenylalanine, indomethacin, and paclitaxel in aqueous microdroplets.<sup>[146]</sup> The reaction conditions could be controlled such that a single crystal formed in the majority of droplets and metastable polymorphs that were stable for long periods (over 3 months in some cases) were observed. A metastable polymorph of lysozyme with extended lifetime has also been observed in droplets.<sup>[147]</sup>

That just one crystal forms can be attributed to the depletion of reagents within the drops as the first crystal grows, such that the supersaturation drops to a level that does not support a second nucleation event.<sup>[148]</sup> The observation of metastable polymorphs in these droplets, in turn, can be attributed to the high supersaturations that can be achieved in these environments, which can favor metastable polymorphs.<sup>[149,150]</sup> The reduction/elimination of convection in the droplets also reduces the rate of nucleation and growth, which retards the transformation of the metastable polymorph.

A number of studies have employed segmented-flow microfluidic systems to investigate calcium carbonate precipitation, where this system exhibits multiple polymorphs and hydrates. Reproducible control over calcium carbonate crystal polymorph was achieved in a system in which droplets were created when two streams of  $\text{CaCl}_2$  and  $\text{Na}_2\text{CO}_3$  reagents were broken by an oil flow in a flow-focusing device. According to the reagent concentrations ( $12 \times 10^{-3}$  M and below) and droplet volume, pure calcite, pure vaterite, or a mixture of calcite and vaterite crystals could be precipitated.<sup>[151]</sup> Use of a comparable device and

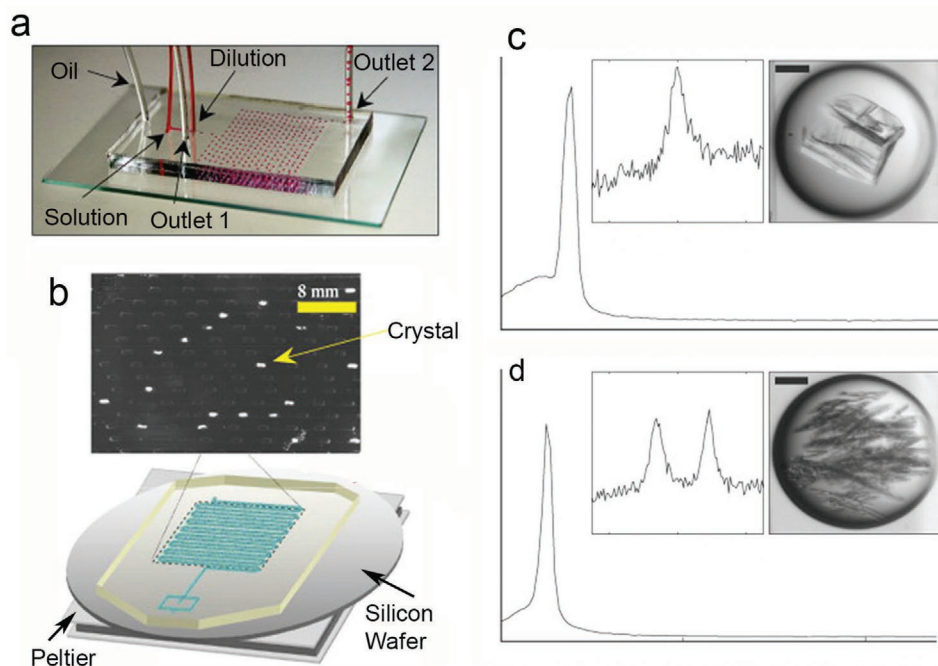


**Figure 10.** a) Photograph of the microfluidic chip, where monodisperse droplets, here colored with a dye, form at the intersection of the aqueous and oil streams. The droplets flow in the long microchannel. b) Schematic of the experimental setup where the PDMS device is sealed on a silicon wafer and placed on a Peltier module to control its temperature, and accompanying image obtained under crossed polarizers of the storage area where birefringent crystals appear as bright spots. c,d) Raman spectra measured on the two different crystals, and optical microscopy images of the corresponding crystals. Scale bars = 100  $\mu\text{m}$ . a–d) Reproduced with permission.<sup>[145]</sup> Copyright 2008, Elsevier.



$50 \times 10^{-3}$  M concentrations yielded surprising results where ikaite ( $\text{CaCO}_3 \cdot 6\text{H}_2\text{O}$ ) was the first phase formed, occasionally together with small quantities of monohydrate ( $\text{CaCO}_3 \cdot \text{H}_2\text{O}$ ).<sup>[134]</sup> This subsequently transformed to calcite and some vaterite. Surprisingly, no ACC was observed in this system, despite the solubility product having been exceeded. This also contrasts with other studies of calcium carbonate precipitation in microfluidic droplets where ACC was clearly demonstrated as the initial precipitated phase.<sup>[137,139]</sup> Notably, these employed lower reagent concentrations, and also more sophisticated strategies for reagent mixing that precluded precipitation at the point of droplet mixing.

Segmented-flow microfluidic systems have also been used to investigate the importance of solution mixing in nucleation processes, where mixing within droplets has been studied using high speed video microscopy. Each droplet provides a well-defined environment, and mixing is well-understood and can be controlled by varying flow rates and introducing serpentine channels. Addressing the crystallization of the protein Thaumatin, droplets of the protein solution were prepared in the carrier oil using a T-junction configuration, and precipitation was induced by combining flows of protein and precipitant ( $\text{KNaC}_4\text{H}_4\text{O}_6$ ) solutions, separated by a flow of buffer solution (Figure 11a).<sup>[152]</sup> Passage of the droplets through a serpentine channel promoted mixing. Nucleation of Thaumatin was strongly dependent on the flow rate/mixing, such that immediate precipitation was observed at slow flow rates which yielded precipitation or multiple small particles after 8 h. No immediate precipitation occurred at fast flow rates, and only a few large crystals formed after 8 h (Figure 11a).

These results were readily rationalized by considering the mixing of the precipitant and protein solutions within the

droplets (Figure 11b). This principally occurs by chaotic advection, which generates interfaces between these solutions across which diffusion can occur. The nucleation rate therefore depends on the area and lifetimes of these interfaces, and the concentrations of the protein and precipitant in the adjacent solutions. These are in turn governed by the flow rate, where the interfaces stretch and fold as the droplet travels along the serpentine channel, increasing their total area and accelerating mixing. The total area of the interfaces is therefore greater at higher flow rates before complete mixing occurs, but their lifetimes are lower. Estimating the mixing effect as the product of the lifetime and total area of the interfaces, and assuming that nucleation occurs within a zone at the interface between the protein and precipitant solutions, the number of nucleation events can be approximated as

$$N \sim w^{7/2} (DU^{-1/2}) \quad (24)$$

where  $N$  is the number of nucleation events,  $w$  is the diameter of the channel,  $D$  is the diffusion coefficient, and  $U$  is the flow rate. The process by which mixing occurs, rather than just the mixing time, is therefore critical in determining the outcome of crystallization, where rapid chaotic mixing could be used to eliminate rapid nucleation at high supersaturations, and slow chaotic mixing to promote nucleation at lower supersaturation.

The role of mixing in determining the outcome of crystallization reactions has also been seen in the precipitation of calcium carbonate.<sup>[139]</sup> A picoinjector was used to prepare droplets of  $2.5 \times 10^{-3}$  M calcium carbonate solution in oil by injecting  $\text{Na}_2\text{CO}_3$  or  $\text{CaCl}_2$  solution into flowing droplets of the counterion. The droplets were then passed along a straight or serpentine channel prior to collection of the product crystals by

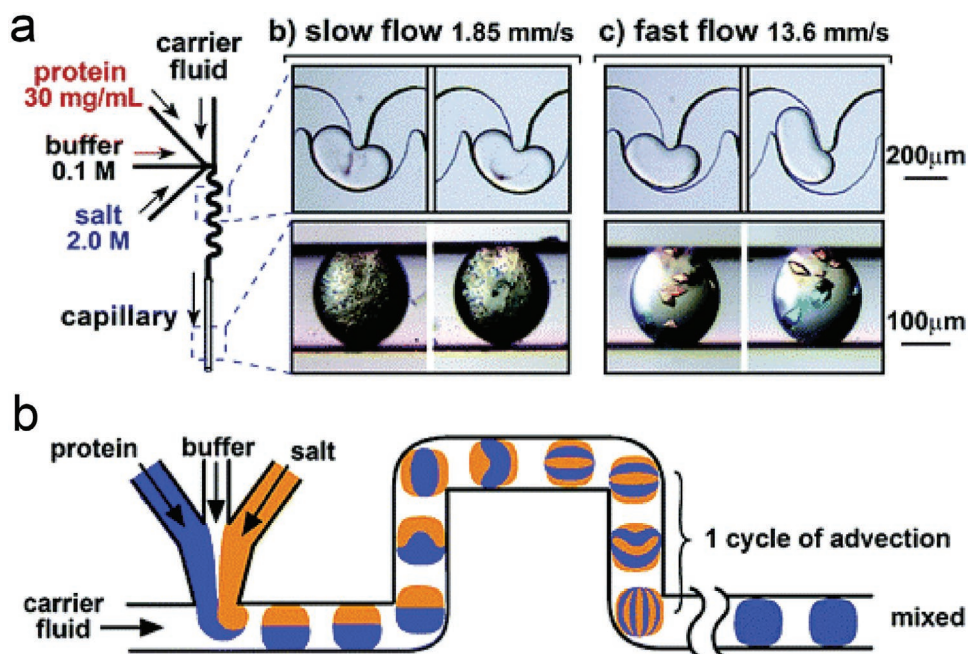


**Figure 11.** a) A schematic of the microfluidic channel. Low-flow velocity produced microcrystals, whereas, at high flow velocity large crystals grew. b) A schematic of the stretching and folding of interfaces as plugs are being mixed by chaotic advection in a winding channel. a,b) Reproduced with permission.<sup>[152]</sup> Copyright 2005, American Chemical Society.

filtration after 5 min. The straight channel device principally generated vaterite crystals, while calcite crystals, together with a few vaterite particles, formed in the serpentine device. Control experiments performed in bulk solution yielded results comparable to those produced in the serpentine device. This again demonstrates that processes occurring in the first few milliseconds of crystallization—long before crystals are observed—define the product of the reaction.

Droplet microfluidics are additionally finding increasing application for studying nucleation kinetics, where in contrast to droplet levitation, many hundreds of experiments can be performed simultaneously.<sup>[153]</sup> The droplet volume can also be precisely controlled, which is essential to the analysis of nucleation kinetics.<sup>[154]</sup> Measurement of the evolution of the fraction of droplets that contain crystals over time under constant supersaturation therefore yields the nucleation kinetics,<sup>[68]</sup> as discussed in Section 5.2.1. Analysis of nucleation kinetics has been carried out for a wide range of systems including proteins,<sup>[155,156]</sup> soluble organics<sup>[156,157]</sup> and inorganics,<sup>[68,70,85,158]</sup> poorly-soluble compounds,<sup>[159,160]</sup> and the solidification of melts,<sup>[161,162]</sup> and most systems exhibit complex nucleation kinetics due to multiple pathways.

One of the earliest studies to use microfluidic devices to study nucleation in droplets focused on potassium nitrate.<sup>[68,85]</sup> The temperature of the droplets was rapidly reduced, and the fraction of the droplet population containing crystals was then measured as a function of time at a specific temperature—and therefore supersaturation. A nonconstant nucleation rate was observed, and the data were analyzed according to the method of Pound and La Mer<sup>[163]</sup> to extract individual rates that could potentially correspond to homogeneous and heterogeneous nucleation. Assuming that impurities are randomly distributed among the droplets and that the average number of active sites in a droplet is  $m$ , the probability that a droplet does not contain a crystal,  $P(t)$  can be described as

$$P(t) = e^{-m} (e^{-k_0 t} - 1) + e^{-m} \exp(m e^{-k_i t}) \quad (25)$$

where  $k_0$  is the homogeneous nucleation rate observed in impurity-free droplets, and  $k_i$  is the heterogeneous nucleation rate for a droplet containing just one type of impurity. Extraction of pre-exponential factors confirmed that nucleation within the droplets was heterogeneous, while the fact that  $m$  increases with increasing supersaturation shows that multiple nucleation sites operate, and that they can become active at different supersaturation values. Comparable results have been obtained for the crystallization of a range of other compounds from solvents, illustrating the role of impurities and potentially the droplet interface even in these very small volumes.

With the possibility of performing multiple dissolution/precipitation cycles within individual droplets, microfluidic devices give a unique opportunity to further investigate whether the distribution in induction times is due to the stochastic nature of nucleation or the presence of specific impurities within certain droplets.<sup>[68]</sup> By carrying out multiple cycles, certain droplets were observed to exhibit higher activity for potassium nitrate nucleation. This effect was quantified by comparing the probability of crystals forming within individual droplets with the distribution predicted for random behavior

$$p_g = C_n^{n_c} p^{n_c} (1 - p)^{n-n_c} \quad (26)$$

where  $p_g$  is the probability that  $n_c$  nucleation events occur in an individual droplet over  $n$  crystallization cycles. The experimental data was a poor match for random behavior, which demonstrates the role played by impurities in promoting nucleation in the most active droplets.

Investigation of the solidification of hexadecane ( $C_{16}H_{34}$ ) and ethylene glycol distearate (EGDS) revealed complex kinetics consistent with at least two nucleation pathways.<sup>[161]</sup> Analysis of freezing/melting cycles showed that more than one population of droplets were present, where those that freeze at higher temperatures undoubtedly contain impurities that act as heterogeneous sites. These impurities also become more active as the temperature decreases, and even the slow nucleation rate is likely to derive from nucleation at the droplet surface. In a technically impressive paper, Stan et al. used a microfluidic device to investigate the nucleation kinetics of ice formation from 80  $\mu$ L droplets of water.<sup>[162]</sup> Temperatures were measured to an accuracy of 0.4 °C, and the freezing point was recorded with a high-speed camera. Analysis of the freezing of >37 000 droplets revealed possible homogeneous nucleation at temperatures between –36 and –378 °C. By comparison, nucleation in the presence of AgI, an effective nucleant for ice, occurred at –10 to –19 °C.

A microfluidic device was also used to explore the nucleation rate of calcite from ACC.<sup>[160]</sup> 100  $\mu$ m droplets of 1 M  $CaCl_2$  solution stabilized with a nonionic surfactant were generated using a flow-focusing device and were stored in individual wells to give long-term stability. Precipitation of calcium carbonate was then initiated by flowing ammonium carbonate vapor through the device, where ACC formed in every droplet within 30 min. The transformation of ACC to calcite was monitored using polarization optical microscopy over the following 5 days, yielding a nucleation rate of 1.2  $cm^{-3} s^{-1}$ . Once a calcite particle was detected, it grew within 1 h to consume all of the ACC.

Studies of nucleation in levitated droplets suggest that the droplet surface can play a role in nucleation.<sup>[120]</sup> This can also be studied in droplet microfluidic devices by varying the continuous phase. Investigation of the nucleation rate of lysozyme using silicone oil and a fluorinated oil demonstrated that the oil/water interface plays a role in nucleation, and that silicone oil was more effective in promoting nucleation.<sup>[164]</sup> A detailed study of the nucleation of potassium nitrate in droplets suspended in silicone oil, fluorinated oil, paraffin, and tocopherol carrier fluids supported this finding (Figure 12a).<sup>[70]</sup> All systems exhibited two populations of droplets: those that crystallized rapidly, and those that crystallized slowly (Figure 12b). The faster rate can be attributed to heterogeneous nucleation associated with impurities, where these may have originated from the reactant solution and/or carrier fluid. That the nucleation rate increases immediately after supersaturation was achieved for all systems also demonstrates that different sites become active at higher supersaturations. As this rate was sensitive to the oil employed, the active impurities are likely to be associated with the interface.

Estimation of the pre-exponential factors ( $A$ ) of the nucleation rate equation showed that the second, slower rate was also likely to correspond to heterogeneous nucleation. This was further supported by the fact that the onset of nucleation was sensitive

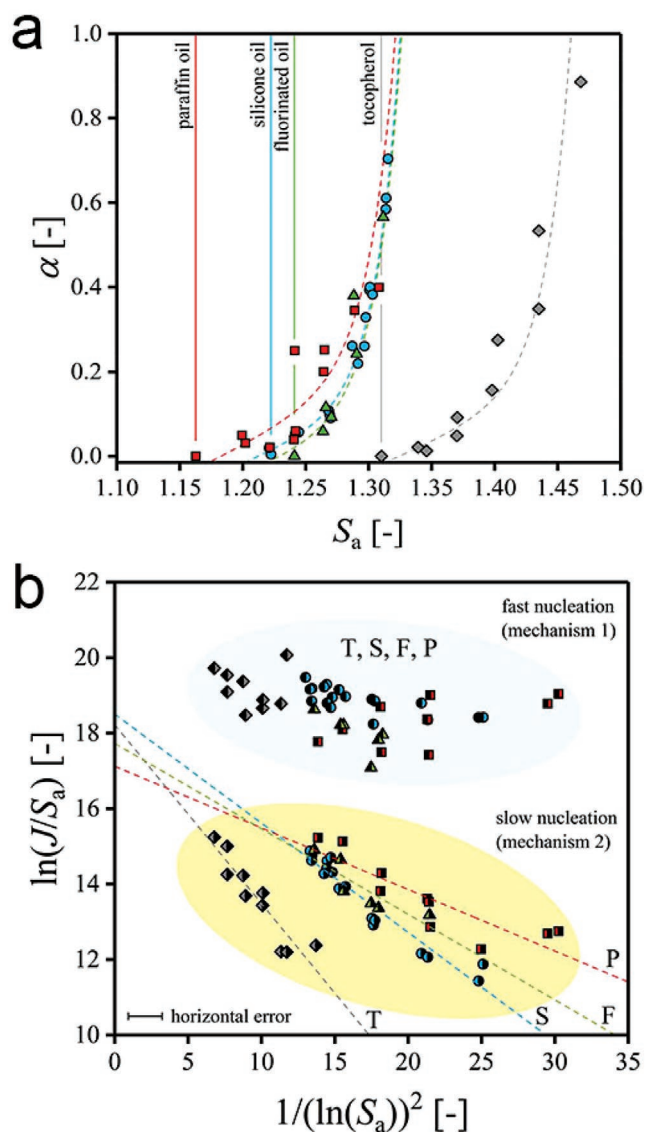


**Figure 12.** a) Fraction of crystallized droplets  $\alpha$  that showed fast nucleation behavior as a function of supersaturation for each combination of dispersed and continuous phase: tocopherol (gray diamonds), silicone oil (blue circles), fluorinated oil (green triangles), and paraffin oil (red squares). Dashed lines are guides to the eye and vertical lines mark the supersaturation at the nucleation onset for each combination of dispersed and continuous phase. b) Volume-specific nucleation rates of mechanism 1 and 2 as a function of supersaturation for each combination of dispersed phase and continuous phase, where the symbols are defined in (a). The dashed lines represent the best linear fits applied to the experimentally determined data obtained for mechanism 2. a,b) Reproduced with permission.<sup>[70]</sup> Copyright 2019, Elsevier.

to the oil employed; in the case of homogeneous nucleation it would depend on supersaturation only. Plots of  $\ln(J/S)$  versus  $1/(\ln S)^2$  for each carrier oil at different supersaturations showed straight line relationships for the slow mechanism, in keeping with Classical Nucleation Theory, from which a unique interfacial energy can be obtained for each oil. No correlation between the rate and supersaturation was observed for the fast nucleation. These data therefore suggest that the droplet interface

promotes nucleation and that true homogeneous nucleation is not observed even in this small droplet system.

### 5.2.5. Droplets in Microcapillaries

Solution plugs can also be created in microcapillaries, where these can provide an excellent opportunity to study a crystallization pathway using optical microscopy.<sup>[165–167]</sup> NaCl crystallization was studied in individual solution plugs in microcapillaries, where maintenance in a controlled humidity environment leads to solution evaporation and the build-up of supersaturation (Figure 13).<sup>[168–170]</sup> A very high supersolubility of  $S \approx 1.6 \pm 0.2$  was recorded, where this compares with the limit of metastability of NaCl of  $S \approx 1.0$  determined from cooling experiments. These highly supersaturated solutions could remain stable for days until a perturbation to the system such as a change in temperature triggers nucleation.<sup>[169]</sup> Crystallization then originates from a single nucleation site and gives rise to a crystal with a hopper (skeletal) morphology that is characteristic of very high growth rates. For NaCl, the transition between cubic and hopper growth occurs at supersaturations that give growth rates above  $\approx 6.5 \pm 1.8 \mu\text{m s}^{-1}$ .<sup>[168]</sup> The higher the supersaturation at the onset of precipitation, the larger the number of interconnected cubic crystals and the number of branches of the hopper morphology.

Surfactants were also added to the system to investigate their effect on NaCl crystallization.<sup>[170]</sup> CTAB (cetyltrimethylammonium bromide) and Tween 80 ( $\text{C}_{64}\text{H}_{124}\text{O}_{26}$ ) both inhibited crystallization such that it occurred at yet higher supersaturations. Unlike the surfactant-free system where crystals nucleated at the air/water interface, individual crystals with star-shaped, hopper-like morphologies nucleated within the volume of the droplet in the presence of the surfactants. This suggests that they passivate the air/water and water/solid interfaces, where no change in the rate of evaporation of the droplets was found in the presence of either surfactant.

### 5.2.6. Droplets on Surfaces

The formation of droplets on surfaces provides an opportunity to study heterogeneous nucleation in well-controlled environments. Importantly, these finite-reservoir conditions can also offer an effective way of studying the crystallization pathway. This has been achieved using patterned SAMs, which can be used to support the formation of arrays of droplets. Stephens et al. used this approach to investigate heterogeneous nucleation of calcium carbonate in small volumes (Figure 14).<sup>[171]</sup> Substrates comprised a regular array of circular, hydrophilic domains (with diameters of 8–20  $\mu\text{m}$ ) in a hydrophobic background and were prepared by immersing a mica substrate supporting an evaporated gold film in a solution of fluoroalkylthiols. The film was then irradiated with deep UV through a suitable mask, and washed to remove the oxidized thiols. Immersion in a solution of carboxyl-terminated thiols then generated the patterned SAM. Arrays of picoliter droplets could then be generated by rolling a large drop of solution over the SAM under controlled humidity.



**Figure 13.** a) Spontaneous growth of hopper crystals at supersaturation  $S \approx 1.6$ , in capillary of  $100 \mu\text{m}$  (top). Evolution of the growth of a hopper crystal over 10 min (bottom). Reproduced with permission.<sup>[169]</sup> Copyright 2014, American Chemical Society. b) Multibranch hopper formed in NaCl solution with CTAB (top) and the solution with Tween 80 (bottom). c, d) Schematic of a one branch and multibranch hopper crystal, respectively. b) Reproduced with permission.<sup>[170]</sup> Copyright 2017, American Chemical Society. c, d) Adapted with permission.<sup>[170]</sup> Copyright 2017, American Chemical Society.

Calcium carbonate was precipitated by either using a metastable solution of calcium carbonate to form the droplets, or using a  $\text{CaCl}_2$  solution and then exposing the substrate to ammonium carbonate vapor. The humidity was carefully controlled such that the droplets did not undergo evaporation. Comparable results were obtained in both cases. Examination of the system after 24 h revealed that most droplets only contained a single crystal of calcite, where these were principally oriented

with (012) or (015) basal planes (Figure 14a). By comparison, immersion of the patterned SAM in bulk solution generated an average of seven crystals in each hydrophilic domain, in the same orientations as occurred in the droplets (Figure 14b). The crystals formed in the droplets were also considerably smaller (basal areas of  $\approx 1.2 \mu\text{m}^2$ ) than those formed in bulk ( $>20 \mu\text{m}^2$  basal area) and were tetrahedral in form as compared with the rhombohedral morphologies that formed in bulk (Figure 14c, d).

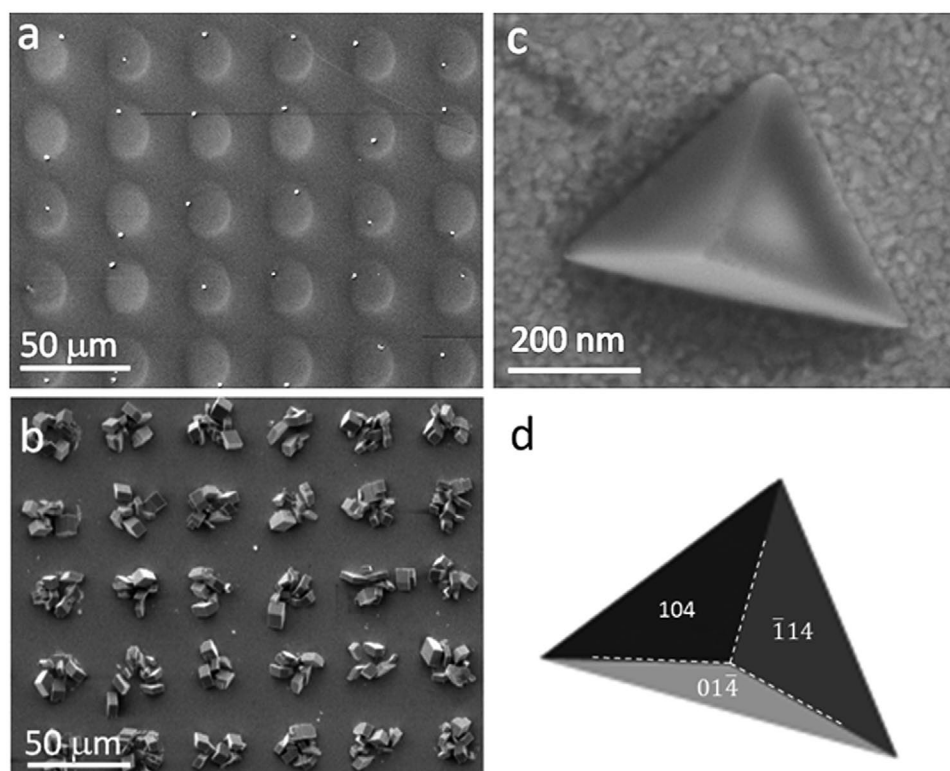


**Figure 14.** a, b) SEM images showing  $\text{CaCO}_3$  precipitated from single droplets (a) and bulk solution (b) onto surfaces patterned with  $10 \mu\text{m}$  radius circles. c) Calcite tetrahedron precipitated within a single  $5 \mu\text{m}$  radius droplet after 24 h, oriented with a {012} nucleation face. d) A simulated calcite tetrahedron oriented with a {012} nucleation face, as defined by a single threefold axis with projected angles of 142, 104, and 104. a–d) Reproduced with permission.<sup>[171]</sup> Copyright 2011, American Chemical Society.

These effects are readily rationalized. The limited quantity of reactant ions present in the droplet limits the growth of the crystal such that it is effectively “frozen” at an earlier stage of growth than in bulk solution. That calcite initially forms as tetrahedra can be attributed to the favorable interaction between the crystal and substrate, such that the crystal initially grows to maximize the interfacial area. The influence of the substrate reduces as the crystal grows, such that it ultimately develops a rhombohedral morphology.<sup>[172]</sup> The droplets were also used as a means of studying the crystallization process at very early times, where crystallization proceeded more slowly in these environments than in bulk solution. Ex situ analysis using SEM showed that ACC particles formed initially, and then aggregated on the substrate. Crystallization then occurs preferentially at the SAM, yielding first irregular particles and then well-defined calcite tetrahedra at particle sizes of  $\approx 100$  nm. No rhombohedra with dimensions of  $< 200$  nm were ever observed.

Arrays of droplets on patterned SAMs have also been used to study crystallization due to evaporation of droplets.<sup>[173–179]</sup> Patterned substrates comprising hydrophilic metal islands in a hydrophobic background were created by evaporating the metal (Ti/Au) through a mask onto a glass substrate, and then back-filling the background by immersion in octadecyltrichlorosilane. The gold areas were functionalized using 4-mercaptobenzoic acid. Droplets can then be formed on the hydrophilic domains by immersing the substrate in, and slowly withdrawing it from an aqueous solution of the compound of interest.

Investigation of glycine crystallization using this system demonstrated that just one crystal formed within individual domains of size 25–725  $\mu\text{m}$  and that the  $\alpha$ -form exclusively formed in the largest droplets, and the  $\beta$ -form in the smallest.<sup>[174]</sup> The emergence of the  $\beta$ -form can be attributed to the high supersaturation arising from the rapid evaporation of the small droplets. This was supported by experiments in which the evaporation rate was controlled by immersing the newly formed droplet array in oil.<sup>[173]</sup> The significantly reduced evaporation rate resulted in the formation of the  $\alpha$ -polymorph in the small droplets. This system was also used to investigate the crystallization of mefenamic acid and sulfathiazole<sup>[176]</sup> within small droplets. Again, the polymorphs formed were dependent on the rate of evaporation and the initial concentrations of the solutions, and multiple polymorphs could form within single droplets demonstrating the roles of competing kinetic and thermodynamic factors.

These droplet arrays have also been used to explore polymorphism,<sup>[179]</sup> and the influence of pH.<sup>[175]</sup> Investigation into polymorph formation exploited the fact that this droplet system makes it possible to rapidly perform huge numbers of experiments in parallel. Using ROY as a suitable test case, Singh et al. carried out 10 000 experiments,<sup>[179]</sup> and in doing so, they were able to observe 6 out of the 7 stable polymorphs of ROY under identical reaction conditions. Initial experiments with 1500 droplets yielded crystals of 4 of the polymorphs, and a fifth form in one droplet only. Expansion of the number of experiments to 10 000 was sufficient to observe a sixth polymorph in a small number of droplets. Notably, three of the polymorphs were obtained on less than 1% of the islands. Therefore, only by carrying out huge numbers

of experiments was it possible to observe low stability polymorphs. Determination of size-dependent solubility provides an additional application of droplet arrays, where the concentration of the droplet and rate of change of supersaturation can be varied to generate crystals of different sizes.<sup>[178]</sup> The solubility of glycine crystals was determined by investigating their solubility in glycine solutions with different concentrations.

Inject printing provides an alternative method for depositing individual droplets of sizes 5–200 pL on substrates, and can be used to generate crystals with different structures.<sup>[180–182]</sup> Droplets generated in this way have been explored for studies of the effects of confinement on the crystallization of a number of polymers<sup>[180]</sup> and organic compounds<sup>[183,184]</sup> on different substrates. Glycine was precipitated on evaporation of droplets of sizes 100 pL to 0.1  $\mu\text{L}$  on glass and aluminum substrates, where larger droplets were created by merging the small droplets.<sup>[184]</sup> All droplets in this size regime yielded the metastable  $\beta$ -phase. By comparison, a mixture of the  $\alpha$ - and  $\beta$ -polymorphs formed in larger droplets generated using a micropipette. The crystallization of D-mannitol was also investigated and the stable  $\beta$ -polymorph formed on evaporation of the smallest 100 pL droplets, while both metastable  $\alpha$ - and  $\delta$ -polymorphs in larger droplets up to 200 nL size.<sup>[183]</sup> Larger droplets of 60  $\mu\text{L}$  created using a micropipette also showed evidence of the  $\beta$ -form in addition to the least stable  $\delta$ -polymorph.

## 6. Surfactant Assemblies

Surfactant assemblies such as reverse micelles and microemulsions can be employed as nanoscale reaction environments and have been widely used to synthesize nanoparticles of a wide range of materials.<sup>[185–191]</sup> These systems are inherently dynamic such that crystal growth continues over time due to the exchange of reactants between individual micelles. Nanoparticles must therefore either be isolated from solution, or capping agents added to terminate growth at specific nanoparticle sizes. These surfactant systems can also yield unusual crystal morphologies, such as wires of calcium sulfate,<sup>[192,193]</sup> barium sulfate,<sup>[194]</sup> and calcium carbonate.<sup>[195]</sup> While providing some fascinating examples of control over crystallization, the dynamic nature of these systems means that they can be difficult to employ in systematic studies of confinement. Vesicles, in contrast, provide isolated reaction volumes and can be generated with diameters ranging from around 20 to 200  $\mu\text{m}$ . These are therefore better suited to studies of confinement, although it can be challenging to obtain high reactant concentrations—and therefore significant crystallization—within these self-assembled environments. This section therefore describes studies whose focus has been on the use of surfactant assemblies to conduct investigations into the effects of confinement on crystallization.

### 6.1. Microemulsions

An elegant demonstration of the potential of achieving thermodynamic control over crystallization in small, finite volumes has

been provided by experiments utilizing microemulsions, where the extreme confinement provided by these environments was used to select crystal polymorph.<sup>[87,196,197]</sup> As described in Section 5.1, crystallization within highly constrained, isolated environments leads to a substantial depletion in the supersaturation as the nucleus grows, leading to a minimum in the free energy with respect to the nucleus size.

Comparing this effect for two polymorphs, a more stable polymorph (A) is less soluble than a polymorph of lower thermodynamic stability (B), and therefore grows to a larger size before the supersaturation is depleted (Figure 15). The minima in the free energy curves  $\Delta F_{\min}^*$  therefore occur at  $r_{\min}^*$  (A) >  $r_{\min}^*$  (B) and it is expected that  $\Delta F_{\min}^*$  (A) <  $\Delta F_{\min}^*$  (B). The population of  $r_{\min}^*$  nuclei at equilibrium then depends upon the Boltzmann factor,  $\exp(-\Delta F_{\min}^*/kT)$ . When  $\Delta F_{\min}^* > kT$ , the system is stabilized due to confinement effects and no crystallization occurs. Under conditions where  $\Delta F_{\min}^* \leq kT$ , a population of (near) stable nuclei are produced such that thermodynamic control over polymorph can be achieved when polymorph A, but not polymorph B, has  $\Delta F_{\min}^* \leq kT$ . Polymorph A—but not polymorph B—can then form a significant population of nuclei, provided that the nucleation energy barrier to formation of this phase is surmountable. The latter can be achieved under the conditions of high initial supersaturation that can be achieved in small droplets. Finally, conditions where  $\Delta F_{\min}^* \leq kT$  for both polymorphs will lead to a mixture of crystal forms.

The possibility of using this framework for gaining thermodynamic control over crystal polymorph was tested against the crystallization of glycine, ROY, and mefenamic acid. Conditions where crystallization occurred within droplets to yield nuclei of the stable polymorph, but negligible quantities of other polymorphs were identified by initially creating a supersaturated system that is stabilized in confinement such that negligible numbers of (near) stable nuclei are present ( $\Delta F_{\min}^* > kT$ ). Subsequent increase in the supersaturation then yields conditions where only (near) stable nuclei of the stable polymorph form in significant quantities. Further growth of the crystals then occurs as the microemulsions collide and their contents merge. Analysis of all three systems using small-angle X-ray scattering (SAXS) demonstrated that the population of as-synthesized microemulsions had average core radii of  $\approx 2\text{--}4$  nm.

Mefenamic acid crystallizes as two polymorphs under ambient conditions, rather creatively termed Form I (stable) and Form II (metastable). While crystallization of mefenamic acid from dimethylformamide (DMF) in bulk solution invariably yielded Form II, the polymorph formed on cooling microemulsions of mefenamic acid/DMF in heptane/sodium dioctyl sulfosuccinate (also known as AOT) depended on the initial supersaturation of the mefenamic acid/DMF solution. Crystallization was extremely slow at an initial supersaturation ratio of  $C/C_{\text{sat}} = 4.1$ , while crystals were principally Form I at  $C/C_{\text{sat}} = 4.1\text{--}5.3$  and increasing quantities of Form II crystals formed at higher supersaturations. Further investigation of this system showed that the Form II crystals grew much faster than those of Form I. Form I crystals could be exclusively obtained from compositions that initially yielded a mixture of Form I and Form II crystals by gently heating the microemulsions to preferentially dissolve Form II.<sup>[196]</sup>

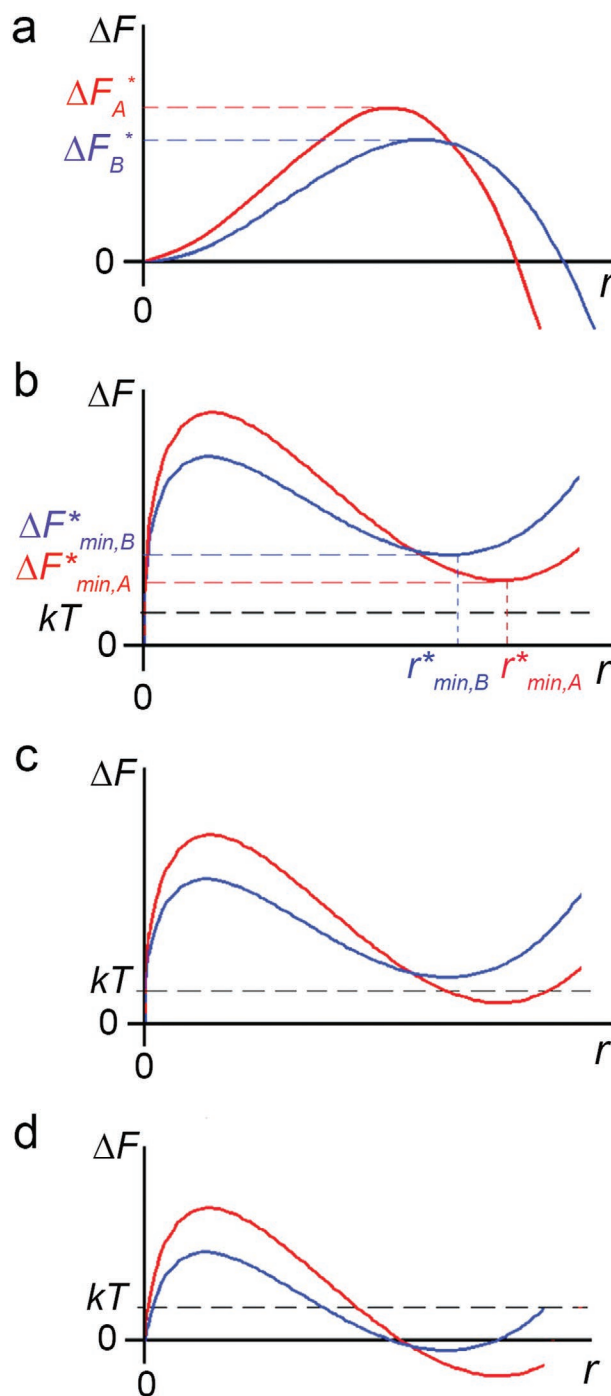


**Figure 15.** The change in free energy as a function of nucleus size for systems crystallizing from a) bulk solution and b–d) nanoconfined solution. a) Ostwald's rule of stages is obeyed as the metastable polymorph B (blue) crystallizes before the stable polymorph A (red). b) Crystallization is not favored and the system is stabilized due to confinement. c) Only polymorph A will crystallize due to the thermodynamic control, whereas in (d) this control is lost leading to the crystallization of both polymorphs. a–d) Reproduced with permission.<sup>[87]</sup> Copyright 2011, American Chemical Society.

Glycine, in turn, forms as  $\alpha$ ,  $\beta$ , and  $\gamma$  polymorphs under ambient conditions where the  $\gamma$ -polymorph is the stable form.

However, it is very difficult to precipitate  $\gamma$  form from neutral solutions in the absence of additives as the  $\alpha$  form is only slightly less stable, but exhibits a much higher growth rate. Crystallization of glycine in microemulsions was achieved by combining a microemulsion of an aqueous solution of glycine in heptane, stabilized with Span 80 (sorbitan monooleate) and Brij 30 (polyethylene glycol dodecyl ether), with one solubilizing water/methanol. Again, low supersaturation conditions yielded the  $\gamma$  glycine polymorph alone, while increasing quantities of the  $\alpha$  polymorph formed as the initial concentration of glycine was increased. Extension of the experiments to use AOT as the surfactant yielded the  $\gamma$  polymorph at a lower supersaturation than with Span/Brij, where this was attributed to a stabilizing interaction between the AOT molecules and developing nucleus.<sup>[197]</sup> Investigation of the ROY system—which has ten known polymorphs—further supported the hypothesis, where the most stable Y prism form could be generated from microemulsions of a toluene solution of ROY in heptane/Igepal (polyoxyethylene (12) isooctylphenyl ether), under control of supersaturation. Higher supersaturations yielded mixtures of YN, R, ON, and Y crystals.

Analysis of these systems shows that the average number of solute molecules within each droplet is in the order of 2–5, such that crystallization can only occur in the largest droplets with the highest supersaturations. Indeed, given a free energy difference of 0.2 kJ mol<sup>-1</sup> between the  $\alpha$  and  $\gamma$  polymorphs of glycine, a thermodynamic preference will occur when the (near) stable nuclei contain  $\approx$ 20–30 glycine molecules. Assuming a Poisson distribution of glycine molecules among the droplets, only 10<sup>-8</sup> of them are predicted to contain sufficient glycine molecules to support nucleation of the  $\gamma$  polymorph.

## 6.2. Vesicles

Biom mineralization processes invariably occur within privileged environments, where an organism can define and localize where mineralization occurs, and exert control over mineralization, for example, by introducing different soluble additives at different time points. Liposomes (vesicles bounded by a phospholipid membrane) provide a convenient model of biom mineralization systems, and have often been used as environments to precipitate materials such as calcium carbonate,<sup>[198,199]</sup> iron oxides,<sup>[200–202]</sup> and calcium phosphate.<sup>[203–205]</sup> The cations are typically encapsulated within the liposomes, and precipitation is then initiated either by diffusion of a gaseous reagent across the lipid bilayer or through a pH change in the bulk medium. The particles formed within the liposomes invariably differ from those precipitated in bulk solution, where this has been attributed to the small volume of solution (and thus limited availability of reactant ions) and interaction with the vesicle membrane.

Liposomes with well-defined sizes have also been used as an excellent system for systematically investigating the effect of confinement on the precipitation of calcium carbonate, and in particular on the transformation of ACC.<sup>[206–209]</sup> Unilamellar diphosphatidylcholine (DPPC) liposomes were generated by extrusion of multilamellar vesicles, prepared in the presence of 1 M CaCl<sub>2</sub> solution, through track-etched membranes with

pores of diameter 1  $\mu$ m, 500 nm, or 200 nm.<sup>[206]</sup> Calcium ions external to the vesicles were removed by size exclusion chromatography and calcium carbonate precipitation was then induced by addition of ammonium carbonate to the suspension of vesicles, or by placing the liposome suspension in a closed environment with solid ammonium carbonate. Examination of the liposomes using cryo-TEM or cryo-scanning TEM (STEM) demonstrated that only one particle formed in liposomes with 200 nm diameters, and that they did not appear to be associated with the liposome membrane. An identical result was obtained for liposomes containing up to 20 wt% phosphatidylinositol (PI), which exhibits a negative charge and hydroxyl groups that are known to bind and stabilize ACC. Analysis of the intravesicular precipitate demonstrated that it was amorphous and had no well-defined morphology. Notably, no crystallization was observed within the 20 h time-span of the experiment, in marked contrast to the rapid precipitation of crystalline calcite in control experiments performed in bulk solution. Characterization of larger liposomes using TEM was challenging due to their sizes, but all of the particles formed within the vesicles were amorphous for the duration of the experiment.

This strategy was then extended to giant unilamellar DPPC liposomes with diameters of 20–50  $\mu$ m (Figure 16).<sup>[208]</sup> Large aggregates of spherical ACC particles with diameters of  $\approx$ 650 nm formed within these vesicles and were stable for over 8 days. Confirmation that the stabilization is due to confinement effects was obtained by lysing the liposome using detergent. Rapid precipitation and dissolution of the ACC occurred when the vesicle was opened. Comparable experiments were also performed with SrCO<sub>3</sub> and BaCO<sub>3</sub> to explore the generality of these findings. A transient amorphous precursor was observed for the SrCO<sub>3</sub> system, which transformed to crystalline strontianite within 5–10 min. No amorphous material was seen with BaCO<sub>3</sub>, and crystalline witherite formed after  $\approx$ 1 min.

The extended lifetime of ACC within these liposomes can be attributed to the exclusion of impurities from these confined environments.<sup>[208,209]</sup> ACC precipitates rapidly within the vesicles, indicating a low energetic barrier to formation, or indeed no barrier at all if it forms via spinodal decomposition.<sup>[101]</sup> The composition of the solution within the vesicles is then defined by the solubility of ACC. Transformation of the ACC to calcite is then dependent on the initial formation of a calcite nucleus, which can subsequently grow, fed by dissolution of the ACC. However, the barrier to homogeneous nucleation of calcite is extremely high under these conditions. With an interfacial free energy of 109 mJ m<sup>-2</sup>,<sup>[210,211]</sup> an energy barrier of 93 kT is predicted at the solubility limit of ACC.<sup>[212]</sup> Therefore, only heterogeneous nucleation will enable crystallization to occur on a reasonable time-frame. That both strontianite and witherite crystallize in minutes within the vesicles suggests that both possess much smaller energy barriers to nucleation as compared with the crystalline CaCO<sub>3</sub> polymorphs.

## 7. Nanoscale Cylindrical Pores

Matrices possessing cylindrical pores have been extensively used to investigate the effects of confinement on crystallization. These are categorized here into two main groups: 1) individual

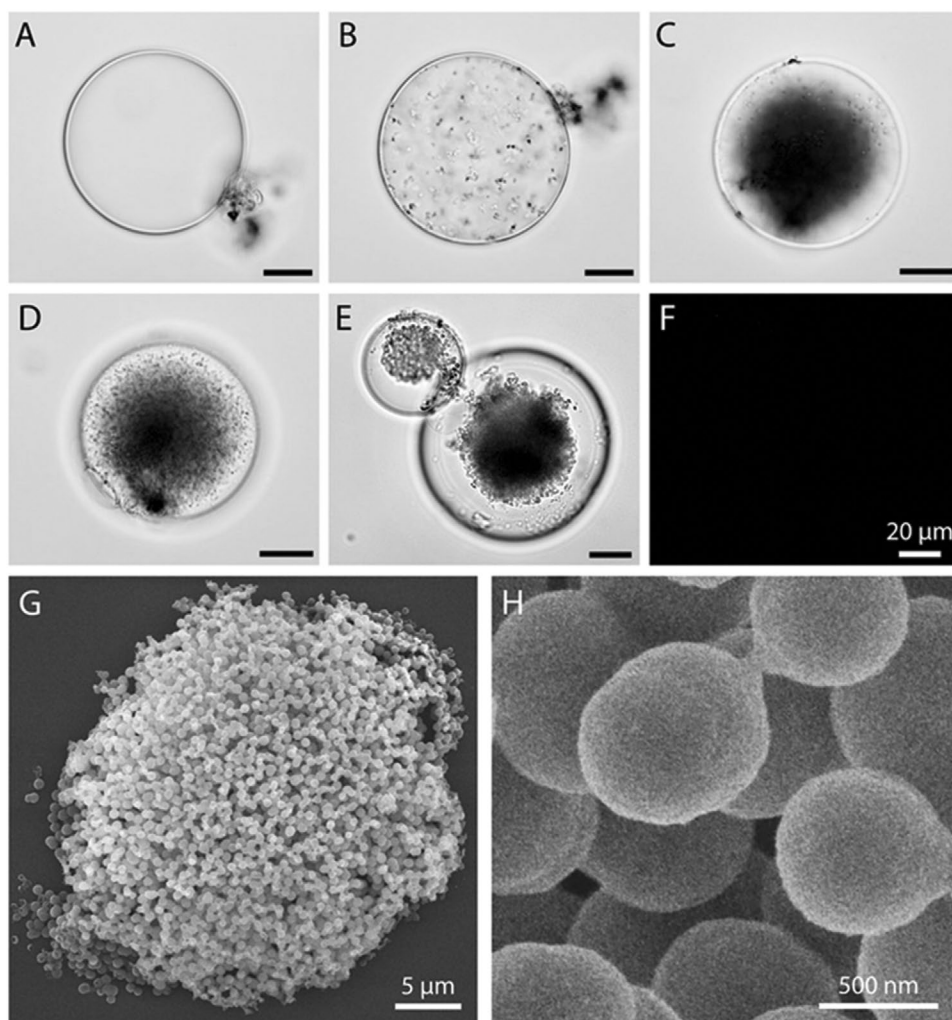


**Figure 16.** Optical microscopy images of Ca<sup>2+</sup>-loaded PC liposomes. A) Before the addition of (NH<sub>4</sub>)<sub>2</sub>CO<sub>3</sub>. B) Initial precipitation of particles within 5 min of addition. C, D) Aggregation and sinking of particles within 2 h (shown as two different focal planes). E, F) Condensation of aggregate with a rough surface, but is not birefringent. G, H) SEM images of an isolated aggregate consisting of 650 ± 5 nm diameter sized nanoparticles. A–H) Reproduced with permission.<sup>[208]</sup> Copyright 2014, Royal Society of Chemistry.

nanotubes that can offer true nanoscale confinement, and 2) matrices containing parallel arrays of cylindrical pores or entwined networks of cylindrical pores. These are extremely versatile and provide the opportunity to systematically study the effects of confinement over length scales ranging from the atomic- to the micrometer-scale (as defined by the pore diameter), and in many cases the surface chemistry can also be modified. Depending on the system, crystallization processes can be followed within individual pores, or measurements are recorded as an average over a population of pores. Crystals can be analyzed within, or after extraction from the pores, and a wide range of analytical techniques can be employed. While many of these systems have been used to synthesize nanomaterials with different morphologies and sizes, the focus here is on studies of confinement effects on crystallization processes. The growth of organic crystals in the confines of these systems has been described in a number of excellent reviews.<sup>[213,214]</sup>

### 7.1. Atomic Scale Confinement—Carbon Nanotubes

With internal diameters of just a few nanometers, carbon nanotubes offer true atomic-scale confinement. They are electron transparent such that they—and the compounds they contain—can be readily characterized using high resolution TEM (HRTEM). Data can also be obtained from an individual nanotube rather than as an average over a population of environments. Carbon nanotubes therefore provide a unique opportunity to characterize the effects of atomic-scale confinement on the assembly of matter, where the positions of individual atoms can be determined. Nanotubes with diameters of 1–2 nm have dimensions comparable to the unit cells of many compounds and therefore have many effects on the structures of the internal compound including lattice distortions,<sup>[215,216]</sup> the formation of structures not seen under analogous bulk conditions,<sup>[217,218]</sup> and even the generation of new crystal phases.<sup>[219–221]</sup>



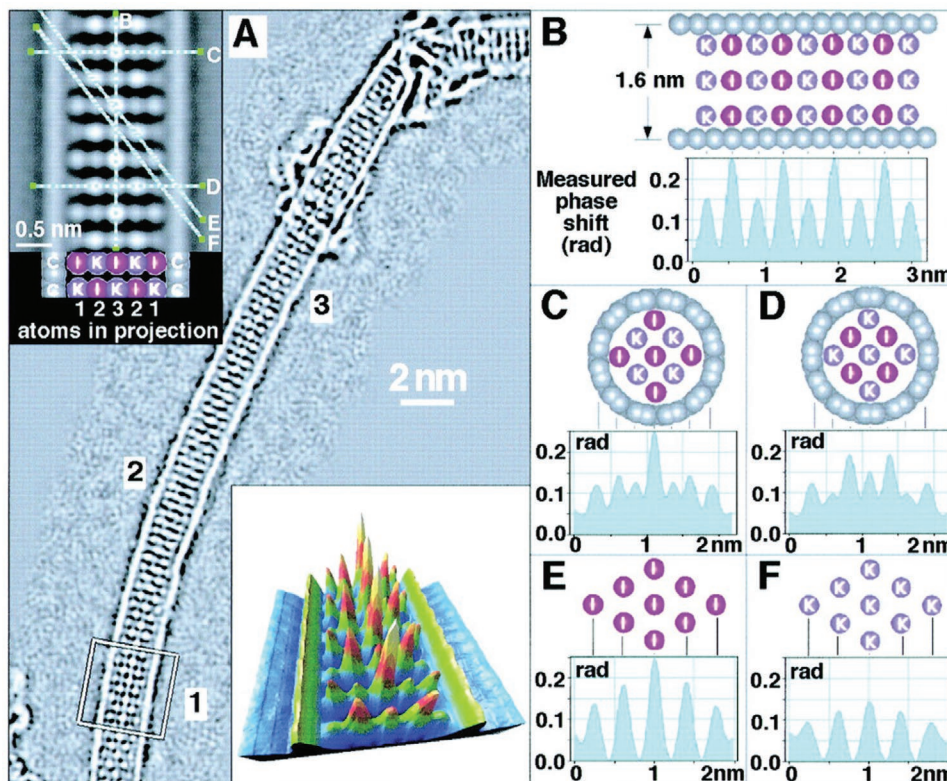


**Figure 17.** A) Phase image showing a  $\langle 110 \rangle$  projection of KI incorporated within a 1.6 nm diameter SWCNT, reconstructed from a focal series of 20 images. Maximum and minimum spatial frequencies of  $1/(0.23 \text{ nm})$  and  $1/(1.05 \text{ nm})$ , respectively, have been retained with a Wiener filter. The upper left inset shows an enlargement of region 1 (symmetrized about the chain axis) and a schematic illustration depicting alternating arrangement of I–2–3I–2K–I and K–2I–3K–2I–K  $\{100\}$  layers within the crystal. The lower right inset shows the surface plot of region 1. B–F) Single-pixel line profiles obtained from line traces marked B to F in the upper left inset in (A). The background level in these profiles is arbitrary because the reconstruction procedure does not recover low-spatial-frequency variations in phase. Schematic crystal structures showing atoms contributing to the contrast are also shown. A–F) Reproduced with permission.<sup>[215]</sup> Copyright 2000, AAAS.

Following the discovery<sup>[222]</sup> and successful production of high yields<sup>[223]</sup> of concentric, cylindrical multiwalled carbon nanotubes (MWCNTs) in the early 1990s, extensive work has been conducted to fill these structures with different compounds to generate novel nanocomposite materials. A range of strategies have been developed, where the Young–Laplace equation predicts that only compounds with surface tensions  $< 200 \text{ nN m}^{-1}$  are able to enter the CNT through capillary action at atmospheric pressure.<sup>[224]</sup> Liquids with high surface tensions (e.g., metals) can therefore only enter under an applied pressure, or under oxidative conditions where the metal reacts with the oxygen or carbon to create a compound with reduced interfacial tension.<sup>[224]</sup>

Early studies focused on filling nanotubes with metals,<sup>[225–227]</sup> metal oxides,<sup>[228–232]</sup> metal carbides,<sup>[226,233,234]</sup> and metal salts,<sup>[235–237]</sup> where these and subsequent studies have been summarized in a number of review articles.<sup>[238–240]</sup> Similar experiments have also been carried out using alternative nanotubes including the formation of single crystal nanowires of potassium halides in BN nanotubes,<sup>[241]</sup>  $\text{PbI}_2$  in BN,<sup>[242]</sup>  $\text{MoS}_2$ ,<sup>[242]</sup> and  $\text{WS}_2$  nanotubes,<sup>[243]</sup> and CsI in  $\text{WS}_2$  nanotubes.<sup>[244]</sup>

One of the systems that has received the most attention is the crystallization of KI within single walled carbon nanotubes (SWCNTs). KI was deposited within  $\approx 1.6 \text{ nm}$  SWCNTs by

heating a mixture of the nanotubes with molten KI at 954 K. Analysis of the deposited KI using HRTEM demonstrated that the structure was based on the rocksalt structure of the bulk phase and that it grew with its  $\langle 001 \rangle$  direction parallel to the long axis of the tube (Figure 17).<sup>[215]</sup> Perpendicular to this direction, the  $\{001\}$  layers alternate between 1I–2K–3I–2K–1I and 1K–2I–3K–2I–1K. The central K–I–K–I row therefore experiences the 6:6 coordination of the bulk structure, while the atoms on the face and edges have reduced coordinations of 5:5 and 4:4, respectively. The reduced coordination is associated with distortions in the lattice, where the crystal is contracted along the  $\langle 001 \rangle$  direction, while the cross-section is distorted from a square with a greater expansion along the  $\langle 100 \rangle$  than the  $\langle 110 \rangle$  direction.

SWCNTs with yet smaller internal diameters of  $\approx 1.4 \text{ nm}$  further constrained the growth of KI crystallites such that they were just 2 atomic layers thick and the ions were entirely 4 coordinate.<sup>[216]</sup> These are therefore “surface only” and contain no internal ions. These crystallites exhibited the same orientation with the  $\langle 001 \rangle$  parallel to the pore axis and a marked expansion perpendicular to their long axis.

The simplicity of these systems is such that simulations can be performed to gain insight into the structures of KI crystallites formed within SWCNTs, and the mechanism by which

liquid KI fills nanotubes.<sup>[245–247]</sup> The minimum energy structures of KI crystals that are two ( $2 \times 2$ ) and three ( $3 \times 3$ ) atoms wide were calculated when they were embedded within nanotubes of various diameters or within nanotubes surrounded by amorphous KI, and also unconstrained. In both cases, the constituent atoms in the unconstrained crystals experienced distortions that were in the same direction, but much smaller than those observed experimentally. For the ( $2 \times 2$ ) cluster this represents an expansion perpendicular to its major axis, while the ( $3 \times 3$ ) cluster experiences a contraction.

Looking at the ( $2 \times 2$ ) crystallites within nanotubes of differing internal diameters, crystallites within 1.09 nm nanotubes experience a compression perpendicular to the main axis, while an expansion is observed in 1.26 nm nanotubes. This can be explained in terms of the ion-carbon separations in these nanotubes, where the smaller separations in the 1.09 nm nanotubes fall in the attractive regime, and the larger separations in the 1.26 nm nanotubes the repulsive regime. Embedding the 1.26 nm nanotubes within molten KI then significantly affects the distortions, where the ion-ion interactions are sufficiently long-range that the ions within the nanotube are influenced by those on the outside. This induces further compression perpendicular to the main axis and yields distortions very close to those obtained experimentally. The ( $3 \times 3$ ) crystal, in contrast, must be significantly compressed for it to be inserted into a 1.63 nm nanotube.

Considering then the mechanism driving crystallization within the nanotubes, a number of possibilities can be considered. The small pore size is expected to lead to an increase in the melting point such that crystallites preferentially form in the small pores. The strong ion-ion bonding in molten KI is also such that the Coulombic interactions between ions within the nanotube drive the formation of a crystalline structure, and amorphous phases are energetically inaccessible.<sup>[245]</sup>

The role of the ratio of K to I ions on the structure of the confined crystallite has also been considered.<sup>[248]</sup> Deposition of KI within nanohorns with internal pore diameters  $<2$  nm was achieved by heating them with KI in a sealed cell at 1073 K. HRTEM analysis revealed that the high pressure phase (CsCl structure) formed rather than the rocksalt structure expected under ambient pressure conditions.<sup>[248]</sup> Calculations to evaluate the energetics of this system suggested that the structure type may derive from different ratios of K and I within the nanopores.<sup>[249]</sup> To maintain stoichiometry, the rocksalt KI structure must be oriented with its [001] direction parallel to the long axis of the nanotube, while the CsCl structure must be  $[111]$  oriented. The rocksalt structure was found to be the more energetically stable for all of the nanotube radii considered. However, under conditions where an imbalance occurs in the number of K and I atoms within the nanotube—which can arise as an effect of the confinement—the high pressure CsCl phase is then energetically favored. This effect is then lost as the pore diameter increases and stoichiometry is obtained.

Confinement within nanotubes can also drive the formation of structures not seen in bulk systems, where reduced anion and cation coordinations are common. While bulk  $\text{TbCl}_3$  consists of  $\text{TbCl}_6$  polyhedra organized in a 3D hexagonal network, a 1D chain of edge-sharing  $\text{TbCl}_6$  octahedra forms within a 1.6 nm SWCNT.<sup>[250]</sup> This structure forms with a reduced

rearranged anion sublattice, but retains the cation sublattice of the bulk halide. In bulk,  $\text{BaI}_2$  crystallizes in a number of structures comprising a 3D network of trigonal prisms.<sup>[251]</sup> Within 1.6 nm SWCNTs, in contrast, a 1D chain consisting of edge-linked coordination polyhedra is formed in which the barium ions exist in 5 and 6 coordinations; neither of these occur in bulk  $\text{BaI}_2$ .  $\text{CoI}_2$  confined within SWCNTs, in turn, exhibits a unique helical structure based on a twisted, double chain of  $\text{Co}_2\text{I}_4$  units within SWCNTs.<sup>[252]</sup> Measurement of the diameter of the nanotubes then revealed that they also undergo an elliptical distortion in correspondence to the  $\text{CoI}_2$  crystal, which is indicative of a strong interaction between the confined crystallite and the supporting nanotube.

These effects have also been observed for monoatomic systems. Deposition of iodine within SWCNTs yielded a single chain of iodine atoms with helical form in nanotubes with internal diameters of  $\approx 1.05$  nm,<sup>[221,253]</sup> where the chains can move when irradiated by the electron beam.<sup>[221]</sup> The SWCNTs then accommodated two, and then three helices as the diameter increased to 1.4 nm, where the helical pitches often varied within a single nanotube (Figure 18). The iodine atoms are incorporated as negatively charged  $\text{I}^{3-}$  or  $\text{I}^{5-}$  species such that the charge on the iodine atoms causes repulsion between the helices and an elliptical distortion of the nanotube. SWCNTs with diameters larger than 1.45 nm supported the formation of crystalline iodine. HRTEM revealed dynamic interchange between three phases, where at least three helical atomic chains of iodine (termed Phase I) could reversibly crystallize into Phases II and III during imaging. Phase II is a highly distorted form of the recognized orthorhombic structure, while Phase III is a completely new structure. The orthorhombic phase of bulk iodine was finally observed in nanotubes with diameters of 1.55 nm.

That the rigidity of the wall of the nanotubes can play a role in structure determination has been shown through the deposition of  $\text{PbI}_2$  within SWCNTs and double-walled carbon nanotubes (DWCNTs) of different dimensions, where DWCNTs

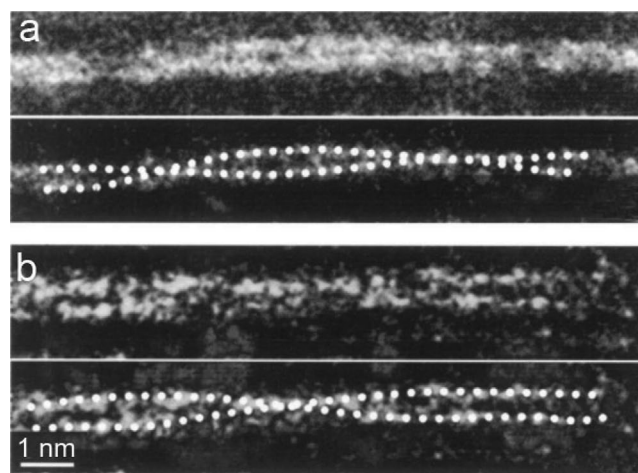


**Figure 18.** Images of iodine-doped SWNT ropes showing different periodicities, where TEM images are shown at the top and the corresponding schematic is shown at the bottom of each pair of images. a) An iodine helix showing 12–13 nm periodicity and b) a helix of longer periodicity. a,b) Reproduced with permission.<sup>[253]</sup> Copyright 2000, American Physical Society.

are more rigid than their single wall counterparts.<sup>[254,255]</sup> PbI<sub>2</sub> exhibits a complex layered structure and can exist in a range of polytypes.<sup>[220]</sup> The 2-H polytype was observed to form in both types of nanotube, as compared with the 4-H form which readily forms in bulk. However, PbI<sub>2</sub> did not crystallize in DWNTs with internal diameters of less than 2 nm, although crystalline material was readily obtained in SWNTs with comparable diameters. This can be attributed to the rigidity of the DWNTs, such that they cannot distort to accommodate asymmetric crystal fragments.

DWCNTs have also been used to create rigid nanopores with such small internal diameters—under 1 nm—that true atomic chains of atoms can be created. Chains of CsI that comprised alternating Cs<sup>+</sup> and I<sup>-</sup> ions were observed in such environments, where the structures of the chains were confirmed using annular dark field (ADF) imaging and electron energy loss spectroscopy (EELS) chemical mapping.<sup>[256]</sup> Linear chains were observed in the smallest nanotubes, while some distortion occurred in larger diameter tubes due to the attraction of the positively charged Cs<sup>+</sup> ions, and repulsion of the negatively charged I<sup>-</sup> ions to the walls of the CNT. Single chains of Eu atoms have been reported in 0.76 nm pores, as compared with FCC-structured nanowires in 1.06 and 1.54 nm nanotubes. Bulk Eu has a BCC structure. Chains of individual Mo atoms were also reported within 0.6–0.8 nm DWCNTs,<sup>[257]</sup> but further examination of this system demonstrated that DWCNTs with inner diameters of 0.7–1 nm actually supported the formation of nanowires whose unit cell is a subunit of a BCC structure and comprises just 4 atoms rather than linear chains.<sup>[258]</sup>

## 7.2. Matrices with Multiple Cylindrical Pores

Commercially available porous media including AAO membranes, polycarbonate track-etched (TE) membranes, and nanoporous glasses provide excellent media for studying crystallization in confinement (**Figure 19a,b**). A number of polymer monoliths that have been fabricated to contain cylindrical pores have also been employed for confinement studies. The majority of studies have focused on organic compounds, where their high solubility in many solvents makes it possible to achieve high loadings into the pores, and to generate crystals uniquely within the pores and not on the surface of the porous medium. Many organic compounds also exhibit a rich polymorphism, and phase transformations can be studied using scanning calorimetry. They therefore offer an interesting test case for investigating the effects of confinement on crystallization.

AAO membranes have been used extensively to template inorganic nanorods and nanotubes of a wide range of materials including metals, metal oxides, and semiconductors.<sup>[259–267]</sup> They are particularly attractive due to their thermal and chemical stability and because they exhibit a high density of cylindrical pores.<sup>[24]</sup> They can also be readily manufactured in the lab and obtained commercially with a wide range of pore sizes. TE membranes are an alternative, commercially available filtration membranes that are perforated with cylindrical channels with diameters from ≈10 nm to tens of micrometers. These are usually supplied coated with poly(vinylpyrrolidone) (PVP) to increase

hydrophilicity, but can be purchased uncoated. Although offering a significantly lower density of pores than AAO membranes, they have been used to template single crystal and polycrystalline nanorods of materials including ZnO, CuO, and α-Fe<sub>2</sub>O<sub>3</sub> (hematite),<sup>[268]</sup> alkaline earth fluorides,<sup>[269]</sup> and Tb-doped CePO<sub>4</sub>.<sup>[270]</sup> With the ability to readily dissolve the membrane in organic solvents, and therefore release the intrapore crystals for analysis using techniques such as electron microscopy, they also offer an attractive means of investigating the effects of confinement on the crystallization of inorganic compounds.

Finally, controlled pore glasses (CPGs) are a silica material of a refractory nature that comprise a sponge-like network of interconnected pores, and are available with mean pore diameters from three to hundreds of nanometers. These therefore provide access to extremely small pore sizes. With high thermal and chemical stability, and the ability to characterize compounds within them using a wide range of analytical techniques, CPGs have been widely used for studies of confinement effects.

### 7.2.1. Depression of Melting Points

The influence of confinement on the phase behavior can be systematically studied in these porous media. The melting point depression experienced by a crystal forming in a cylindrical pores can be described by the Gibbs–Thomson equation (see also Section 4)

$$\Delta T_m = T_m - T_m(d) = \frac{4\gamma_{\text{solid-melt}}T_m}{d\Delta H^{\text{fus}}\rho_{\text{sol}}} \quad (27)$$

where this predicts a linear relationship between  $\Delta T_m$  and  $1/d$  (the channel diameter). However, this form of the equation fails to take into account the energy terms associated with the solid/substrate and melt/substrate (melt-sub) interfaces by assuming a contact angle of 180° between the solid and cylinder wall. It is therefore more appropriate to rewrite the equation as

$$\frac{\Delta T_m}{T_m} = \frac{4}{d\Delta H^{\text{fus}}\rho_{\text{sol}}} (\gamma_{\text{solid-sub}} - \gamma_{\text{melt-sub}}) \quad (28)$$

which predicts a different dependence of the melting point depression on the pore size for the different porous media.

This relationship was confirmed by studying the melting points of 2,2,3,3,4,4-hexafluoro-1,5-pentanediol (HFPD) and (*R*)-(+)-3-methyladipic acid (*R*-MAA) within polystyrene monoliths with parallel cylindrical channels and CPG beads using thermal analysis.<sup>[271]</sup> A large melting point depression was observed for both compounds, where this increased with decreasing channel diameter and thus increasing surface-area-to-volume ratio of the crystals. The melting point depression exhibited a linear dependence on  $1/d$ , despite the fact that  $\Delta H^{\text{fus}}$  also decreased linearly with increasing  $1/d$ . The linearity was attributed to the decrease in  $\Delta H^{\text{fus}}$  being compensated for by a decrease in  $\gamma_{\text{solid-melt}}$  with decreasing crystal size. The experimental data also revealed that the slope of  $\Delta T_m$  versus  $1/d$  is different for both HFPD and *R*-MAA within CPGs and the polystyrene monoliths. The melting point depression was greater in the polystyrene monoliths than in the CPGs, which derives from different interactions of the compounds with the two media.

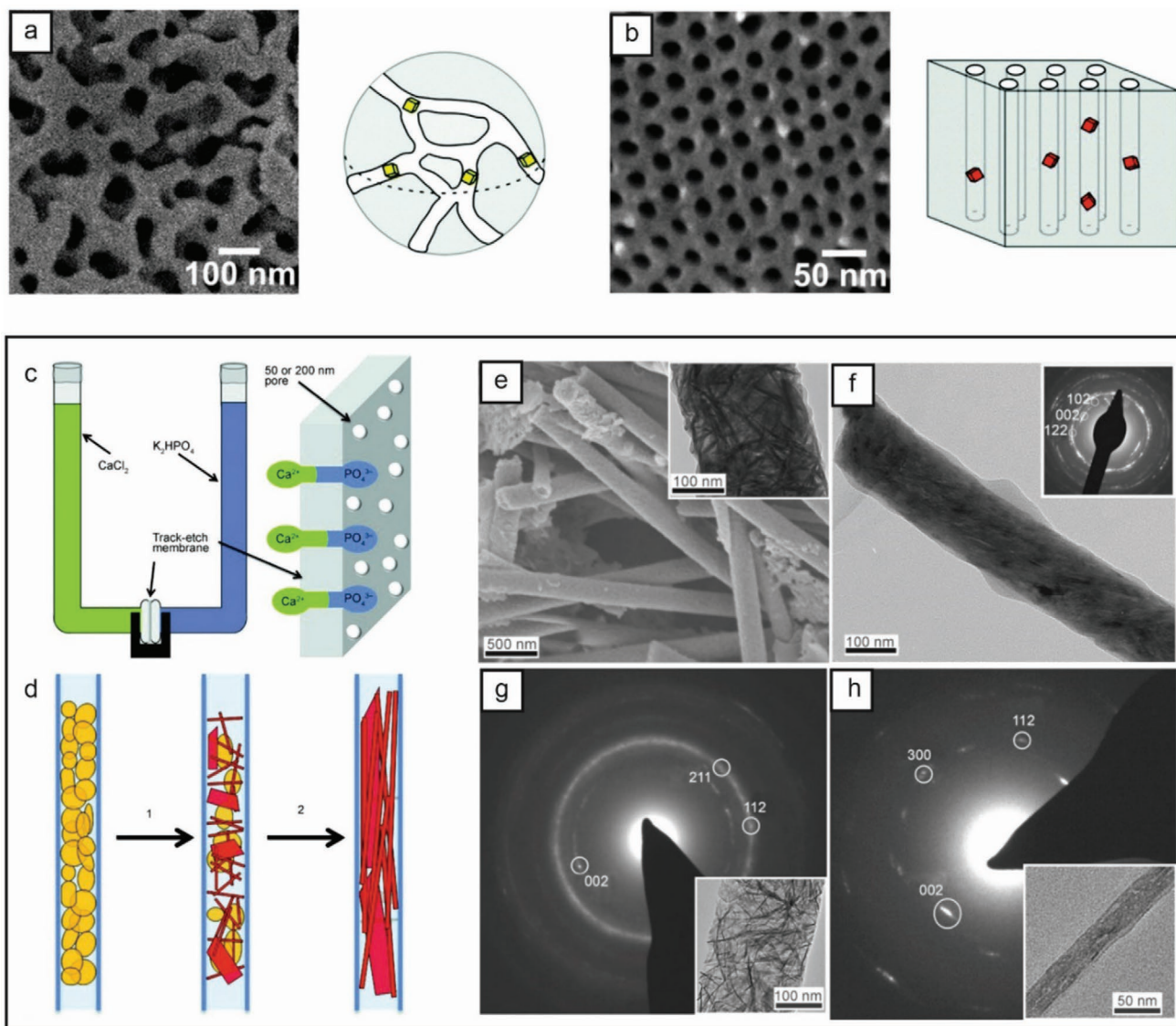


**Figure 19.** Top: a,b) SEM images and diagrams of a controlled pore glass with a pore size of 55 nm (a) and a platinum-coated p-PCHE monolith with an array of cylindrical pores of 30 nm in diameter (b). a,b) Reproduced with permission.<sup>[214]</sup> Copyright 2014, Royal Society of Chemistry. Bottom: c) Schematic of the crystallization of calcium phosphate in membrane pores in a double-diffusion configuration. d) Schematic of the crystallization sequence beginning with amorphous calcium phosphate particles (yellow) which then transform to hydroxyapatite (red). The hydroxyapatites are preferentially oriented with the [001] axis aligned with the long axis of the pore. e,f) SEM and TEM (inset) images of crystals after six days of growth in 200 nm pores (e) and a hydroxyapatite rod from a 50 nm pore after one day (f). g,h) SAED images with corresponding TEM images (inset) of a randomly oriented rod from a 300 nm pore (g) and a rod oriented parallel with the pore length of a 25 nm pore (h). c–h) Reproduced with permission.<sup>[273]</sup> Copyright 2013, Wiley-VCH.

### 7.2.2. Influence over Orientation

Crystallization within AAO- and TE-membranes frequently leads to a preferential orientation. This effect is characteristic of anisotropic crystals, where these achieve an orientation such that their fast-growing crystallographic direction lies parallel to the long axis of the nanopore. This can be attributed to competitive growth effects, where unimpeded growth is only possible parallel to the pore axis. Those crystals oriented with their direction of rapid growth coincident with the pore axis therefore grow at the expense of crystals in other orientations, such that

the faces with higher surface energy span the narrowest dimension of the pore.<sup>[272–274]</sup> When pores are comparable in diameter to the critical nucleus size, growth may be constrained such that crystals cannot exceed a critical volume, which further promotes growth of the highly oriented crystals.<sup>[214]</sup>

Many examples of this behavior are seen across the literature.  $\beta$ -Glycine crystals formed within AAO membranes with 20–200 nm pores<sup>[275,276]</sup> and porous polystyrene–poly(dimethyl acrylamide) (PS-PDMA) monoliths with 10 and 20 nm pores<sup>[272,277]</sup> were oriented such that their fast-growing [010] axes were parallel to the pore axis. While the metastable  $\beta$ -glycine

crystals showed long term stability in the pores under ambient conditions, incubation at relative humidities of 90% induced a transformation to  $\alpha$ -glycine within 24 h.<sup>[276]</sup> These crystals were now oriented with the [100] axis parallel to the pore axis, corresponding to a 90° rotation of the glycine molecules with respect to the original  $\beta$ -glycine crystals. Notably, addition of chiral auxiliaries to the growth solution that retard growth of  $\beta$ -glycine along the [010] and  $[0\bar{1}0]$  axes changed the orientation of the crystals such that the  $[10\bar{5}]$  direction (which lies perpendicular to the  $(10\bar{2})$  plane) was oriented parallel to the pore axis.<sup>[272]</sup> This represents a rotation of 90°, where the {010} planes were now parallel to the pore axis.

A range of other organic compounds have also been shown to exhibit orientation in cylindrical pores. Crystals of ROY were formed within 30 nm pores of poly(cyclohexylethylene) (PCHE) monoliths containing hexagonal arrays of cylindrical pores, and the R crystals were oriented such that the (111) plane is aligned with the pore axis.<sup>[278]</sup> Crystals of HFPD formed within porous polystyrene monoliths showed a preferential orientation such that the (012) planes were approximately parallel to the long axis of the pores.<sup>[271]</sup> This plane features HFPD molecules held together by in-plane hydrogen bonds, such that only the nonpolar CF<sub>2</sub> groups protrude from its surface. This orientation therefore also minimizes the contact of the polar hydroxyl groups with the polystyrene pore walls. Crystallization of an organic semiconductor (triisopropylsilylethynyl pentacene) within 60–200 nm AAO membrane pores resulted in preferential orientation such that the fast-growing direction (the  $\pi$ -stack direction) was aligned with the long axes of the pores,<sup>[279]</sup> and oriented acetaminophen (paracetamol) formed within AAO membrane pores where the (0k0) faces of the form II crystals, and the (hk0) faces of the form III crystals were oriented normal to the pore axes.<sup>[280]</sup>

A detailed study was also carried out of the orientations of crystals of  $\alpha,\omega$ -alkanedicarboxylic acids (HO<sub>2</sub>C(CH<sub>2</sub>)<sub>*n*</sub>-CO<sub>2</sub>H, *n* = 3–13, odd) in the cylindrical pores of PCHE monoliths and revealed a dependence of the orientation on the chain length.<sup>[281]</sup> Crystals of malonic acid (*n* = 3) in 14, 30, and 40 nm pores existed in two orientations, both of which lay parallel to the direction of the hydrogen-bonded chains. Crystals of glutaric acid (*n* = 5) also possessed orientations where the hydrogen-bonded chains were coincident with the long axes of the 30 and 40 nm pores, but the 14 nm pores supported an entirely different orientation in which the average direction of the hydrogen-bonded chains lay perpendicular to the pore axis. Pimelic acid (*n* = 7) crystals were similarly oriented with their hydrogen-bonded chains parallel to the pore direction, but crystals of *n* = 9, 11, or 13 alkane dicarboxylic acids adopted orientations in which the hydrogen-bonded chains progressively tilted away from the pore direction as the alkane length was increased. This was attributed to changes in the fast-growing crystal direction according to the alkane structure, where crystals oriented such that their rapidly growing axis can grow unrestricted at the expense of crystals in other orientations.<sup>[213]</sup>

Inorganic compounds also exhibit preferential orientation. Single crystals of Rochelle salt (NaKC<sub>4</sub>H<sub>4</sub>O<sub>6</sub>·4H<sub>2</sub>O) and KNO<sub>3</sub> preferentially oriented with their respective (100) and  $\langle 010 \rangle$  axes parallel to the long axes of 35 nm AAO membrane pores, where the KNO<sub>3</sub> crystallized with the aragonite form.<sup>[282]</sup> Single crystal Bi<sub>2</sub>S<sub>3</sub> nanowires formed within 20–80 nm pores using metal–organic

chemical vapor deposition (MOCVD)<sup>[283]</sup> were oriented with the [002] direction parallel to the long axis of the pore,<sup>[283]</sup> while single crystal nanorods of the superconductor YBa<sub>2</sub>Cu<sub>3</sub>O<sub>7- $\delta$</sub>  (YBCO) were preferentially oriented with the [100] axis parallel to the pore axis.<sup>[284]</sup> CdS nanorods formed via an electrochemical method were oriented with their *c*-axes parallel to the long axes of the pores.<sup>[285]</sup> Silicon wafers can also be etched to create arrays of cylindrical channels, and crystallization of *n*-hexanes within 10 nm pores resulted in crystals with the triclinic structure characteristic of the bulk phase aligned with their fast-growing  $\langle 001 \rangle$  axis parallel to the long axis of the pore.<sup>[286]</sup>

A strong pore size dependence has been seen in the orientation of calcium phosphate (CaP) within the pores of TE membranes (Figure 19c–h).<sup>[273,287]</sup> CaP was precipitated within 25–300 nm pores under physiological conditions, where the progression from amorphous CaP to octacalcium phosphate (OCP) or hydroxyapatite (HAP) was retarded in the membrane pores. The intra-pore crystals exhibited rod-like morphologies and were either single crystal OCP or polycrystalline HAP. They were also oriented such that the fast-growing [001] axis of HAP was parallel to the long axis of the pore with angular spreads of  $\pm 15^\circ$ – $25^\circ$  for the 200 nm and  $\pm 15^\circ$ – $20^\circ$  for the 50 nm rods. Exploration of even smaller pores of 20 nm was made possible using AAO membranes, where a high degree of orientation was achieved with an angular spread of  $\pm 5^\circ$ – $12^\circ$ .

These experiments are also relevant to CaP precipitation in biological nanocomposites, such as bone and dentine. Both bone<sup>[288,289]</sup> and collagen fibrils mineralized in vitro<sup>[39,290,291]</sup> exhibit preferential orientation of the *c*-axes of the HAP crystallites with the long axis of the collagen fibrils with an angular spread of  $\approx \pm 15^\circ$ . The mechanism by which collagen directs the orientation of HAP has been much discussed and has been attributed to factors such as a structural match between the HAP nanocrystals and the collagen. The possibility that the confines of the gap region in collagen directs orientation has also been suggested. These simple experiments with TE membranes add support to the hypothesis that confinement effects play a role in determining the orientation of HAP platelets in collagen.

Insight into the mechanism by which crystals achieve a preferential orientation within nanopores was obtained from a study of the growth of Ni(OH)<sub>2</sub> within AAO membranes (Figure 20).<sup>[292]</sup> There, membranes were coated with a thin layer of carbon using CVD of propylene and were then impregnated with an ethanolic solution of Ni(NO<sub>3</sub>)<sub>2</sub>·6H<sub>2</sub>O and dried. Following hydrothermal treatment in 10 M NaOH at 150 °C dissolution of the AAO membrane released carbon nanotubes containing the nickel compound. With their electron transparent character, this system enabled the crystallization pathway to be evaluated.

Detailed examination of crystallization within 100 nm pores revealed that after 1 h reaction time the pores contained <50 nm hexagonal crystals of  $\beta$ -Ni(OH)<sub>2</sub>, together with some small, thin crystals (Figure 20e–h). The hexagonal crystals have exactly the same structure, and comparable shapes and sizes to Ni(OH)<sub>2</sub> formed using a hydrothermal route in bulk solution. Larger hexagonal crystals and some small nanorods were observed after 6 h, and after 24 h most of the hexagonal platelets had grown to reach the walls of the nanotube. These were oriented such that the (001) planes that comprise the large faces of the hexagon were parallel to the pore axis. The nanorods then

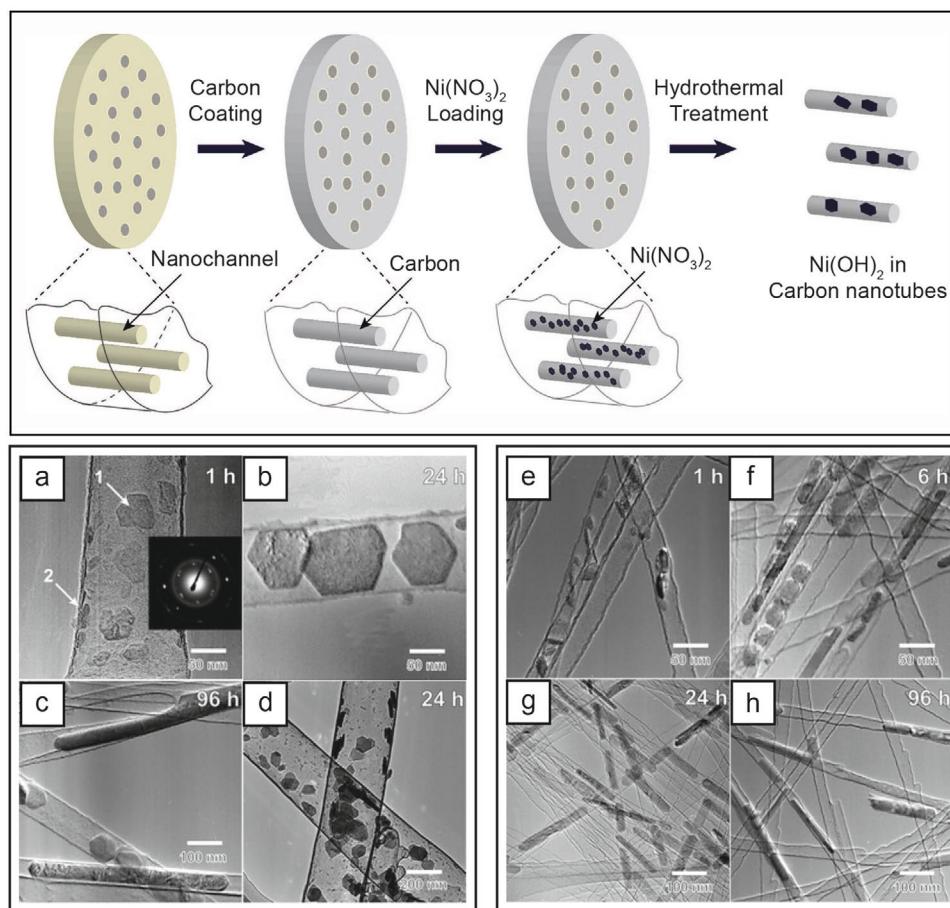


**Figure 20.** Schematic of the hydrothermal synthesis of  $\text{Ni}(\text{OH})_2$  crystals inside carbon-coated 1D nanochannels of anodic aluminum oxide (AAO). a–d) TEM images and an SAED pattern of  $\text{Ni}(\text{OH})_2$  crystals synthesized for different periods in the nanochannels with diameters of 100 nm (a–c) and 300 nm (d). The inset in (a) is an SAED pattern of the crystal labeled 1. e–h) High-magnification TEM images of  $\text{Ni}(\text{OH})_2$  crystals synthesized for different hydrothermal periods in 25 nm diameter nanochannels: a) 1 h; b) 24 h; c) 96 h; d) 24 h; e) 1 h; f) 6 h; g) 24 h; h) 96 h. Schematic (top): Adapted with permission.<sup>[292]</sup> Copyright 2007, Royal Society of Chemistry. a–h) Reproduced with permission.<sup>[292]</sup> Copyright 2007, Royal Society of Chemistry.

continued to increase in number and size at the expense of the hexagonal crystals with longer reaction times. Comparison with different-sized pores showed that short nanorods were present after just 6 h in 25 nm pores, while individual hexagonal platelets alone were present in the 300 nm pores after 24 h. Transformation into single crystal nanorods was therefore attributed to an Ostwald ripening mechanism, where larger crystals grow at the expense of smaller ones. The small pores thus create a unique environment that can dictate the morphology, orientation and number of crystals within the nanopore.

### 7.2.3. Influence over Polymorph

The nanoscale pores within AAO- and TE-membranes and CPGs can stabilize metastable polymorphs of many crystals, where this has been attributed to a range of effects. Looking first at the behavior of organic compounds in confinement, metastable  $\beta$ -glycine exclusively formed within 20–200 nm AAO nanopores,<sup>[276]</sup> CPGs with pore sizes of 75, 24, and 55 nm<sup>[277]</sup> and porous polystyrene–poly(dimethyl acrylamide) (PS-PDMA) monoliths with 10 and 20 nm pores<sup>[277]</sup> when the

porous matrices were immersed in a glycine solution and then vacuum dried. This compares with  $\alpha$ -glycine in bulk solution.  $\beta$ -glycine was stable for over a year within the 75, 24 nm CPGs, and transformed to the  $\alpha$ -phase within 60 days in the 55 nm CPG. All crystals within the CPGs also exhibited a melting point depression that increased in magnitude with decreasing pore size.

An alternative study identified a mixture of glycine polymorphs within AAO membranes with 55 nm pores, where crystallization was induced by immersing the membrane in unsaturated solutions of glycine and then incubating for 20 h at 24 °C.<sup>[275]</sup> Concentrations of 2.3 g glycine/10 g  $\text{H}_2\text{O}$  yielded the  $\alpha$ -polymorph only, 2.0 g/10 g a mixture of the  $\alpha$ - and  $\beta$ -polymorphs, and 1.8 g/10 g a higher ratio of the  $\beta$ - to the  $\alpha$ -polymorph. The increase in  $\beta$ -polymorph with decreasing concentration was attributed to a lower diffusion rate of molecules to the nucleation site, which limited the formation of the more stable  $\alpha$ -phase.

Looking then at the much-studied model compound ROY, crystals were formed within 30 nm pores by evaporating a pyridine solution of ROY in contact with a PCHE monolith.<sup>[278]</sup> Both the  $\gamma$ -polymorph and amorphous ROY were identified, as

compared with the Y polymorph on the surfaces of nonporous PCHE. A further heating/cooling cycle was also performed after removing any bulk crystals from the porous monolith surface, and amorphous ROY and the R polymorph were generated. Notably, crystallization of ROY was suppressed in 20 nm pores, such that amorphous ROY formed. This was attributed to the pores being too small to accommodate critical nuclei of any of the crystalline polymorphs. By comparison, polymorphs R and ON formed on the monolith surface.

Acetaminophen (paracetamol) has three known polymorphs, where Type-I is the most stable, Type-II metastable, and Type-III unstable under bulk conditions. Selectivity over polymorph has been obtained by crystallizing within AAO membranes and CPGs with different sized pores.<sup>[280,293–295]</sup> Acetaminophen was crystallized within CPG membranes by immersing them in molten acetaminophen and then cooling.<sup>[293–295]</sup> The crystalline layer on the surface of the membranes was then removed and the sample was subjected to differential scanning calorimetry (DSC) scans. Cooling in the presence of a reservoir on the membrane surface led to the formation of Type-I acetaminophen in CPGs with pore sizes between 22 and 103 nm. Confinement within the nanopores resulted in a melting point depression, where this was very small for the 103 nm pores and increased in magnitude with decreasing pore size.

Samples in which acetaminophen was only located within the pores were also quenched from 180 °C, generating an amorphous solid. Isothermal heating yielded the type-III polymorph at 80 °C and the type-II polymorph at 100 °C. Similar studies with AAO membranes of pore sizes of 25–400 nm showed that type-II and III are formed in pores >100 nm.<sup>[293]</sup> That all three polymorphs can form within these environments demonstrates that the stabilization of metastable phases cannot be ascribed to the exclusion of phases whose critical nuclei are too large.<sup>[293]</sup> Examination of CPGs with pore sizes of only 4.6 nm showed that crystallization was completely suppressed in this environment.<sup>[294]</sup> Estimation of the critical nucleus size as ≈4 nm suggests that the pore diameter may simply be too small to allow the formation of a crystalline nucleus. The low mobility of molecules at the reduced crystallization temperature may also lead to slow kinetics.

A strong size effect was seen for the crystallization of *o*-terphenyl and benzyl alcohol within CPGs with pore sizes of 4–73 nm,<sup>[296]</sup> where *o*-terphenyl only crystallized in 73 nm pores while the crystallization of benzyl alcohol depended on the pore size and reaction conditions. Benzyl alcohol failed to crystallize in 4 nm pores, and crystallization only occurred in 8.5 nm pores when they were overfilled, potentially due to the formation of nuclei outside the pores. Failure to crystallize in the smallest pores may be due to the inability of a critical nucleus—which is estimated to have a size of around 4 nm—to form in the highly constrained pore. The failure of *o*-terphenyl to crystallize may arise from its recognized slow kinetics.

Polymorph selectivity of anthranilic acid (AA) in CPGs was also attributed to a size-restriction of a critical nucleus. AA crystallizes in three polymorphs, where form II is formed on cooling supersaturated solutions or by rapid evaporation at room temperature. Form III can be generated from the melt, and mixtures of II and III can be obtained by sublimation. CPG beads were infiltrated with molten AA and then slowly

cooled.<sup>[278]</sup> Form III AA formed on the surfaces of the beads and within beads with 55 nm pores, while Form II was the dominant polymorph in 23 nm pores and the sole product in 7.5 nm CPGs. Polymorph selectivity was attributed to the larger critical nucleus of the type-III polymorph, which precluded its formation in the 7.5 nm pores.

In our final example of studies of organic compounds, the influence of the structure of small organic molecules on their crystallization within porous PCHE monoliths and CPG beads was investigated for a series of  $\alpha,\omega$ -dicarboxylic acids and coumarin (1,2-benzopyrone) (Figure 21).<sup>[297]</sup> Glutaric acid (HOOC(CH<sub>2</sub>)<sub>3</sub>COOH) was precipitated within these porous media by infiltrating them with a methanolic solution, and then evaporating the solvent. Both the  $\alpha$  and  $\beta$  polymorphs formed in PCHE monoliths with 14 nm pores, while only  $\alpha$ -glutaric acid in 30 and 40 nm pores;  $\beta$ -glutaric acid is stable in bulk. Subsequent melting and recrystallization of the intrapore crystals then yielded the  $\alpha$ -polymorph alone in all three pore sizes. A mixture of the  $\alpha$  and  $\beta$  polymorphs formed in 7.5, 24, and 55 nm pores in the CPGs. The CPGs were also infiltrated with molten glutaric acid, in which case the  $\alpha$ -polymorph exclusively formed on cooling. The  $\beta$  to  $\alpha$  transition was also suppressed in these confined environments. This behavior suggests that  $\alpha$ -glutaric acid is thermodynamically favored in nanoscale confinement, and that the  $\beta$ -polymorph is a kinetic product when crystallized by evaporation of methanol solutions.

Pimelic acid (HOOC(CH<sub>2</sub>)<sub>5</sub>COOH) has three polymorphs, of which the  $\alpha$  and  $\beta$  polymorphs precipitated within CPGs filled from a methanolic solution, while the  $\alpha$ -polymorph was the sole product in the monolith under these conditions. Different results were obtained for samples produced by cooling of a melt. A new polymorph (termed  $\delta$ ) formed within 75 nm CPGs, while the  $\alpha$ - or  $\delta$ -polymorphs formed within 23 nm pores and  $\alpha$  only in 55 nm pores. Conversion to the  $\delta$ -polymorph within the 75 and 23 nm pores occurred within 1 month. The  $\delta$ -polymorph was also the sole form within the 14 and 30 nm monolith pores, while a mixture of the  $\delta$  and  $\alpha$  polymorphs was generated in the 40 nm pores. The  $\delta$ -pimelic acid crystals within 30 nm

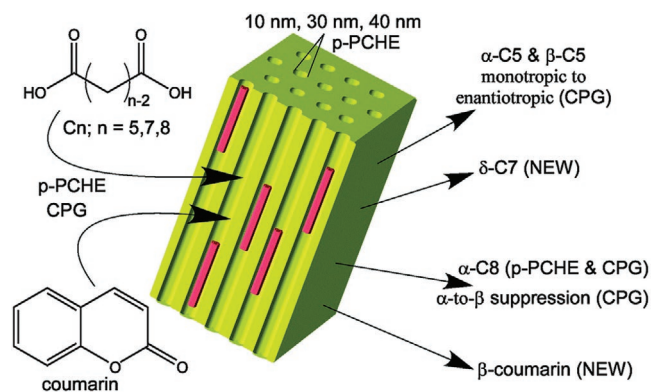


**Figure 21.** Schematic summarizing the results of the crystallization of  $\alpha,\omega$ -alkanedicarboxylic acids, including pimelic acid (C7,  $n = 7$ ), glutaric acid (C5,  $n = 5$ ), and suberic acid (C8,  $n = 8$ ), and coumarin in the pores of p-PCHE and CPG. This resulted in the identification of three, previously unreported polymorphs. Reproduced with permission.<sup>[214]</sup> Copyright 2014, Royal Society of Chemistry.

pores underwent partial conversion to the  $\alpha$ -polymorph within one month, while it was stable for over a year in 14 nm pores.

Only one polymorph is recognized for suberic acid ( $\text{HOOC}(\text{CH}_2)_6\text{COOH}$ ), but bulk experiments have suggested the existence of a metastable  $\beta$ -phase. Cooling of a melt of suberic acid within the CPGs yielded the  $\beta$ -polymorph, which remained stable at room temperature. A new form of coumarin—termed the  $\beta$ -polymorph—precipitated within 14 nm pores in the monoliths, while a mixture of  $\alpha$ - and  $\beta$ -coumarin crystallized in 30 and 40 nm pores.  $\alpha$ -coumarin exclusively formed within 55 nm CPGs, while the  $\beta$ -polymorph was also present in the smaller pores. The data was consistent with the  $\alpha$ -coumarin having greater stability at crystal sizes of 55 nm and above, and the  $\beta$ -polymorph for crystal sizes of 23 nm or below.

Polymorph selectivity has also been observed for inorganic compounds in confinement. Pressure injection was used to fill the AAO membrane pores with liquid Bi, which crystallized under slow cooling.<sup>[298]</sup> While the majority of the rods formed had the same structure as the bulk crystal, some pores contained a metastable, high-pressure phase. As Bi expands on transformation from liquid to solid, it was suggested that the membrane pores could impose an external stress that stabilizes the high pressure crystal structure.

The polymorph of the all-inorganic cesium lead halide ( $\text{CsPbI}_3$ ) perovskite can also be selected using confinement effects.<sup>[299]</sup> The  $\alpha$ -phase has attractive semiconductor properties, but typically converts to the nonphotoactive  $\delta$ -phase at temperatures below 300 °C. The  $\delta$ -phase was the only polymorph detected within 112 nm pores in AAO membranes, while a mixture of the  $\alpha$ - and  $\delta$ -phases was produced in 69 nm pores. The  $\alpha$ -phase alone was found in 30 and 41 nm pores. The perovskite methylammonium lead iodide ( $\text{MAPbI}_3$ ) has also been deposited within AAO membranes with pores of diameter 20–200 nm.<sup>[300]</sup> These environments supported the formation of a metastable crystalline phase containing solvent molecules, where the crystals were oriented such that alternating sheets of  $\text{PbI}_2$  and solvent molecules lie parallel to the long axis of the pores. Annealing at 130 °C converts this phase to randomly oriented  $\text{MAPbI}_3$  crystals. The confines of the membrane pores also retard the degradation of  $\text{MAPbI}_3$  to  $\text{PbI}_2$ , where they remained stable for over two weeks.

Significant effects on polymorph were observed for potassium ferrocyanide,  $\text{K}_4\text{Fe}(\text{CN})_6$  (KFC) on crystallization within CPGs with very small pore sizes. KFC crystallizes at room temperature as an anhydrous form (KFC) and as potassium ferrocyanide trihydrate (KFCT), which has a metastable tetragonal form and a thermodynamically stable monoclinic polymorph. Anhydrous KFC, which was never observed on precipitation in bulk aqueous solution, was the first phase to crystallize within the CPGs and was present for at least 1 day in 8, 48, and 362 nm pores.<sup>[301]</sup> Slow transformation to the metastable tetragonal polymorph of KFCT then occurred, where this polymorph was stable for a month in 8 nm pores. Finally, this converted to the thermodynamically stable monoclinic polymorph. Notably, this phase was always found after a few minutes in bulk solution.

Extensive studies have focused on the crystallization of calcium carbonate within the pores of TE membranes,<sup>[35,36,38,302,303]</sup> in order to gain insight into the mechanisms by which organisms gain control over biomineralization processes.

Precipitation of calcium carbonate at low temperatures invariably generated ACC that was stable for up to 30 min and that subsequently transformed to calcite.<sup>[35,36]</sup> However, the yield of crystals was low in small pores ( $\approx 50$  nm) using this strategy.<sup>[38]</sup> Infiltration into small pores was vastly enhanced by addition of low concentrations of the polyelectrolytes poly(aspartic acid) (PAsp) or poly(acrylic acid) (PAA) where these generate a so-called polymer-induced liquid precursor (PILP) phase.<sup>[304]</sup> The mineral precursor phase subsequently crystallized within the membrane pores to give high aspect ratio single crystals (Figure 22a,b).<sup>[38]</sup>

TE membranes were also used to investigate the potential role of confinement in calcite/aragonite polymorphism.<sup>[305]</sup> While aragonite is only slightly less thermodynamically stable than calcite under ambient conditions, it typically only forms as a minor product in additive-free solutions at room temperature. However, aragonite is an abundant biomineral, and certain organisms can selectively generate calcite and aragonite. The mechanism by which they achieve such control has been the subject of intense interest, where it is widely believed that organisms achieve polymorph selectivity using organic macromolecules. Experiments were conducted using uncoated polycarbonate TE membranes and low concentrations of magnesium and sulfate ions—both of which promote aragonite formation and which are present in high concentrations in the oceans.

Experiments were initially performed in bulk solution to identify sulfate and magnesium concentrations that promote low levels of aragonite. These were then applied to the TE membrane system with pore diameters of 1200, 800, 200, 50, and 25 nm. The crystals in the 1200 nm pores and on the surfaces of all of the membranes were almost entirely calcite. The proportion of aragonite then increased with a decreasing pore diameter to 19% aragonite in 800 nm pores and 69% in 200 nm pores, and aragonite was the sole polymorph in 50 and 25 nm pores (Figure 22c). Experiments were also conducted in the absence of magnesium and sulfate. Very little aragonite formed in the 1200 and 800 nm pores and just 8% in the 200 nm pores. However, 47% of the crystals in the 50 nm pores were aragonite and aragonite single crystals formed in the absence of any additives in the 25 nm pores.

Growth within the cylindrical pores also influenced the orientation and single crystal/polycrystalline characteristics of the rods. Aragonite crystals grown in the presence of magnesium and sulfate in the 200 nm pores were polycrystalline and exhibited no preferential orientation. Those in the 50 nm pores were virtually single crystals, and the 25 nm rods indistinguishable from single crystals (Figure 22c,d). These aragonite crystals were preferentially oriented with the  $c$ -axis (the direction of fast growth) parallel to the pore axis, such that  $\approx 50\%$  and  $100\%$  of rods in the 50 and 25 nm pores were oriented in this way. 90% of the aragonite crystals formed in the 25 nm pores under additive-free conditions were also oriented with their  $c$ -axes parallel to the pore axis.

No definitive answer can be given for the selection of aragonite in these small volumes. However, a graph of the aragonite percentage versus the inverse of the pore diameter reveals a linear relationship between these quantities. This is expected if the number of aragonite nucleation sites is proportional to the surface area ( $d^2$ ), while the amount of  $\text{CaCO}_3$  is proportional to volume ( $d^3$ ) under a constant rate of crystal growth. The



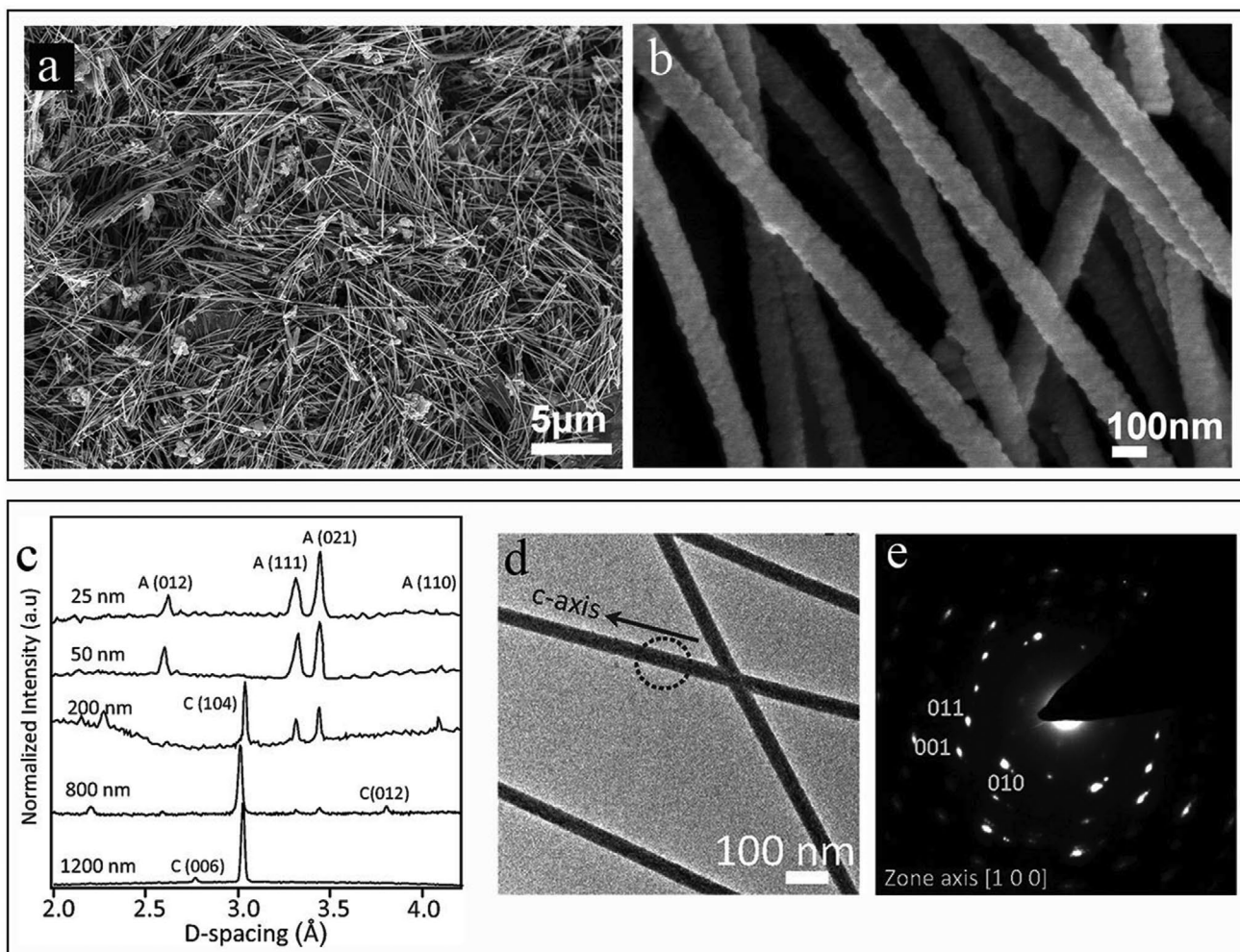


**Figure 22.** a,b) SEM images of calcite crystals precipitated in 100 nm pores of track-etched membranes in the presence of poly(aspartic acid). a,b) Reproduced with permission.<sup>[38]</sup> Copyright 2011, Wiley-VCH. c) XRD spectra showing the increase in the proportion of aragonite formed as the pore size reduces for crystals precipitated under conditions  $[Ca^{2+}] = [CO_3^{2-}] = 1.5 \times 10^{-3}$  M and  $[Ca^{2+}]:[Mg^{2+}]:[SO_4^{2-}] = 1:2:1$ . A, aragonite; C, calcite. d,e) TEM image and corresponding electron diffraction pattern of a single aragonite rod precipitated in 50 nm membrane pores under the solution conditions described in (c). c–e) Reproduced with permission.<sup>[305]</sup> Copyright 2018, National Academy of Sciences, USA.

proportion of aragonite therefore increases with the degree of confinement as the surface increases in importance relative to the bulk. This may be related to a surface-induced alteration of the local ionic environment in the small pores, where the distribution of ions adjacent to a charged membrane surface can differ significantly in a membrane pore compared with a planar surface, particularly for divalent ions.<sup>[306,307]</sup>

#### 7.2.4. Influence of Surface Chemistry

A number of studies have shown that the surface chemistry of the pore can also influence crystallization. Bi was crystallized within AAO membranes that had either been anodized in  $H_2C_2O_4$  and etched using  $H_3PO_4$  (termed C-templates) or anodized or etched using  $H_2SO_4$  (S-templates). These had pore sizes of 20–120 and 9–30 nm, respectively.<sup>[298]</sup> Oriented single crystal nanorods formed within the pores, where 90% of those

in the C-membranes were directed with the (202) plane parallel to the plane of the membrane. Two orientations were observed in the S-membranes such that the (012) or (202) plane was parallel to the plane of the membrane.

The influence of the membrane surface chemistry was investigated for the crystallization of hentetracontate (termed C41) within AAO membranes using X-ray diffraction and non-isothermal crystallization, where the samples were incubated at 120 °C for 5 min, and then cooled to 30 °C at different cooling rates.<sup>[308]</sup> C41 crystallized at two temperature ranges below the bulk value within unmodified membranes. In membranes modified with polydimethylsiloxane, in contrast, crystallization was suppressed at the upper temperature range, and enhanced at the lower temperature range. The orientation of the C41 crystals was also affected by the surface of the membrane, such that the C41 crystals were oriented with the *a*-axis parallel to the pore axis within the unmodified membranes, while two orientations—one identical to the unmodified membrane and the

other with the (110) plane parallel, and the *c*-axis perpendicular to the pore axis—were obtained in the modified membranes.

The surface chemistry can also influence the polymorph produced, as seen in the calcium carbonate system. CaCO<sub>3</sub> was precipitated within AAO membranes with 200 nm pores whose surfaces were modified with Gly-His and Gly-Ser peptides,<sup>[309]</sup> and small, polycrystalline aragonite particles formed within the pores as compared with calcite under identical bulk solution conditions. However, it cannot be ruled out that dissolution of the membranes under the experimental conditions used contributed to the polymorph observed.

Variation in CaCO<sub>3</sub> polymorph was also observed in TE membranes depending on the source of the membranes.<sup>[302]</sup> Comparison of crystal growth from [Ca<sup>2+</sup>] = 10 × 10<sup>-3</sup> M solutions in membranes with 200 nm pores from two suppliers showed that Millipore membranes supported the formation of a high yield of intrapore crystals. These crystals were almost exclusively single crystals of vaterite that remained stable for >4 days even when the membrane remained immersed in the reaction solution. This compares with the calcite crystals formed on the membrane surfaces. In contrast, a low yield of intra-pore crystals was obtained in membranes supplied by Sterlitech. These were ≈1/1 calcite/vaterite as compared with calcite on the membrane surface. That the two membrane types behave differently suggests that they must create different environments within the pores. However, extensive characterization of the pore size distributions, the surface chemistry, and topography revealed only minor differences in the surface roughness and no compositional variations. Very subtle differences in the microenvironments within the pores must drive the observed effects on CaCO<sub>3</sub> precipitation, where these could comprise differences in the density or conformation of the chemical species lining the membrane pores. It is also interesting that single crystals of vaterite form within the membrane pores as compared with the polycrystalline particles that invariably form in bulk solution. This again demonstrates that the membrane pores must limit vaterite nucleation such that nuclei can grow with limited competition to give a single crystal product. A similar mechanism was proposed for the growth of single crystals of Pb in carbon nanotubes.<sup>[310]</sup>

## 8. Mesoporous Solids

Mesoporous silica has been extensively explored as a carrier for drug delivery, where the small pores can readily stabilize many drugs in an amorphous form, and thus enhance solubility.<sup>[311–315]</sup> The majority of work has focused on MCM-41 and SBA-15 where these have pore sizes of ≈4 and ≈8 nm respectively. NMR has been used to investigate the environment of small molecules<sup>[316–318]</sup> and larger drug molecules<sup>[319]</sup> within mesoporous silica. Crystallization of flufenamic acid (FFA) was investigated in the mesoporous silicas MCM-41, SBA-15, and MCF where these have pore sizes of 3.2, 7.1, and 29 nm, respectively. No crystallinity was observed in the MCM-41 or SBA-15 after filling with the melt. Crystallization did occur in the larger pores of MCF, however. <sup>19</sup>F NMR of FFA-MCF revealed the presence of two molecular environments corresponding to crystalline material and a liquid-like layer at the surfaces of the pores. Analysis

of FFA-MCM and FFA-SBA also revealed two environments corresponding to a disordered amorphous phase and a liquid-like surface phase, where the liquid-like surface layer can be attributed to weak interactions between the hydrophobic FFA guest and the hydrophilic silica surface. NMR was additionally used to follow the crystallization of FFA-MCF, and revealed that the population of FFA molecules associated with the liquid-like layer remains unchanged over time.

## 9. Crystallization in Wedge Geometries

A wedge-shaped geometry provides the opportunity to study crystallization between surfaces that range continuously from angstroms to the macroscopic level in a single experiment. Importantly, it is also possible to create wedges that are sharp on the nanoscale, and even at the atomic-level. Effective ways of creating a well-defined wedge with a sharp apex include placing a sphere on a planar substrate or by crossing two half cylinders. Both create an annular wedge, where the separation of the surfaces as a function of the distance from the contact point is defined by the radius of the sphere/cylinder. Natural cracks that occur in brittle materials can provide an opportunity for studying crystallization in atomically sharp environments.

### 9.1. Surface Forces Apparatus (SFA)

The SFA is used to measure the force between two surfaces in liquid and in vapor.<sup>[320]</sup> This is achieved using two curved, atomically flat surfaces (usually mica), which are mounted in a crossed-cylinder configuration. The surface separation *h* between identical crossed cylinders with radii of curvature *R* is equal to that between a sphere of radius *R* and a flat surface, and is related to the radial distance *x* from the contact point by

$$h = R - \sqrt{R^2 - x^2} \approx x^2/2R \quad (29)$$

Mounting one of these surfaces on a mechanical spring and recording its deflection allows the force between the surfaces to be determined as a function of the surface separation. The separation, in turn, is determined using multiple beam interferometry. Replacement of the spring with a more rigid support enables this apparatus to be used to study confinement effects on phase behavior.<sup>[43]</sup> Further, information about the refractive index, and thus the phase of the material between the surfaces can also be obtained using interferometry.

Freezing/melting phenomena have been studied in the SFA, as reviewed by Christenson.<sup>[43]</sup> The process of capillary condensation from unsaturated vapor has been widely investigated, and the liquid condensate sometimes crystallizes below the melting point (*T<sub>m</sub>*) when the surfaces are separated. Direct deposition of solid from vapor has also been observed at temperatures well below *T<sub>m</sub>*. Significant differences in behavior are observed for different compounds.

An SFA was used to study the behavior of an aqueous solution of the chloride salt of the low solubility rod-shaped dye molecule bis-(dimethylamino)heptamethine (BDH<sup>+</sup>Cl<sup>-</sup>) in the confines between two mica surfaces.<sup>[321]</sup> The cationic

dye molecules adsorb to the mica surfaces, where they can interact and ultimately form aggregates when present at sufficient concentrations. Multiple approach/separation cycles therefore lead to the formation of a crystal, where cations accumulate between surfaces separated by a molecularly thin gap, and then add to the aggregates as the surface separation is increased.

The interaction between two polycrystalline calcite surfaces and their surface reactivity in confinement has also been studied using an SFA,<sup>[322,323]</sup> and similar systems have been considered using modeling approaches.<sup>[324,325]</sup> Experiments were conducted using calcite surfaces glued to two crossed cylinder disks, where the calcite thin films were deposited on mica using atomic layer deposition. Solutions were saturated with  $\text{CaCO}_3$ , and the influence of the additional electrolytes NaCl,  $\text{CaCl}_2$ , and  $\text{MgCl}_2$  was also explored.<sup>[322]</sup> Force curves were measured as a function of the surface separation, and repulsive forces were recorded in all cases. Despite the solution being saturated with respect to calcite, the calcite surfaces underwent minor dissolution, where this was attributed to the roughness of the films. Dissolution was then followed by the onset of a precipitation front, which propagated inward toward the contact zone. Precipitation was attributed to a build-up of supersaturation and was associated with a significant increase in the repulsive forces. The precipitates were consistent with ACC and moved freely in the solution, suggesting that they did not nucleate on the calcite surfaces. Subsequent approach/separation cycles eventually led to the formation of  $\approx 5 \mu\text{m}$  particles that appeared to be crystalline. Added NaCl and  $\text{CaCl}_2$  induced

faster formation of the precipitation front, which could be attributed to more rapid dissolution of the calcite or decreased solubility of the calcium carbonate, while  $\text{Mg}^{2+}$  ions significantly delayed nucleation.

## 9.2. Crossed Cylinders Apparatus

A crossed cylinder apparatus was used to investigate the effects of confinement on the precipitation of calcium carbonate,<sup>[326,327]</sup> calcium phosphate,<sup>[328]</sup> calcium oxalate,<sup>[329]</sup> and calcium sulfate.<sup>[330]</sup> Cylinders with diameters of 25 mm offer a surface separation that varies from zero at the contact point to 2–3 mm at the air/solution interface of the droplet (around 7–8 mm from the contact point). A droplet of supersaturated solution is placed between the cylinders, providing a large reservoir of ions. The crystals precipitated on the cylinders can be characterized after separating the cylinders, and their position with respect to the contact point yields the surface separation at which they formed (Figure 23a,b).

Looking first at calcium carbonate,<sup>[326]</sup> experiments were conducted with glass cylinders coated with a gold thin film, and then functionalized with a SAM of mercaptohexadecanoic acid (MHA). Solutions with concentrations of  $(4\text{--}10) \times 10^{-3} \text{ M Ca}^{2+}$  were employed. Surface separations  $>10 \mu\text{m}$  supported the formation of calcite crystals with comparable number densities, orientations and morphologies to those formed on the same surfaces in bulk solution (Figure 23c). Separations of  $\approx 5 \mu\text{m}$  were characterized by a change in morphology, where

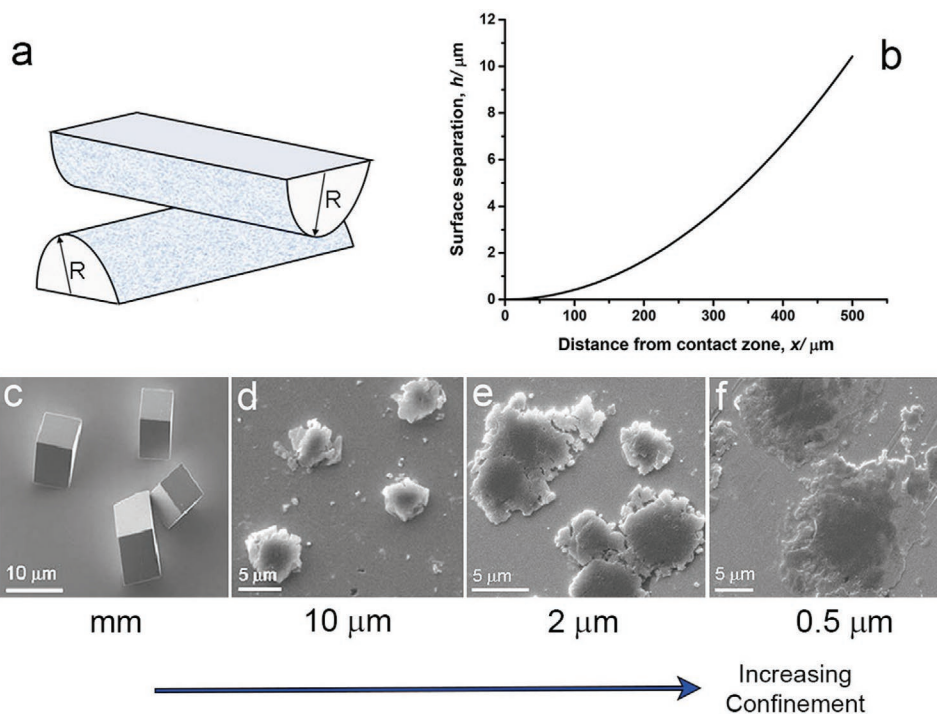


**Figure 23.** a) Schematic diagram of the crossed-cylinder configuration with radius of curvature  $R$ . b) The surface separation  $h$  plotted as a function of distance  $x$  to the contact point. c–f) Representative SEM images of calcium carbonate precipitated between crossed cylinders at approximate surface separations of millimeters (c),  $10 \mu\text{m}$  (d),  $2 \mu\text{m}$  (e), and  $0.5 \mu\text{m}$  (f). As the separation decreases the particles become less geometric and more amorphous in character. a–f) Reproduced with permission.<sup>[326]</sup> Copyright 2010, Wiley-VCH.

the crystals were now irregular in shape and bounded by many small faces (Figure 23d). No morphological features characteristic of crystalline CaCO<sub>3</sub> were seen in particles formed at surface separations of <0.5 μm, where the particles were about 10 μm in diameter, and roughly circular in shape (Figure 23f). These particles were confirmed as ACC using Raman spectroscopy, where transformation to calcite was recorded after heat treatment. Confinement—even at large length scales (sub-micrometer)—can therefore lead to stabilization of a metastable intermediate, where ACC is short-lived under comparable solution concentrations in bulk solution.

The origin of this confinement effect on the stabilization of ACC was considered. The surface free energy of ACC is expected to be lower than that of calcite, such that contact between ACC and a solid substrate should be more favorable than contact between calcite and the substrate, while the bulk free energy of calcite is lower than that of ACC. In confinement, if the particle surface area is very large with respect to the volume, an ACC particle can therefore become thermodynamically more stable than calcite. This dimension was estimated by considering ACC precipitates close to the contact zone to be discs of radius  $r$  and thickness  $d$ . The total free energy difference  $\Delta G$  between calcite and ACC consists of a bulk term  $\Delta G_{\text{bulk}}$  and a surface term  $\Delta G_{\text{surf}}$ , where the surface free-energy change for crystallization is given by

$$\Delta G_{\text{surf}} = 2\pi r^2(\gamma_{\text{s/calc}} - \gamma_{\text{s/ACC}}) + 2\pi r d(\gamma_{\text{w/calc}} - \gamma_{\text{w/ACC}}) = 2\pi r(r\Delta\gamma_{\text{s}} + d\Delta\gamma_{\text{L}}) \quad (30)$$

$\gamma_{\text{s/calc}}$ ,  $\gamma_{\text{s/ACC}}$ ,  $\gamma_{\text{w/calc}}$ , and  $\gamma_{\text{w/ACC}}$  are the free energies of the substrate–calcite interface, the substrate–ACC interface, the water–calcite interface, and the water–ACC interface, respectively.  $\Delta\gamma_{\text{s}}$  and  $\Delta\gamma_{\text{L}}$  are the differences according to Equation (2). The bulk term is

$$\Delta G_{\text{bulk}} = \pi r^2 d \frac{\Delta G_{\text{cryst}}}{V_{\text{M}}} \quad (31)$$

where  $\Delta G_{\text{cryst}}$  is the free energy of crystallization of calcite per mole, and at equilibrium

$$\Delta G = \Delta G_{\text{surf}} + \Delta G_{\text{bulk}} = 0 \quad (32)$$

These equations can then be combined to give the following equation for the value of  $\Delta G_{\text{cryst}}$  for the conversion of ACC to calcite

$$2\left(\frac{\Delta\gamma_{\text{s}}}{d} + \frac{\Delta\gamma_{\text{L}}}{r}\right) = -\frac{\Delta G_{\text{cryst}}}{V_{\text{M}}} \quad (33)$$

Taking a value of  $\Delta G_{\text{cryst}}$  at 18 kJ mol<sup>-1</sup> at 20 °C,<sup>[331]</sup>  $V_{\text{M}} = 3.7 \times 10^{-5}$  m<sup>3</sup>, and  $\gamma_{\text{s}} \approx 10$  mJ m<sup>-2</sup> and  $\Delta\gamma_{\text{L}} \approx 100$  mJ m<sup>-2</sup>, where these are order-of-magnitude estimates, one obtains

$$\left(\frac{0.001}{d} + \frac{0.1}{r}\right) = 0.24 \quad (34)$$

where  $d$  and  $r$  are in nm. Particles with micrometer-scale diameters would therefore need to have thicknesses in the order of 0.1 nm for ACC to be thermodynamically stable with respect to calcite.

The stabilization of ACC with respect to calcite at such large surface separations must therefore be kinetic in origin. It was suggested that this effect could derive from the restricted contact between the ACC precipitates and solution when they are sandwiched between the glass surfaces. Synthetic ACC can be stable for long periods of time when isolated from aqueous solution,<sup>[332]</sup> or when precipitated from nonaqueous solvents such as ethanol.<sup>[333]</sup> Further, an initial dissolution/reprecipitation step is considered essential in the transformation process.<sup>[334]</sup>

Calcium carbonate was also precipitated between crossed glass cylinders with nonfunctionalized surfaces, from solutions with low supersaturations:  $[\text{Ca}^{2+}] = [\text{CO}_3^{2-}] = 0.5 \times 10^{-3}$ ,  $1.0 \times 10^{-3}$ ,  $1.5 \times 10^{-3}$ ,  $2.5 \times 10^{-3}$ , and  $4.5 \times 10^{-3}$  M.<sup>[327]</sup> After 1 day, solution concentrations of  $[\text{Ca}^{2+}] = [\text{CO}_3^{2-}] = 4.5 \times 10^{-3}$  M yielded rhombohedral calcite crystals at  $h \geq 2.5$  μm, while plate-like vaterite crystals were observed at  $h \approx 1$  μm. Aggregates of ACC were observed at  $h \leq 0.5$  μm. Lower concentrations of  $1.5 \times 10^{-3}$  M yielded calcite at  $h > 10$  μm, vaterite and ACC at  $h \approx 5$ –10 μm and ACC alone at  $h \approx 2.5$  μm. All of the ACC particles observed at this, and lower concentrations were nonaggregated. No vaterite was observed from  $1.0 \times 10^{-3}$  M CaCO<sub>3</sub> solutions, where small calcite crystals formed at  $h > 10$  μm, and ACC particles at separations of 5 μm and below. At  $0.5 \times 10^{-3}$  M, sparsely distributed individual nanoparticles consistent with ACC were observed, but were too small to analyze with selected-area electron diffraction. These data can be compared with control experiments performed in bulk solution, where calcite was the only crystalline phase formed in  $1.5 \times 10^{-3}$  and  $1.0 \times 10^{-3}$  M solutions, and ACC was only occasionally detected. No ACC or calcite were ever found in  $0.5 \times 10^{-3}$  M solutions after 1 day. These results therefore confirm predictions from a titration study which suggest that the solubility product of ACC is an order of magnitude lower than previously believed.<sup>[335]</sup> The stabilization provided by confinement can therefore enable detection of metastable phases at solution concentrations where observation may be impossible in bulk solution. They also highlight the role of surface chemistry in directing crystallization in confined environments, where no vaterite was observed under comparable solution conditions with functionalized glass surfaces.

Investigation of the effects of confinement on the precipitation of calcium sulfate,<sup>[330]</sup> calcium phosphate,<sup>[328]</sup> and calcium oxalate<sup>[329]</sup> showed a similar pattern of results, where metastable phases were significantly stabilized between the surfaces of the crossed cylinders. Looking first at calcium sulfate, these experiments were conducted with a TEM grid inserted between the crossed cylinders to facilitate characterization of the precipitated particles (Figure 24a). Bassanite (CaSO<sub>4</sub>·0.5H<sub>2</sub>O) was the first phase formed from  $100 \times 10^{-3}$  M solutions, and fully transformed to gypsum (CaSO<sub>4</sub>·2H<sub>2</sub>O) after 10 min. In the crossed cylinders apparatus, in contrast, bundles of gypsum crystals and individual gypsum plates were present at  $h = 5$  μm, while a mixture of gypsum plates and bassanite nanorods formed at  $h = 1.5$  μm. Smaller separations of  $h = 1$ –0.5 μm were characterized by bassanite nanorods only, where their sizes decreased with a decreasing surface separation, and aggregates of 10–30 nm nanoparticles were observed in addition to small nanorods at  $h = 0.2$  μm. These results are summarized in Figure 24b,c. Conclusive evidence that the

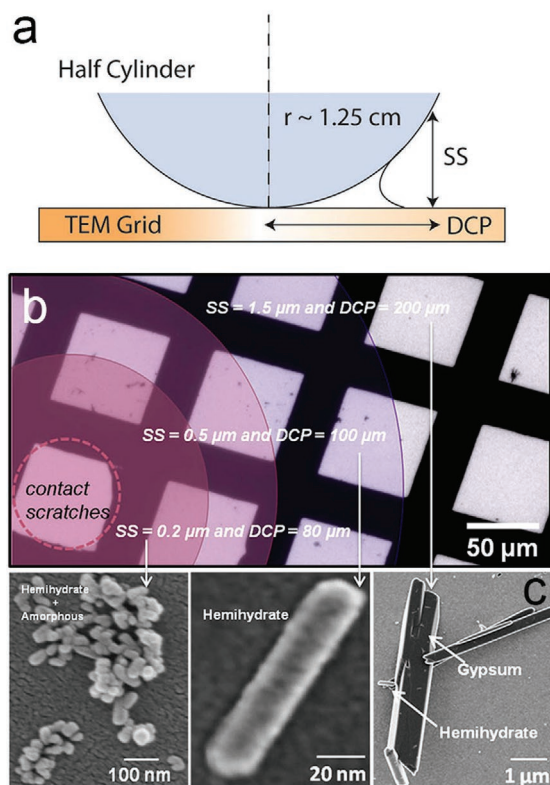


**Figure 24.** a) Schematic image of crossed cylinder apparatus, together with b) a low magnification image of a TEM grid supporting calcium sulfate particles precipitated in confinement, showing the contact point, and c) the characteristic precipitates generated at different distances from the contact point (DCP), corresponding to surface separations (SS). a–c) Reproduced with permission.<sup>[330]</sup> Copyright 2013, Wiley-VCH.

nanoparticles were amorphous  $\text{CaSO}_4$  was obtained by continued exposure to the electron beam, where partial crystallization to gypsum was apparent after 2 min. Notably, these amorphous nanoparticles were viewed after 1 h in the crossed cylinders apparatus, but could not be found in bulk solution at  $100 \times 10^{-3}$  M. Given that gypsum is more hydrated than bassanite, and the particles are nanoparticulate, a different stabilization mechanism must operate as compared with ACC. In bulk solution it has been suggested that transformation of bassanite to gypsum occurs via an aggregation-based process,<sup>[336]</sup> where this would inevitably be retarded in confinement.

Calcium phosphate, in turn, is of enormous importance as the principal inorganic component of biominerals such as bones and teeth, where it forms within the confines of organic matrices. Precipitation of calcium phosphate (CaP) in bulk solution led to the formation of 20 nm amorphous calcium phosphate (ACP) nanoparticles within 1 h, and all transformed into thin lamellae of hydroxyapatite (HAP) within 5 h. Experiments performed under the same solution conditions for 3 days using the crossed cylinders apparatus, in contrast, yielded flower-like clusters of HAP crystals at  $h = 2\text{--}5$   $\mu\text{m}$ , while at  $h = 1.5$   $\mu\text{m}$ , where the surface separation is comparable to the size of the clusters, the HAP precipitates appeared with flattened surfaces. An effect of confinement on both the morphology and polymorph of the CaP precipitates was observed

at smaller surface separations, where thin, flat plates of octacalcium phosphate (OCP) were observed in the region where  $h \approx 1$   $\mu\text{m}$ . Amorphous nanoparticles were observed in combination with the OCP platelets at  $h \approx 0.5$   $\mu\text{m}$ , while amorphous nanoparticles alone were observed at  $h \approx 0.2$   $\mu\text{m}$ .

The combined effects of spatial confinement and soluble additives were then investigated with the goal of gaining insight into the possible role of the noncollagenous proteins in the mineralization of collagen fibrils in bone. PAsp was selected as it has been considered an effective mimic of the noncollagenous proteins implicated in the mineralization of collagen with CaP. Control experiments conducted in bulk solution showed that this polymer inhibited crystallization. The initial phase formed was ACP, which transformed to OCP and ultimately HAP within 1 week. This pathway was significantly stabilized in confinement, where OCP particles were observed after 1 week at  $h \approx 1.5$   $\mu\text{m}$ , and transformation to HAP took  $\approx 2$  weeks. Further, ACP alone initially formed at  $h \approx 500$  nm. Again, neither of the mechanism proposed for calcium sulfate and calcium carbonate can operate in the CaP system. This provides strong evidence that a general mechanism must also operate in these systems. Undoubtedly, convective transport—which is often the dominant mechanism for transport of material to a growing crystal,<sup>[337]</sup> is reduced in these confined systems, such that the rate of transport between a growing, stable crystal and a dissolving metastable crystal is reduced. The amount of ACP available to a growing crystal within a certain radius must also decrease as the surface separation decreases, which would lead to slower conversion.

Finally, three forms of calcium oxalate—monohydrate ( $\text{CaC}_2\text{O}_4 \cdot \text{H}_2\text{O}$ ), dihydrate ( $\text{CaC}_2\text{O}_4 \cdot 2\text{H}_2\text{O}$ ) and amorphous calcium oxalate—were observed within the crossed cylinders apparatus.<sup>[329]</sup> Calcium oxalate monohydrate is the thermodynamically most stable phase of calcium oxalate under ambient conditions and was the principal polymorph at  $h > 1.5$   $\mu\text{m}$ . This was gradually replaced by the metastable phase calcium oxalate dihydrate as the surface separation was reduced to 0.2  $\mu\text{m}$ . Spherical nanoparticles that were morphologically consistent with an amorphous phase were observed below  $h = 0.2$   $\mu\text{m}$ . Electron diffraction analysis also suggested that they were amorphous, but this could not be confirmed by irradiation with the electron beam, as this resulted in decomposition rather than crystallization. Further experiments including the production of amorphous calcium oxalate via freeze drying confirmed that an amorphous phase can be formed in aqueous solution, where it has also been shown that CaOx can be precipitated in an amorphous form from ethanol.<sup>[338]</sup>

### 9.3. Mica Pockets

It is very difficult to manufacture environments that offer atomically sharp features. Naturally occurring environments can, however, provide access to this size regime. Campbell et al. exploited the “pockets” that commonly form along the steps on cleaved Muscovite mica (Figure 25a).<sup>[339,340]</sup> These necessarily exhibit a highly acute wedge that exhibits an angle below  $1^\circ$ , and crystallization within these structures can be studied using optical microscopy and interferometry (Figure 25b).

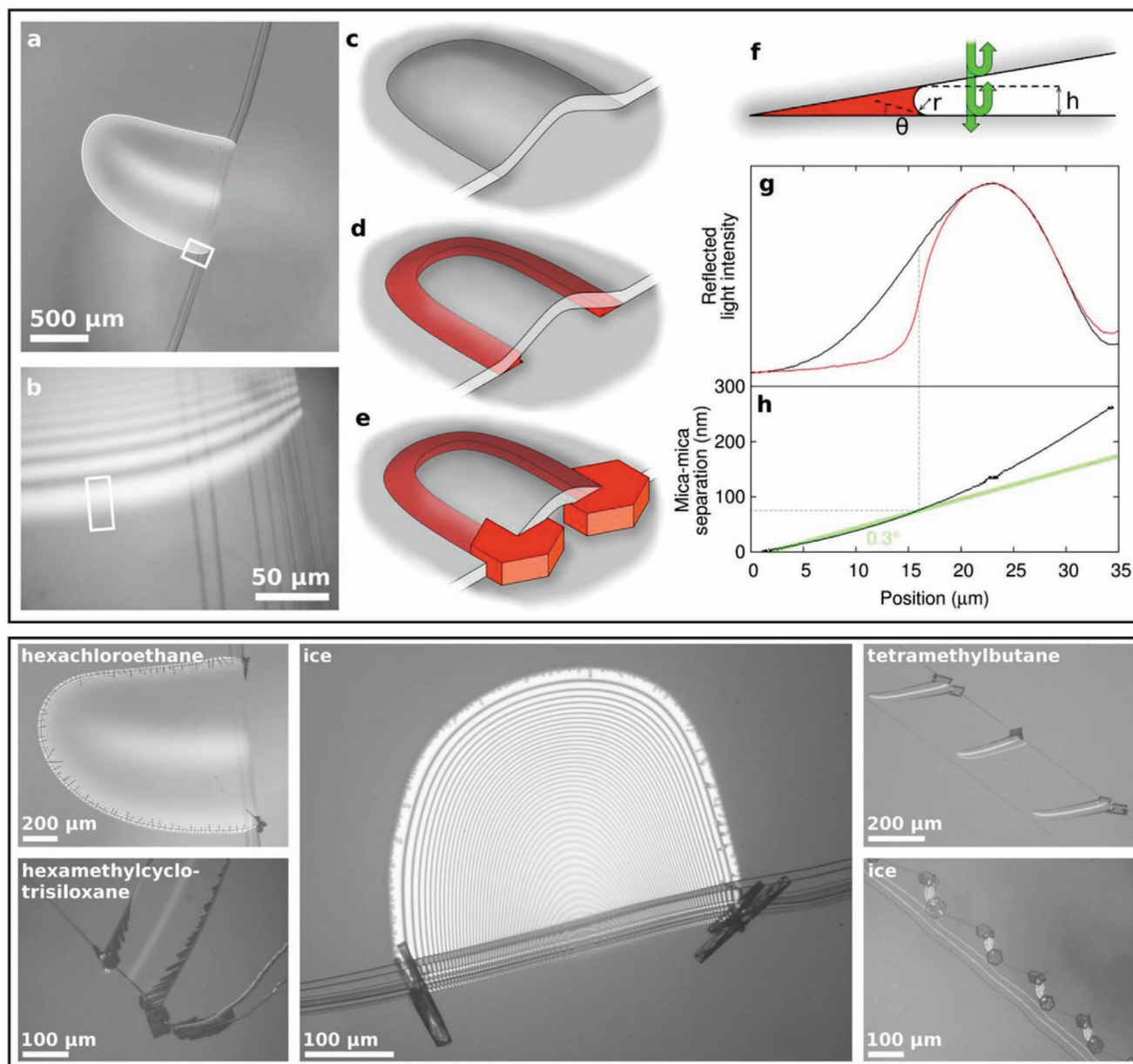


**Figure 25.** Crystallization in mica pockets. a) An optical microscopy image of a pocket. b) View of the highlighted region at higher magnification showing interference fringes. c–e) Illustration of a pocket with the growth of twinned bulk crystals shown in red. f) Wedge geometry where the condensate forms. g) The intensity of light across a single fringe for both an empty wedge (black) and a wedge with condensate of carbon tetrabromide (red). h) The profile of the wedge from the black curve; the green curve represents a  $0.3^\circ$  angle for reference. The bottom panel shows optical microscopy images of crystals of the indicated compounds crystallizing from the two corners of one or more mica pockets. Bottom images and (a)–(f): Reproduced with permission.<sup>[340]</sup> Copyright 2017, National Academy of Science, USA.

Illumination with reflected light results in a set of fringes whose intensities ( $I$ ) are described by the relation

$$I \approx I_0 + a \sin^2 \frac{2\pi z}{\lambda} \quad (35)$$

where  $z$  is the separation of the mica surfaces,  $\lambda$  is the wavelength of the light,  $I_0$  is the intensity of background light reflected from other surfaces, and  $a$  is a constant dependent on the reflectance. A bright fringe therefore first appears at  $\lambda/4$ , and at subsequent intervals of  $\lambda/4$ . Measurement of the

changes in the positions and intensities of the fringes during crystallization therefore gives detailed information about the profile of the wedge and the development of the crystals. The heights of the condensates in the pockets could also be estimated by recording the intensity profile across an interference fringe and finding the location of a sharp step in intensity from the condensate edge (Figure 25f–h).

The crystallization of three organic compounds with high vapor pressures and melting points well above room temperature—norbornane, carbon tetrabromide and camphor—was

studied.<sup>[340]</sup> Experiments were carried out in a sealed cell containing a reservoir of the material to be studied, and the mica substrate was mounted at the top such that it could be studied in reflected light, and was held at room temperature. Saturation was then achieved by increasing the temperature of the reservoir, and the temperatures of the reservoir and substrate were recorded. The pockets provided highly effective nucleation sites for all of the compounds studied (Figure 25). A condensate was first observed to form around the apex of the wedge, which thickened with time. Bulk crystals then emerged at each of the corners of the pockets. Multiple crystallization cycles were also performed in individual pockets and in almost all cases the crystals located at the pocket corners were in different orientations. This demonstrates that the two bulk crystals and connecting condensate are seldom a single crystal. The bulk crystals also formed in different orientations in separate runs, showing that the structure of the mica pocket did not direct their orientation.

As described in detail in Section 9.1, a condensate can form within the mica wedge slightly below saturation—by capillary condensation—provided that the contact angle between the condensate and mica is below 90°. To meet this criterion the interfacial free energy between the mica and the condensate must be lower than that between the mica and the vapor. As the Gibbs–Thomson effect predicts that a confined phase exhibits a reduction in the melting point that is inversely proportional to the pore size, the first condensate to form is expected to be a supercooled liquid, which subsequently freezes. However, the heights of the condensates formed within the pockets were significantly greater than estimates for liquid condensates, showing that the condensates observed experimentally were solid rather than liquid.

Ice formation in the mica pockets was also investigated by conducting experiments in a sealed cell whose temperature was controlled using a Peltier element. A stream of nitrogen at constant humidity was then flowed through the cell as the temperature of the substrate was reduced until the frost point of the gas is passed; this is the point at which the water vapor is in equilibrium with the vapor, i.e., the point at which it becomes supersaturated.<sup>[339,340]</sup> The crystallization pathway within the pocket varied according to the observed frost point. At frost points below about −42 °C, condensates were seen to form at the wedge apex in most experiments, and bulk crystals then formed at just one pocket corner, or when crystals did form at both corners, this occurred at different times. At frost points between −42 and −35 °C, in contrast, no condensate, but some small ice crystallites were initially observed along the wedge apex. Bulk crystals then usually appeared at both pocket corners at the same time. No crystallization occurred within the pocket at frost points above −35 °C, but instead water droplets condensed on the flat mica substrate and then froze.

These data are consistent with the two-step mechanism proposed by Page and Sear<sup>[341]</sup> in which crystal growth from a nanoscale pore or pocket is potentially a two-step process in which there are barriers both to nucleation within the pore and then emergence from the pore. Crystallization within the mica pockets is nucleation-limited at higher temperatures, while the emergence of the crystals from the pocket is the limiting factor at lower temperatures. Under both conditions, a continuous condensate initially forms along the apex of the wedge (although

it may be too small to observe at lower temperatures). The saturation of the vapor (with respect to ice) is smaller at the lower temperature, which creates a barrier to the emergence of the crystals from the pockets. However, the probability of nucleation is greater at the lower temperature. At higher temperatures the probability of nucleation is reduced, but the barrier to the emergence of the crystals is reduced or even eliminated. Therefore, crystals usually emerge simultaneously from the pocket corners at high temperatures, but not at low temperatures.

These experiments therefore allow direct visualization of crystallization in true nanoscale environments and demonstrate that emergence of crystals from these environments depends on a complex interplay between growth and nucleation rates.

#### 9.4. Simulations of Crystallization in Wedges

A comparison of nucleation in a wedge as compared with on a flat surface was made by carrying out Monte Carlo simulations of the crystallization of a Lennard–Jones solid in the confines of a wedge-shaped groove formed when 2 planes meet along a line, separated by an angle  $\beta$  (Figure 26).<sup>[342]</sup> Crystallization occurred from a liquid and supersaturation was controlled by varying the temperature. The simulations showed that nucleation was many orders of magnitude higher within the wedge than on a planar surface. The rate of nucleation was also strongly dependent on the angle of the wedge and reaches a maximum at  $\approx 70^\circ$  (Figure 26e). Detailed analysis of nucleation in wedges with different angles demonstrated that as a nucleus grows, close-packed {111} planes of an FCC structure grow along both faces of the wedge (Figure 26a). An FCC crystal bounded by {111} planes fits perfectly within a wedge of angle 70.5°, such that it can form defect-free, while maximizing the interaction between the crystal and the walls of the wedge, which reduces the free energy barrier to nucleation. As the angle changes, the crystals form with different defect structures (Figure 26b–d). Wedges with angles of 62° also offer an interesting case, where this corresponds to the angle separating the {111} and densely packed {101} planes in an HCP structure; a poor fit to the FCC structure occurs at this angle. Nucleation of an HCP rather than an FCC structure may therefore be anticipated. The simulations again support this analysis where the structure is principally HCP, with multiple stacking faults.

Simulations have also been conducted of ice nucleation in a wedge formed between two graphene sheets.<sup>[343]</sup> Most wedge angles supported higher nucleation rates than planar surfaces. In common with the study of Page and Sear,<sup>[342]</sup> the nucleation rate exhibits a nonmonotonic dependence on the wedge angle (Figure 26f,g). Ice nucleation is significantly promoted at angles of 45°, 70°, and 110°, while little enhancement occurs at 30°, 60°, and 135°. The simulations show that nucleation at the latter set of angles occurs far from the apex of the wedge, on the flat surface. Nucleation is thus comparable to an unconstrained system. The promotion effect at 70° and 110° can be attributed to a structural match with cubic ice, where an FCC structure bounded by {111} planes ideally fits within wedges with these angles (Figure 26h). The activity of the 45° wedge instead derives from the formation of ice with specific topological defects that bridge the wedge. At all angles where nucleation is promoted, the

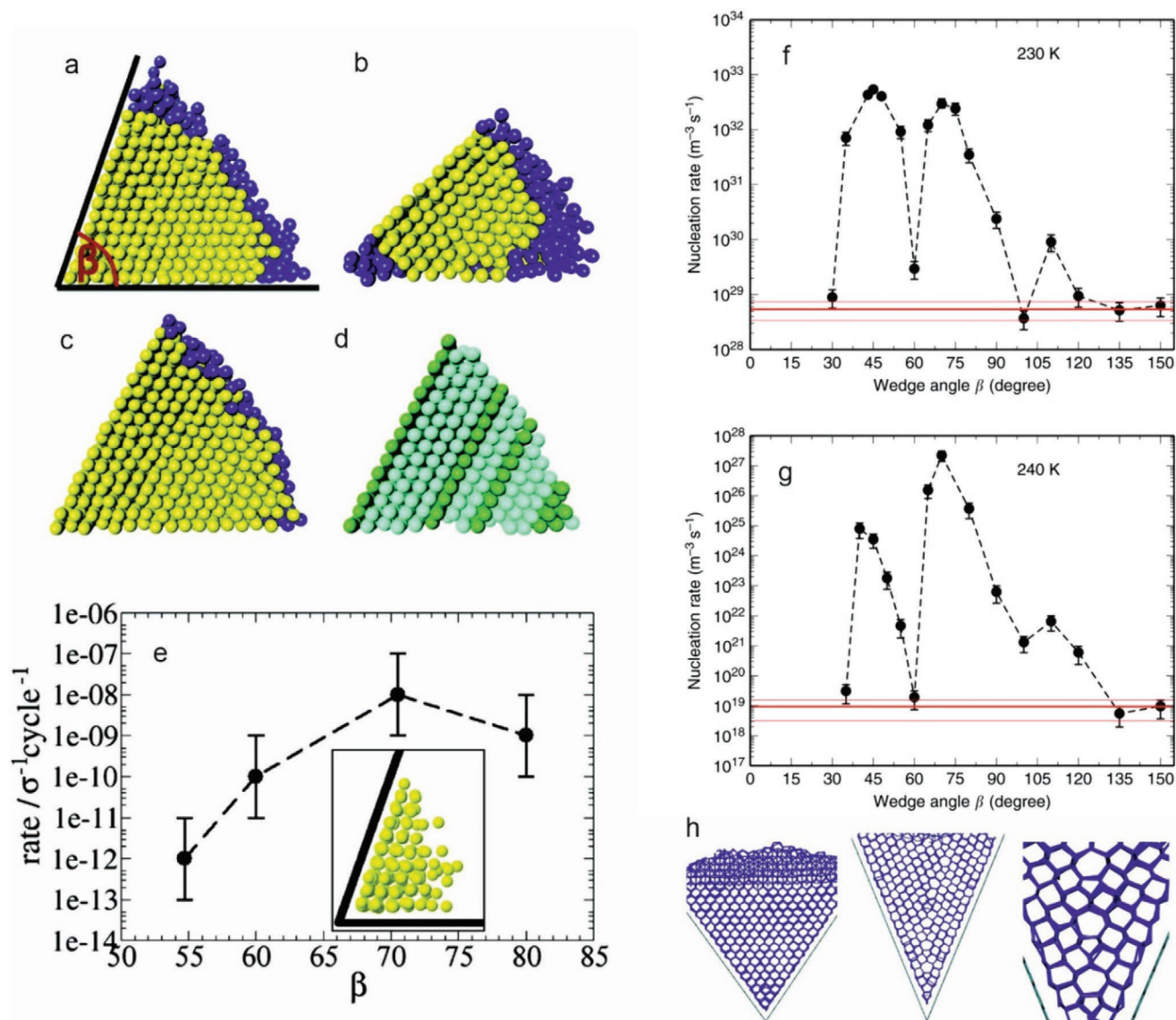


**Figure 26.** a–e) Simulation configurations of crystals in wedges. (a), (b), and (c) show snapshots of crystals in wedges of angles (denoted as  $\beta$ ) 70.5°, 45°, and 62°, respectively. Crystalline molecules are shown in yellow and fluid molecules are shown in blue. (d) is the same crystal as (c) with fcc environments shown in dark green, and those in hcp environments shown in cyan. (e) The nucleation rate as a function of wedge angle. a–e) Reproduced with permission.<sup>[342]</sup> Copyright 2009, American Chemical Society. f–h) Experimental crystallization of ice within atomically sharp wedges. f,g) The nucleation rate as a function of wedge angle at two labeled temperatures. h) Cross-section of the fully crystallized ice at 230 K within the 70° (left) and the 45° (middle) wedges with a zoom in of the 45° wedge shown on the right. f–h) Adapted under the terms of the CC-BY Creative Commons Attribution 4.0 International License (<https://creativecommons/licenses/by/4.0>).<sup>[343]</sup> Copyright 2017, The Authors, published by Springer Nature.

wedge reduces the space that the water molecules can explore. If the restriction in motion is compatible with a structural unit of ice, the entropic component of the free energy barrier to nucleation is reduced, increasing the rate of ice nucleation.

## 10. Manufactured Reaction Chambers

Thanks to the wealth of microfabrication techniques now available, it is also possible to fabricate well-defined environments tailored to the study of crystallization processes. Examples described here include a “crystal hotel” microfluidic device that comprises a

series of inter-linked circular rooms, microwells, and the sample cells used for liquid-phase TEM, which allow a flow of fluid into cells comprising planar faces, separated by 0.1–5  $\mu\text{m}$ .

### 10.1. The Crystal Hotel

Microfluidic devices offer many features that are characteristic of biological systems including confinement and flow. Crystal hotel devices were therefore constructed to explore biomineralization processes, and in particular how multiple strategies can be combined to control crystallization (Figure 27).<sup>[344]</sup>



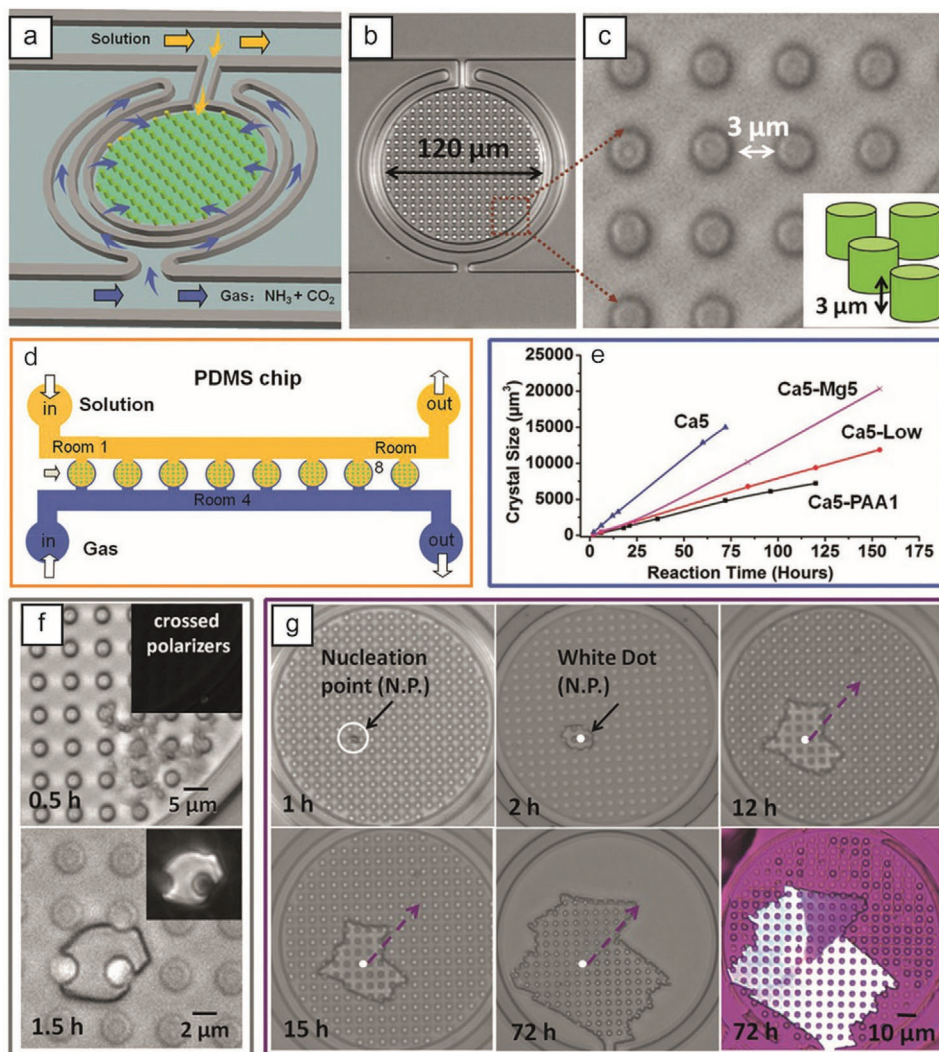


**Figure 27.** Schematic diagram of the crystal hotel. a–c) The PDMS device is composed of circular rooms, numbered R1–R8, which are internally patterned with pillars. Each room is surrounded by a circular channel (blue arrow) from which it is separated by a PDMS membrane, which is used to provide gas flow to the room, and a direct feeding channel that supplies solution (yellow arrow). d) The device is positioned on an inverted microscope and crystallization is achieved by supplying  $\text{CaCl}_2$  solution and vapor released from  $(\text{NH}_4)_2\text{CO}_3$  powder via two syringe pumps. e) Graph of the change in the crystal area with time. PAA, Mg, and Ca5 all correspond to the standard conditions given for (f) and (g), with  $[\text{PAA}] = 1 \mu\text{g mL}^{-1}$  and  $[\text{MgCl}_2] = 5 \times 10^{-3} \text{ M}$ . Low gas flow rate is identical to Ca5-low, with the exception of a gas flow rate of  $1 \mu\text{L min}^{-1}$ . f,g) Calcite crystals precipitated in the crystal hotel in the absence of additives under growth conditions of  $[\text{CaCl}_2] = 5 \times 10^{-3} \text{ M}$ , gas flow rate  $10 \mu\text{L min}^{-1}$ , and solution flow rate  $1 \mu\text{L h}^{-1}$ . f) Diffuse particles are present after 30 min, which are consistent with ACC; these are replaced by a single crystal after 1.5 h. The inset shows an image recorded between crossed polars. g) The growth of an individual crystal over 72 h. Growth is pinned such that it is retarded along the direction indicated, where this results in a domain of different orientation, as observed using a quarter-wave plate. a–g) Reproduced with permission.<sup>[344]</sup> Copyright 2015, Wiley-VCH.

Devices were fabricated from polydimethyl siloxane (PDMS) bonded to glass using common lithographic methods and comprised interlinked circular “rooms” of diameter  $120 \mu\text{m}$ ,  $3 \mu\text{m}$  heights, and volumes of  $23 \text{ pL}$ . Each room is patterned with an array of vertical pillars and a direct feeding channel supplies solution. Each room is also surrounded by a circular channel that is separated from the room by a PDMS membrane. This channel was used to provide gas flow. Calcium carbonate was used as the focus of the study and was precipitated within these environments by filling the rooms with  $\text{CaCl}_2$  solution and then continuously flowing ammonium carbonate vapor and calcium chloride solution through the appropriate

supply channels. Diffusion of ammonium carbonate vapor into the room results in the precipitation of calcium carbonate (Figure 27a–d).

Standard reaction conditions of  $[\text{CaCl}_2] = 5 \times 10^{-3} \text{ M}$ , solution flow rate  $= 1 \mu\text{L h}^{-1}$ , and gas flow rate  $= 10 \mu\text{L min}^{-1}$  resulted in the precipitation of ACC within 30 min (Figure 27f). Transformation to a single crystal of calcite occurred over the next 1.5–2 h via a dissolution/reprecipitation process, and the crystal then continued to grow at a highly uniform rate (Figure 27e). Crystals grew through the template and were entirely space-filling such that they grew right up to, and engulfed the pillars. Many crystals exhibited asymmetric external morphologies, however,

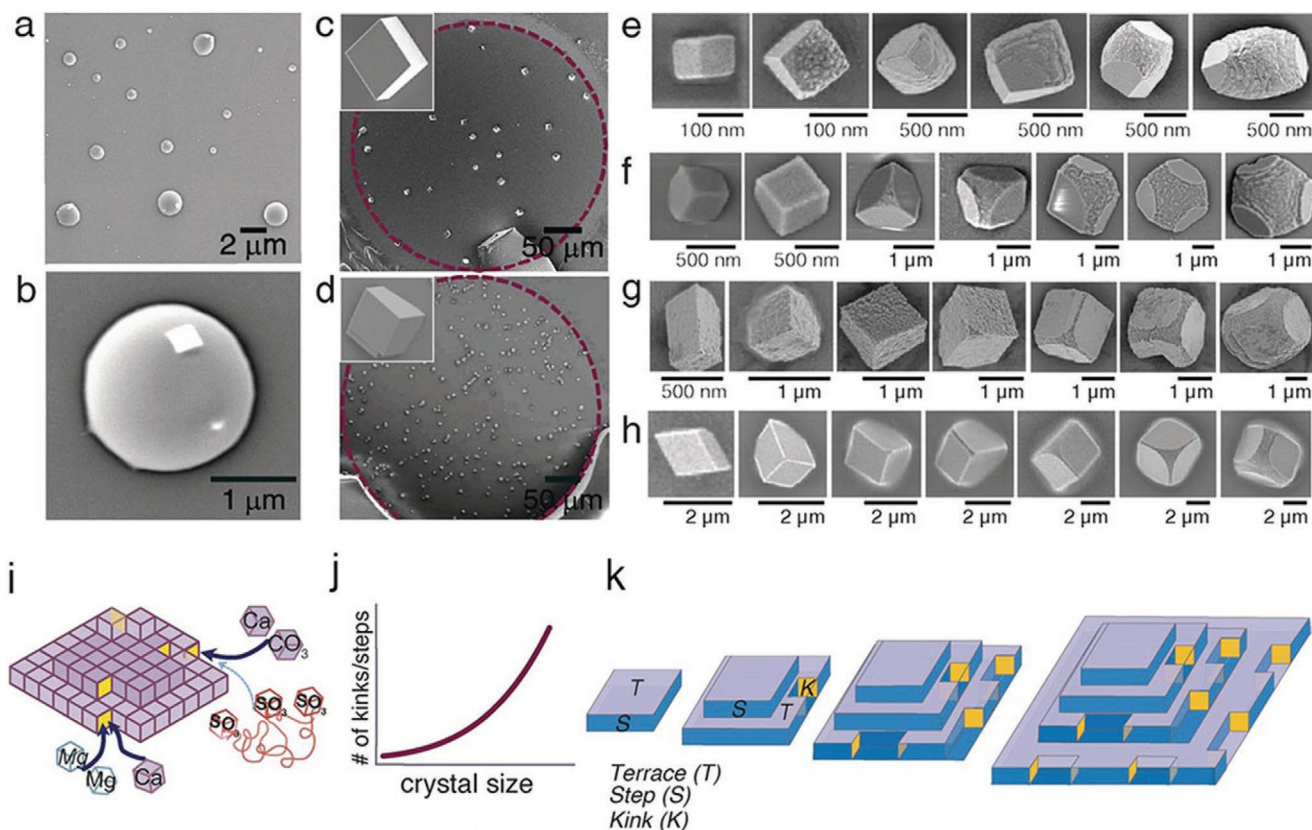


**Figure 28.** Top: a–h) SEM images of CaCO<sub>3</sub> precipitates in the crystal hotel. a,b) Amorphous calcium carbonate obtained at [Ca<sup>2+</sup>] = 2.5 × 10<sup>-3</sup> M and [Mg<sup>2+</sup>] = 1.25 × 10<sup>-3</sup> M. c,d) Calcite crystals grown without additives at: c) [Ca<sup>2+</sup>] = 5 × 10<sup>-3</sup> M, and d) [Ca<sup>2+</sup>] = 50 × 10<sup>-3</sup> M. The insets show crystals at higher magnifications. e–h) In the presence of: e) [Ca<sup>2+</sup>] = 2.5 × 10<sup>-3</sup> M and [Mg<sup>2+</sup>] = 1.25 × 10<sup>-3</sup> M, f) [Ca<sup>2+</sup>] = 2.5 × 10<sup>-3</sup> M and [PSS] = 500 μg mL<sup>-1</sup>, g) [Ca<sup>2+</sup>] = 2.5 × 10<sup>-3</sup> M and [PSS] = 250 μg mL<sup>-1</sup>, and h) [Ca<sup>2+</sup>] = 1.25 × 10<sup>-3</sup> M and [PSS] = 250 μg mL<sup>-1</sup>. Bottom: i) Schematic summarizing how additives affect calcite morphologies. i) Mg<sup>2+</sup> and PSS compete with the Ca<sup>2+</sup> and CO<sub>3</sub><sup>2-</sup> growth units to bind to kink sites (yellow) at step edges. The thickness of the arrows indicates the relative binding strength. j) The length of step edges and hence the number of kink sites increases with the crystal size. k) For simplicity only one {104} face is shown. Newly formed calcite crystals have few kink sites and the probability of additive binding is low. As the crystals grow, increase in the length of step edges and associated kink sites raises the probability of additive binding. Ultimately, the crystals are sufficiently large for additive binding to cause a change in the macroscopic crystal shape. a–k) Reproduced with permission.<sup>[345]</sup> Copyright 2017, Wiley-VCH.

due to pinning at a particular site (possibly at defects) within the reaction chamber (Figure 27g).

Control over crystallization could be achieved by varying the gas flow rate and adding soluble additives (Figure 27d). Increase in the flow rate resulted in a concomitant increase in the number of crystals formed within the rooms, while magnesium ions and PAA reduced the rate of crystal growth. Notably, pinning events were rare in the presence magnesium ions, such that the crystals exhibited isotropic morphologies and could grow to fill the entire room. In contrast, pinning was extremely common in the presence of PAA and crystals exhibited highly irregular morphologies. Finally, these environments were used to explore a key feature of many biomineralizing systems—crystal orientation. As a mimic of the organized organic matrices that direct crystallization in vivo, the base of the rooms was functionalized with carboxyl-terminated alkylsilane monolayers. These SAMs supported faster crystal growth and were able to select the same unique crystal face as occurs in bulk solution.

An alternative crystal hotel device was also used to explore the influence of soluble additives on the early stages of growth of calcite (Figure 28).<sup>[345]</sup> Due to the challenges associated with

studying dynamic phenomena on the nanoscale, and monitoring the development of crystals by isolating them from solution at different reaction times, it can be highly challenging to investigate how additives influence the growth of crystals in the nanoparticle regime. As crystallization processes proceed more slowly in confinement than in bulk solution, suitable constrained environments can provide an excellent opportunity to monitor the morphological development of small crystals. Crystal hotel devices were therefore designed to offer a sequence of 48 rooms with diameters of 400 μm and heights of 150 μm. The rooms are linked by microchannels and do not contain pillars. The rooms were filled with CaCl<sub>2</sub> solution containing either magnesium ions or poly(styrene sulfonate) (PSS), and calcium carbonate was precipitated by then flowing ammonium carbonate vapor only through the supply channel. The reactions were terminated at a selected time by flowing ethanol through the device.

ACC was the first phase formed in all cases (Figure 28a). Its transformation to calcite was retarded in the presence of both additives, which enabled this process to be studied. Many of the ACC hemispheres formed in the presence of Mg<sup>2+</sup> exhibited small rhombohedral particles consistent with calcite on

their surfaces (Figure 28b), which supports the suggestion that conversion of ACC into calcite is initiated adjacent to the ACC/solution interface.<sup>[334]</sup> The morphological development of the calcite crystals was then studied, and rather surprisingly, perfect rhombohedra were observed until the crystals reached sizes of  $\approx 1 \mu\text{m}$  in the presence of PSS ( $[\text{Ca}^{2+}] = 2.5 \times 10^{-3} \text{ M}$  and  $[\text{PSS}] = 500 \text{ mg mL}^{-1}$ ) (Figure 28f–h) and 100–500 nm in the presence of  $\text{Mg}^{2+}$  ions ( $[\text{Ca}^{2+}] = 2.5 \times 10^{-3} \text{ M}$  and  $[\text{Mg}^{2+}] = 1.25 \times 10^{-3} \text{ M}$ ) (Figure 28e). Initial modifications of the morphologies comprised truncations of the edges and roughening of the surfaces, and the crystals then developed to exhibit the same morphologies as those observed in bulk solution.

These results were rationalized by considering the mechanisms by which additives interact with calcite crystals (Figure 28i–k). Screw dislocations and islands on the calcite surface exhibit acute and obtuse step edges, and additives typically bind preferentially to one edge type. The growth of sparingly soluble compounds such as calcite are further governed by the availability of kink sites on these steps, where strong binding can change the shape, speed, and separation of the steps. This ultimately leads to changes in the macroscopic form of the crystal. The influence of an individual additive therefore depends on its residence time at a kink site as compared to the propagation rate of the steps. As very small crystals exhibit short steps and few kink sites, the probability that an additive binds to a kink site and prevents completion of that growth layer is very small. As the crystal grows, the area of the faces, the length of the step edges, and the number of kink sites all increase, which increases the chance that an additive will influence the propagation of an individual step. Strongly binding additives therefore induce changes in morphologies at smaller crystal sizes, as observed for  $\text{Mg}^{2+}$  versus PSS. This model was supported by simple calculations that estimated the fraction of kink sites that are occupied by additives rather than calcium carbonate growth units, as a function of the crystal size. In keeping with the experimental data, these showed that the “critical size” at which a crystal begins to change morphology is dependent on the binding strength and concentration of an additive, and the solution supersaturation.

## 10.2. Microwells

Lithographic methods have been used to generate arrays of microwells on a transparent glass base.<sup>[346]</sup> The wells comprise gold side-walls of height 20 nm and diameters of 2–10  $\mu\text{m}$  (giving volumes of 0.8–2 fL) and the solution can be constrained to the wells by functionalizing the wells such that the base is hydrophilic and the top surface separating the wells is hydrophobic. Crystallization of lysozyme in these microwells yielded tetragonal crystals in the 10  $\mu\text{m}$  wells, as was also observed under bulk hanging drop conditions. Both tetragonal and plate-like crystals formed in 3  $\mu\text{m}$  wells. Yet smaller wells supported the formation of single protein crystals with plate-like shapes. The change in morphologies can be attributed to the faster evaporation rate of the small volumes. Similar changes in morphology with a reduction in the well volume were also observed for thaumatin and glucose isomerase. Yet smaller organosilane nanopores with diameters of  $\approx 90 \text{ nm}$  and depths of a few

nanometers were also formed by particle lithography, and were used to support the formation of erbium-doped yttrium oxide nanoparticles.<sup>[347]</sup> The pores were filled with a precursor solution and dried, and then heated at up to 800 °C to generate individual oxide nanoparticles in each nanopore.

## 10.3. Liquid-Cell for TEM

Liquid cells have been developed for use with transmission electron microscopes to enable analyses to be conducted in real time, in solution. The cells must therefore be very thin to allow transmission of the electron beam, and are constructed with silicon nitride windows that are separated by spacers that typically range between 0.1 and 5  $\mu\text{m}$  in size. These cells have been widely used to study crystallization processes, but the contribution of the confined environment to the processes occurring within the cells remains poorly characterized.

Liquid cell (LC)-STEM was used to study calcium carbonate precipitation from a  $10 \times 10^{-3} \text{ M}$  solution in a cell constructed using 500 nm spacers.<sup>[348]</sup> The results were then considered in light of finite element simulations of the flux of ions from a reservoir to a growing calcite crystal confined between parallel plates.  $\text{CaCl}_2$  and  $\text{Na}_2\text{CO}_3$  solutions were mixed prior to flowing them through the cell at 300  $\mu\text{L min}^{-1}$ . No precipitation was observed in a viewing area of  $400 \times 400 \mu\text{m}$  even after 30 min at a magnification of 20 k (corresponding to a dose of  $3 \text{ e}\text{\AA}^{-2}$ ). Increase of the magnification triggered precipitation due to the influence of the electron beam, but these dissolved on reduction of the dose. The phase of the particles formed was not determined. Notably, these results do not entirely agree with those of Nielsen et al, who also studied calcium carbonate precipitation from  $\text{CaCl}_2$  and  $\text{NaHCO}_3$  solutions flowed through a LC-TEM cell.<sup>[349]</sup> They again noted that the formation of ACC was influenced by the electron beam, but the precipitation of crystalline polymorphs were unaffected and they also formed in regions of the cell that were not exposed to the electron beam. The lateral growth rate of the crystals was also not affected by the thickness of the cell.

Kroger et al. carried out 2D finite element calculations to consider the growth of a calcite crystal confined between two parallel plates with lateral dimensions of 5 mm and separated by 500 nm.<sup>[348]</sup> Two processes were considered: the rate of incorporation of ions into the growing crystal, and the flux of ions from the reservoir. Unlike the experiments where new solution is continuously flowed through the cell, the simulations considered a static system with an infinite reservoir or ions. The simulations demonstrated that the dimensions of the depletion zone around the crystal is affected by the degree of confinement. The concentration of ions around the crystals rapidly recovers to bulk solution levels at a plate separation of 1 mm, while significant effects are seen even at 10  $\mu\text{m}$ . This effect will therefore limit the growth rate of crystals, and the nucleation of new crystals within the depletion zone will be limited.

## 11. Crystallization in Porous Media

The crystallization of minerals in heterogeneous porous media is a widespread phenomenon in geochemistry and building

materials, and is observed in a wide range of settings and environments.<sup>[350–352]</sup> With relevance to processes including the degradation of rocks in natural systems, and of porous building materials such as stone, brick, cement and concrete,<sup>[11]</sup> the formation of ore deposits,<sup>[353]</sup> the storage of carbon dioxide<sup>[13,14]</sup> and sequestration of toxic metals in minerals,<sup>[15]</sup> and the extraction of oil,<sup>[354–357]</sup> this topic attracts enormous interest and is the subject of an extensive body of literature. Predicting the outcome of crystallization within these porous media is an extremely complex problem that depends on an ability to model both transport processes and crystal nucleation and growth within confined volumes.<sup>[358,359]</sup> It is therefore dependent on the structure of the porous medium, as defined by the pore size distribution, pore number density, and the connectivity of the pores.<sup>[360]</sup>

Highlighting some salient examples, the precipitation of salts within porous natural and man-made systems is often associated with weathering processes, where damage to these materials occurs due to the force exerted by the crystal on the walls of the porous network.<sup>[361–365]</sup> These crystallization reactions are typically driven by cycles of evaporation and rehydration within the pore space. This is often associated with the build-up of very high supersaturation levels, where porous media can be extremely effective at suppressing nucleation.<sup>[361,366]</sup> Precipitation of salts in porous rocks that host oil and gas deposits causes additional problems by clogging the system by essentially decreasing the porosity in pivotal areas of flow.<sup>[354,355]</sup> The incompatible mixing of formation brines and injection water is often the cause of this decrease in porosity, as a variety of sulfates are known to precipitate in these environments.<sup>[367–369]</sup> These issues can also occur in geothermal systems during the capturing of CO<sub>2</sub> in underground well systems.<sup>[356]</sup>

In this section we aim to provide a brief overview of this topic, where we have chosen to highlight studies that focus on the influence of confinement on crystal nucleation and growth. Understanding of crystallization within porous rocks and man-made building materials is extremely challenging due to the heterogeneous structures of these media. Further, specialist techniques such as X-ray tomography<sup>[364,370–374]</sup> are required to characterize the structure of these materials and to determine the locations and structures of the growing crystals. A range of model systems with well-defined structures and which can be characterized using laboratory techniques have therefore been employed and are outlined here.

### 11.1. Crystallization in Silica Gels

Much of our current understanding of crystallization in porous media comes from early work using silica gels, where these possess a number of properties that make them well-suited to this purpose.<sup>[360,375–380]</sup> Silica gels have the advantage that they are optically transparent, such that it is possible to use optical microscopy to monitor the formation of crystals over time. They can also be prepared within any selected environment, and their porosity controlled. A key factor governing crystallization within porous media is that it relies on the mass transport of dissolved ions through the medium until a level of supersaturation (the critical supersaturation,  $S_{\text{crit}}$ ) is achieved that supports crystal nucleation and growth. A beautiful feature of silica gels

as a model system is that it is possible to monitor the evolution of the supersaturation in both space and time, where this can be achieved by taking gel columns at different reaction times and cutting them into slices.<sup>[375]</sup> The total concentrations of the free ions in each slice is then determined by chemical analysis. An equation system formed of mass-balance equations and ionic association equilibria is then solved iteratively to produce the concentrations of all of the relevant ionic species. Finally, the ionic strength, activity coefficients and supersaturation are calculated, where that the calculation of the ionic strength involves the concentration of all the main species in solution.

#### 11.1.1. Evolution of Supersaturation

A series of experiments were conducted using a U-tube shaped double diffusion-reaction system where these systems are characterized by two vertical reagent reservoirs separated by a horizontal silica hydrogel column (**Figure 29**). The structure, and therefore transport properties of the gel are controlled during the preparation stage, which typically involves the acidification of a solution of sodium silicate (Na<sub>2</sub>SiO<sub>3</sub>) to a given pH.<sup>[360]</sup> The solution is then placed in the horizontal column where it polymerizes and solidifies into a gel. The silica gel contains ≈95 vol% of solution within the pores and the pore size varies from 100 to 500 nm in diameter.<sup>[351]</sup> The silica gel allows counter diffusion of the chosen reagents (e.g., CaCl<sub>2</sub> and Na<sub>2</sub>SO<sub>4</sub> for gypsum), such that after a given amount of time—determined by the transport properties of the gel—the reagents in the column meet and precipitation occurs.<sup>[360]</sup>

Initial experiments focused on the crystallization of gypsum (CaSO<sub>4</sub>·2H<sub>2</sub>O) within silica gels.<sup>[375]</sup> The gel columns were cut into 48 slices and were chemically analyzed as described above. Experiments were carried out for 24–50 days at various concentrations of mother solutions. With solutions of equal concentrations the highest saturation was obtained in the middle slice regardless of incubation time. The experiments that ran for 24 and 32 days were undersaturated ( $S < 1$ ) throughout the gel column whereas supersaturation developed at slices 6 and 3 in experiments run for 40 and 50 days, respectively. For all times, the highest degree of supersaturation was found slightly shifted from the middle of the column (slice 15) due to the lower diffusion coefficient of the sulfate ion.

Experiments were also conducted by varying the concentration ratios of the mother solutions (1 M CaCl<sub>2</sub>: 0.3 M Na<sub>2</sub>SO<sub>4</sub> and 0.3 M CaCl<sub>2</sub>: 1 M Na<sub>2</sub>SO<sub>4</sub>) for different diffusion times (32–80 days).<sup>[375]</sup> Supersaturation was once more achieved in experiments with residence times of 40 days or higher, but the supersaturation region was narrower than when equimolar solutions were employed. The supersaturated region was additionally skewed toward the higher concentration reactant for lower diffusion times (32 and 40 days) and progressively shifted toward the lower concentration reactant with increasing time (80 days). The shift in the position of maximum supersaturation demonstrates the importance of the initial reagent concentrations. These findings differ greatly from oversimplified mass transfer models. Additional information about the actual concentration distribution of supersaturation is required to interpret the location of the first precipitate. The ratio of

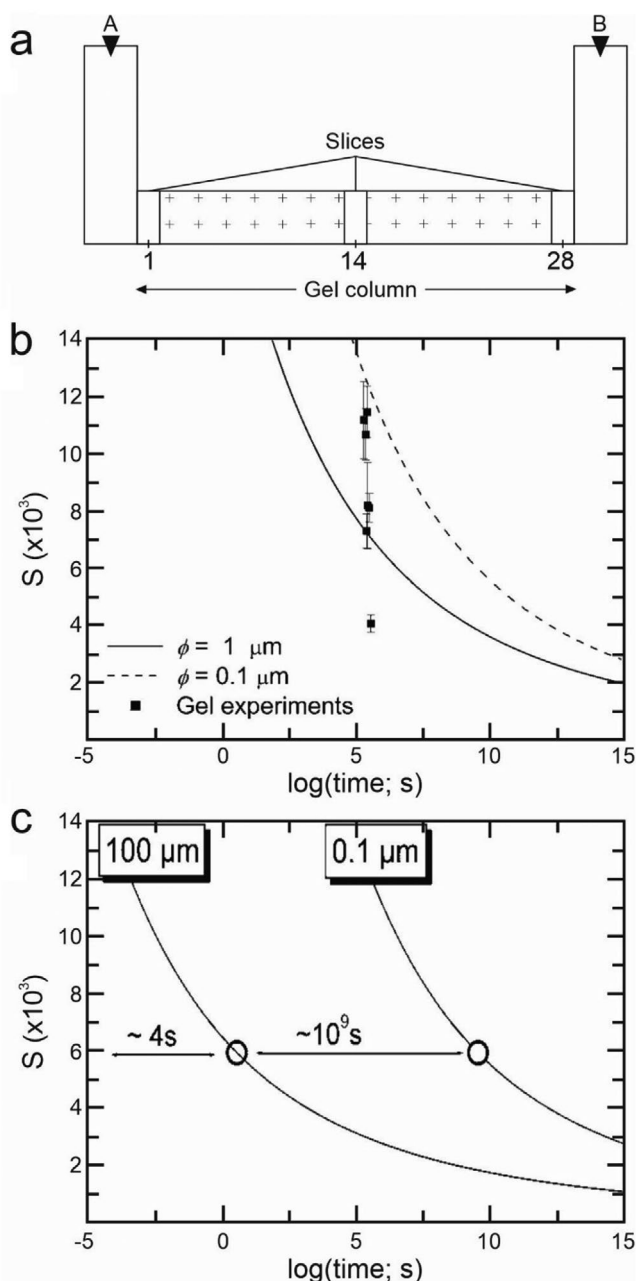


**Figure 29.** a) A schematic diagram of U-tube experimental arrangement. Typically cut into 28 equal sized slices for chemical analysis. b) A supersaturation–nucleation–time (S–N–T) diagram for pore sizes 1 and 0.1  $\mu\text{m}$ . c) Pore-size effect on the homogeneous nucleation in a porous medium with two pore sizes. a) Adapted with permission.<sup>[384]</sup> Copyright 2014, Mineralogical Society of Great Britain and Ireland. b,c) Reproduced with permission.<sup>[384]</sup> Copyright 2014, Mineralogical Society of Great Britain and Ireland.

concentrations of both reagents also dictates where nucleation occurs because the nucleation probability is very small unless this ratio is close to unity (termed as “equality range” condition).<sup>[376]</sup>

Building from these initial results, similar crystallization experiments were conducted with both barium and strontium carbonates (witherite and strontianite).<sup>[376]</sup> In these experiments the pH of the solution throughout the gel column

was determined by adding a colored pH indicator during the preparation of the gel. Initially, the entire column was of uniform pH. However, as the diffusion of reagents progressed, the gel developed a color banding which could be used to determine the pH profile. The pH profile paralleled the mass-transfer phenomena, steadily increasing in pH from 5.5 in slice 1–10.5 in slice 21, where it remains constant to slice 28. As expected, the pH and total carbon concentrations behaved similarly throughout the gel column at all diffusion times, where a higher pH corresponds to higher total carbon concentrations. The maximum supersaturation was shifted toward the carbonate reservoir, where this can be explained by the distribution of the carbon-containing species  $\text{H}_2\text{CO}_3^0$ ,  $\text{HCO}_3^-$ , and  $\text{CO}_3^{2-}$ . This again depends on the pH.<sup>[376]</sup> The profiles of these species shows that  $\text{H}_2\text{CO}_3^0$  is the dominant species at low pH (5.5, slices 1–7), but with increasing pH and carbon concentration  $\text{HCO}_3^-$  becomes more important (slices 7–16), until  $\text{CO}_3^{2-}$  finally becomes the prevailing species in slices 16–28.<sup>[376]</sup>

The influence of the concentrations of the reagents was also explored.<sup>[376]</sup> While the morphologies of the crystals did not change, the number of crystals did vary, where the nucleation density was highest at high concentrations of both reagents, and decreased as the concentrations of one or both of the reagents were reduced. Perhaps the most important information obtained from these experiments, however, is the location of the first precipitates. In all experiments, the precipitate location did not coincide with the supersaturation maximum. This demonstrates that the critical supersaturation condition is not the only requirement for nucleation to occur. Further, the nucleation zone is limited to a narrow range of concentration ratios and corresponds to  $[\text{CO}_3^{2-}]/[\text{Ba}^{2+}]$  or  $[\text{CO}_3^{2-}]/[\text{Sr}^{2+}]$  ratios which are close to unity.<sup>[376]</sup> This is consistent with the “equality range” condition for crystal nucleation.<sup>[360]</sup> Thus, both the critical supersaturation and the “equality range” conditions must be met in order to achieve nucleation. Similar results were also obtained in the barite system.<sup>[360]</sup>

These analyses also fail to take into account that the supersaturation in these systems is not constant, but varies with time and the location in the gel column.<sup>[360]</sup> In time-dependent and nonhomogeneous systems we must consider the saturation threshold,  $S_{\text{th}}$ , which is a kinetic concept that corresponds to the metastability limit that can be achieved for the specific set of conditions.<sup>[360,378]</sup> It is also noted that the induction time is a difficult quantity to measure as it relies upon the ability to detect the onset of critical nuclei. Thus, Prieto and co-workers opted to use an alternative measure called the “experimental waiting period.”<sup>[360,378]</sup> Utilizing these concepts allows the supersaturation rate to be calculated at specific reaction times, where this is defined as the derivative of the supersaturation versus time.<sup>[378]</sup>

The relationship between the supersaturation threshold and the supersaturation rate was investigated in a number of nucleation experiments on a variety of minerals including barite, strontianite, witherite, and gypsum.<sup>[377,378]</sup> The experimental waiting period, supersaturation threshold and the supersaturation rate were determined for multiple concentrations of the mother solutions and a clear relationship was observed between the starting reagent concentrations and the waiting time. This is expected as the initial concentration dictates the supersaturation rate of the system.<sup>[378]</sup> The supersaturation rate also affects the supersaturation threshold, such that

supersaturation rate  $\propto$  (supersaturation threshold)<sup>*m*</sup> (36)

where *m* is an empirical coefficient that is determined by the crystallizing material. This relationship is linear in ln–ln space, where the relationship between the supersaturation rate and threshold is analogous to that of the cooling rate and supersaturation.<sup>[377]</sup> The slope of the curves corresponds to the empirical coefficient *m*, which should be a function of the amount of particles that form the critical nucleus.<sup>[377]</sup>

### 11.1.2. The Effect of Additives

The influence of additives on crystallization in silica gels has also been studied, where this is relevant to crystallization in porous media in the environment and offers a potential strategy for inhibiting crystallization. Investigation of the effect of the inhibitors phosphero-modified poly(acrylic acid) derivative and phosphero-modified poly(maleic acid) on the crystallization of barite in silica gels showed that both of these increased the supersaturation threshold.<sup>[377,378]</sup> However, the relationship between the rate and threshold remained linear in ln–ln space. The slope of this graph was also much higher than for pure barite, which is indicative of an increase in the size of the critical nucleus in the doped solutions.<sup>[377,378]</sup>

The effect of magnesium ions on calcium carbonate precipitation attracts particular interest due to the high concentration of this ion in seawater, and the significant effects it has on crystal polymorph and morphology.<sup>[379,381,382]</sup> In the absence of Mg<sup>2+</sup>, the first crystals formed in silica gel columns were always calcite with typical rhombohedral forms. With time, crystals began to grow into hopper crystals of rhombohedral form with nonflat wavy faces. After longer incubation times, aragonite spherulites formed closer to the carbonate reservoir. The supersaturation increases from the calcium reservoir to the carbonate reservoir as does the metastability, which explains the presence of metastable aragonite proximal to the carbonate reservoir.

Addition of magnesium ions yielded an identical crystallization sequence, but the elapsed time between calcite and aragonite crystallization increases as a function of the magnesium concentration. The Mg<sup>2+</sup> ions also had a dramatic effect on the morphology of the calcite crystals, where these initially developed as spheres with very rough surfaces. Longer reaction times then produced a wide range of morphologies from dumbbell-like forms to bundles or sheaf-like crystals. The magnesium content of the calcite crystals also increased with increasing supersaturation (toward the carbonate reservoir) and the crystals displayed compositional zoning consistent with nonequilibrium selection of surface composition. The morphologies observed correspond to the supersaturation profile within the gel. Further investigations of a variety of other systems showed that compositional zoning is very easily achieved in gels that have high degrees of supersaturation and metastability compared to bulk solutions.<sup>[380,383]</sup>

### 11.1.3. Effect of Pore Size

The dependence of crystallization on pore size has been observed in many systems.<sup>[351,358,384]</sup> However, it can be

extremely difficult to obtain systematic data regarding this effect. 1) Knowledge of the pore-size distribution is critical to our understanding of the crystallization behavior, where the existence of nanopores and macropores can drastically change the potential for crystallization in any of the pore size ranges. This information can be difficult to obtain. 2) The shape of the pores can influence crystallization, where this effect will vary according to the preferred habit of a given crystal. 3) The interconnectivity of the pores and the permeability will affect how ions are transported throughout the medium, and thus the development of supersaturation. 4) The solubility of the particular crystals must be taken into account as supersaturations vary enormously for soluble and poorly soluble crystals. 5) It is very difficult to perform systematic studies in which just one parameter—such as the size, interconnectivity or pore-size distributions—is varied. This makes it very challenging to compare results obtained from different systems.

Recently, supersaturation–nucleation–time (S–N–T) diagrams have been used to predict nucleation in porous media based on experimental data from barite crystallization in silica gels (Figure 29b).<sup>[384]</sup> Using classical nucleation theory as a framework, S–N–T diagrams were calculated for cases of homogeneous and heterogeneous nucleation for different pore sizes. All experimental saturation thresholds were seen to fall between the calculated curves for pore sizes of 0.1 and 1 μm, showing that nucleation is favored in larger pores. The induction time was also nine orders of magnitude greater in the 100 μm pores as compared with 0.1 μm at a supersaturation level of 6000 (Figure 29c).<sup>[384]</sup> This finding was further supported by a set of experiments in which calcium carbonate was precipitated in an amorphous-silica medium with a bimodal distribution of pore sizes.<sup>[385]</sup> Precipitation was uniquely observed in the larger pores (≥30 μm).

Many explanations exist for the inhibition of nucleation in smaller pores,<sup>[350,351]</sup> where these are summarized here. 1) As described by classical nucleation theory, nucleation is a stochastic process, that requires ions to come together to form clusters.<sup>[351]</sup> Only when these reach a critical size is growth energetically favorable. In small pores, the probability of these clusters forming, even at large supersaturations, is decreased.<sup>[351]</sup> 2) Interacting versus noninteracting pore walls will influence crystal growth.<sup>[384,385]</sup> [350] Indeed, precipitation of calcium carbonate within surface-functionalized controlled pore glasses (CPGs) revealed that the surface chemistry influenced crystallization within the pores,<sup>[385]</sup> and that favorable interactions can promote growth within smaller pores. 3) Crystals with large surface to volume ratios can exhibit higher solubilities than their bulk counterparts.<sup>[351]</sup> Referred to as pore-size-controlled solubility,<sup>[386]</sup> this suggests that a solution can simultaneously be undersaturated and supersaturated with respect to a crystal in small and large pores respectively. This may contribute to the precipitation of salts in larger pores.<sup>[351]</sup> 4) The growth of crystals via the aggregation of nanocrystal building blocks could potentially be retarded in small pores.

## 11.2. Influence of Crystallization on the Confining Medium

Crystallization in porous media generally causes the porosity and permeability of the material to decrease as crystals grow

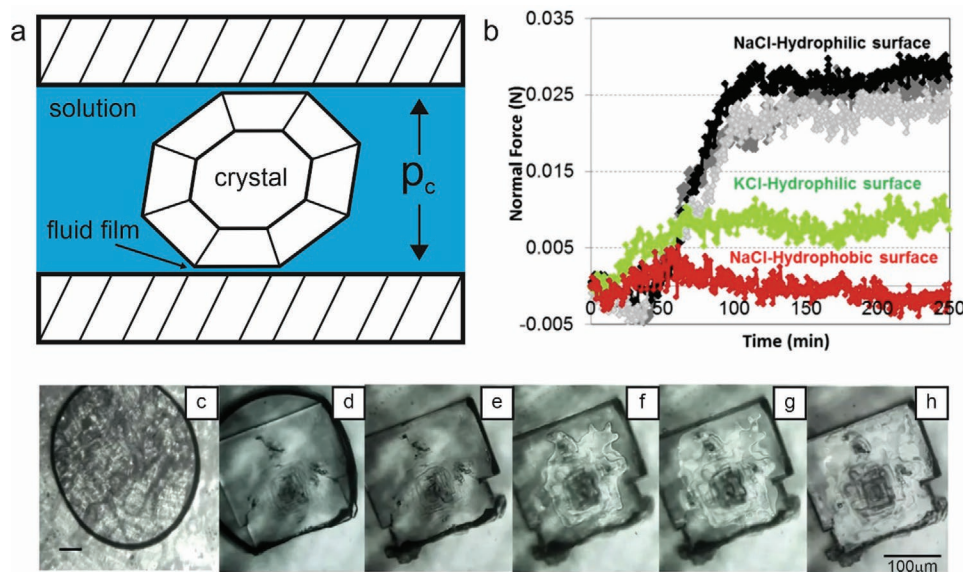


**Figure 30.** a) Schematic diagram showing the crystallization pressure ( $p_c$ ) exerted onto the confining walls highlighting the importance of the presence of a thin fluid film. b) Experimental results of the measured force for three NaCl (black and gray), one KCl (green), and one NaCl with hydrophobic glass plates (red). c–h) The evaporation of NaCl solution between two hydrophilic glass plates. c) Droplet prior to precipitation, d) lateral crystal growth, e–h) evolution of the step growth on the confined face with the development of efflorescence on the left corner of the crystal. b)–h) Reproduced under the terms of the CC-BY Creative Commons Attribution 4.0 International License (<https://creativecommons/licenses/by/4.0>).<sup>[397]</sup> Copyright 2016, The Authors, published by Springer Nature.

and fill the pore space. These crystals can continue to grow while in contact with pore walls, such that they exert a certain stress, which if sustained, can damage the host material. This is necessarily a cause of great concern in the industrial world due to the damage done to porous building materials ranging from stone to concrete. This effect has been known for some time, where Becker and Day demonstrated as long ago as the turn of the 20th century that crystals in saturated solution could not only lift their own weight but a considerable amount of surplus weight as well.<sup>[387,388]</sup> Two very important conclusions were drawn from these experiments.<sup>[366,389,390]</sup> The first is that a thin film of solution must exist between the crystal and the adjacent confining surface in order for the continued deposition of material to occur (Figure 30a).<sup>[391]</sup> The second is that the solution must be supersaturated to allow growth on the loaded face. The degree of supersaturation is proportional to the load on that crystal face.<sup>[365,391,392]</sup>

### 11.2.1. Calculation of the Crystallization Pressure

An expression to calculate the crystallization pressure as a function of the supersaturation was first derived by Correns and Steinborn,<sup>[389]</sup> whose original work has recently been translated and commented upon by Flatt and co-workers.<sup>[393]</sup> This is expressed as

$$\Delta p = \frac{RT}{V_m} \ln S \quad (37)$$

where  $\Delta p = p_c - p_1$  is the crystallization pressure,  $p_c$  is the pressure on the loaded crystal face,  $p_1$  is the ambient pressure,  $R$

is the universal gas constant,  $T$  is the temperature and  $V_m$  is the molar volume. In this derivation, the supersaturation,  $S$ , is defined as a function of the concentrations in the saturated ( $c_0$ ) and supersaturated ( $c$ ) solutions, such that,  $S = c/c_0$ .<sup>[389,390]</sup> This formulation for the crystallization pressure has been adopted by many authors, although the supersaturation has also been defined using activities ( $S = a/a_0$ )<sup>37</sup> and activity products ( $S = K/K_0$ ).<sup>[394]</sup>

A second approach to the problem was taken by Everett, who related the crystallization pressure to the properties of curved interfaces between crystals and their solutions. He investigated the damage caused by frost heave to porous materials and particularly the formation of “ice lenses.”<sup>[395]</sup> When considering a scenario with a large pore adjacent to a small pore, he concluded that the crystal in the larger pore would exert a crystallization pressure since the growth of a crystal in the small pore was not favorable thermodynamically.<sup>[391,395]</sup> The difference in the chemical potentials of these two crystals leads to a pressure difference equivalent to

$$\Delta p = \gamma_{cl} \frac{dA}{dV} \quad (38)$$

where  $\gamma_{cl}$  is the interfacial free energy between the crystal and the liquid,  $V$  is the total volume of the solid, and  $A$  is the area of the interface.<sup>[391,395]</sup> In the case of spherical pores Equation (38) simplifies to

$$\Delta p = 2\gamma_{cl} \left( \frac{1}{r_1} - \frac{1}{r_2} \right) \quad (39)$$

for large and small pores with radii  $r_1$  and  $r_2$ , respectively.<sup>[391,395]</sup>

An expression for the crystallization pressure that is consistent with both of these models was subsequently

developed<sup>[391]</sup> that uses Pitzer's<sup>[396]</sup> ion interaction approach in order to consider the nonideal behavior of the liquid phase. For cases where crystals have sizes greater than 0.1 μm, where curvature effects are negligible, this can be written as<sup>[391]</sup>

$$\Delta p = \frac{\nu RT}{V_m} \left( \ln \frac{m}{m_0} + \ln \frac{\gamma_{\pm}}{\gamma_{\pm,0}} + \frac{v_0}{\nu} \ln \frac{a_w}{a_{w,0}} \right) \quad (40)$$

Here,  $\nu$  corresponds to the total number of ions released when the salt in question completely dissociates and  $v_0$  is the total number of water molecules.  $m$  and  $m_0$  are the molalities of the supersaturation and saturated solutions respectively. The parenthesis can be split into two parts. The first is equivalent to the  $\ln(c/c_0)$  term in Correns and Steinborn's expression,<sup>[389]</sup> but using the molalities ( $m$ ) rather than the concentrations. The second part deals with the nonideal behavior of the salt solution where  $\gamma_{\pm}$  is the mean activity coefficient and  $a_w$  is the activity of water.

This expression was used to calculate the crystallization pressures of supersaturated solutions of aqueous NaCl, NaNO<sub>3</sub>, Na<sub>2</sub>SO<sub>4</sub>, and MgSO<sub>4</sub>,<sup>[391]</sup> where these salts are very common in building materials. Both the anhydrous and hydrated phases for these salts were used for the calculations and it was demonstrated that the crystallization pressures produced at low to moderate supersaturations are sufficient to yield tensile stresses on the pore walls. These stresses far exceed the tensile strength of most building materials. For instance, at supersaturations of 1.2 all of the salts, with the exception of mirabilite, would have significantly larger crystallization pressures than the tensile strength of sandstone ( $\approx 3$  MPa).<sup>[391]</sup>

The importance of considering the nonideal behavior of the liquids on the calculated crystallization pressure is striking. For salts whose activity coefficients increase with increasing confinement, the calculated crystallization pressure is greater than if ideal behavior is assumed (MgSO<sub>4</sub> = 60%, NaCl = 28% and Na<sub>2</sub>SO<sub>4</sub> = 7%).<sup>[391]</sup> Conversely, if the activity coefficients decrease then the calculated crystallization pressure is smaller (NaNO<sub>3</sub> = -10%). For hydrated salts, there is also an error due to the use of the mole fraction of water rather than its activity. The omission of this effect in the original Correns and Steinborn equation<sup>[389]</sup> leads to an error of  $\approx 10$ –30% for these salts. Finally, the most critical issue arises from the failure to consider the number of ions arising from dissociation of a salt. This underestimates the crystallization pressure by a factor of 2 (in 1–1 salts such as NaCl) or 3 (in 1–2 and 2–1 salts such as CaCl<sub>2</sub> and Na<sub>2</sub>SO<sub>4</sub> respectively).

A more general expression that incorporates Everett's<sup>[395]</sup> consideration of the interfacial energy of the crystal–liquid interface and which can be applied to all crystal sizes has also been derived<sup>[392]</sup>

$$\Delta p_i = \frac{\nu RT}{V_m} \ln \left( \ln \frac{m}{m_{\infty}} + \ln \frac{\gamma_{\pm}}{\gamma_{\pm,\infty}} + \frac{v_0}{\nu} \ln \frac{a_w}{a_{w,\infty}} \right) - \gamma_{d,i} \frac{dA_i}{dV} \quad (41)$$

Here the  $\infty$  subscript is used to denote the properties of the saturated solution with respect to an infinitely large reference crystal. It is used to calculate the pressure increase at crystal face  $i$  assuming that the solution between the pore wall and crystal has activity  $a > a_{\infty}$  where  $a_{\infty}$  is the equilibrium activity of an infinitely large reference crystal at ambient pressure.<sup>[392]</sup>

Application of this equation to the crystallization pressure exerted by NaCl crystals with cubic morphologies at various degrees of supersaturation shows that the crystallization pressure increases with crystal size for a given solution molality. Additionally, there is a minimum crystal size required for the onset of the crystallization pressure, which is a function of the crystal solubility.<sup>[392]</sup>

### 11.2.2. Experimental Investigation of Crystallization Pressure

Experiments to directly measure the crystallization pressure exerted by NaCl and KCl have been carried out using a parallel glass plate system in a climate-controlled chamber.<sup>[397]</sup> A rheometer capable of measuring the normal force was placed in contact with the top plate while an inverted microscope imaged the crystal growth between the glass plates from below. As discussed,<sup>[389,391–393]</sup> a thin liquid film is required for the development of crystallization pressure; if no gap exists between the glass plate and the crystal face, then no ions can access the crystal face, and it cannot continue to grow. This phenomenon was investigated by using hydrophilic and hydrophobic glass plates.<sup>[397]</sup> No pressure was recorded using hydrophobic glasses, where these inhibit the formation of a wetting film. Conversely, the hydrophilic glass slides allowed a thin film to form, giving rise to a sizeable crystallization pressure. For both salts, the crystallization pressure increased with increasing salt concentration,<sup>[397]</sup> as expected from theory,<sup>[389,391–393]</sup> and halite (NaCl) exerted a higher crystallization pressure than sylvite (KCl) for a given concentration of salt (Figure 30b).

The latter result can be readily rationalized. In order to maintain a liquid film, repulsive forces must exist between the crystal face and the confining surface. DLVO-type forces (named after Derjaguin–Landau–Verwey–Overbeek) are obvious candidates.<sup>[397]</sup> The disjoining pressure within a film of a given thickness depends on the charge density at the surface, the relative permittivity of the bulk and free space and the Debye screening length with a specific molar concentration of salt.<sup>[397]</sup> The charge density at the surface is affected by the ions present in solution and decreases from 0.12 C m<sup>-2</sup> for NaCl to 0.072 C m<sup>-2</sup> for KCl, thus explaining the lower crystallization pressure recorded for KCl. The disjoining pressure measured in these experiments at a supersaturation of  $\approx 1.5$  is equal to 150 MPa  $\pm$  50, as compared with 135 MPa for the calculated crystallization pressure of Steiger<sup>[31]</sup> at the same supersaturation.<sup>[397]</sup> These results demonstrate that it is entirely possible for a crystal to grow and exert a crystallization pressure large enough to overcome the tensile strength of natural rocks (Figure 30c–h).

Microfluidic devices have also provided an effective means of studying crystallization within channels, and the concomitant development of crystallization pressure. NaCl was precipitated within finite volumes present in channels in a PDMS/glass microfluidic device, and an increase in supersaturation was achieved by allowing controlled evaporation.<sup>[398]</sup> Coupling the experimental data with computational modelling generated an in-depth understanding of stress generation by the growing crystals and showed that this is governed by the supersaturation in the solution film between the crystal and the pore wall



rather than that in the bulk of the droplet. As this is limited by ion transport, the stress generated is less than that expected based on the bulk supersaturation. The growth of halite crystals within PDMS channels in a microfluidic device was also studied using optical microscopy, where the growing crystals deformed the elastic PDMS.<sup>[399]</sup> Changes in the crystal growth were observed at both the NaCl/PDMS and the NaCl/solution interfaces, and the crystal faces adjacent to the PDMS were indented and bounded by a growth rim. The known mechanical properties of PDMS allowed the crystallization pressure to be estimated in this system.

Studies have also been conducted to image the crystal face adjacent to the pore walls during the development of crystallization pressure, where these have shown that the face is not fully in contact with the substrate, but exhibits a growth rim surrounding a hollow core (**Figure 31**).<sup>[400,401]</sup> Reflection interference contrast microscopy was used to study the growth of a calcite crystal in a microfluidic device and to characterize the topography of the crystal surface adjacent to the glass substrate forming the base of the PDMS/glass device.<sup>[401]</sup> Time-resolved analysis revealed the presence of a thin fluid film between the crystal and substrate and demonstrated that this is not uniform in thickness. Confinement then limits mass flux to the growing crystal surface such that a cavity appears in the crystal face adjacent to the substrate where no growth occurs. An outer rim then develops where growth occurs, causing the crystal to be pushed away from the substrate.

### 11.3. Salt Weathering in Porous Materials

Many experiments have been conducted to explore the disintegration of rocks and building materials due to salt crystallization.<sup>[12,361,374,402–405]</sup> These range from the inspection of damage in porous rocks subjected to salt attack,<sup>[361,405]</sup> to the detection of crystallization pressure in situ during rock dilatation.<sup>[364,403]</sup> Of these, the crystallization of NaCl,<sup>[361,397]</sup> sodium sulfate,<sup>[12,403,404]</sup> <sup>[361,406]</sup> and gypsum<sup>[407,374]</sup> have attracted particular attention. Goudie investigated the efficiency of different salts at breaking down rectangular sandstone blocks by submerging the lower part of the sandstone in a salt solution and then subjecting the block to simulated diurnal temperature cycles.<sup>[405]</sup> Damage was then evaluated after 40 and 60 cycles. From the exhaustive list of salts and mixtures of two salts explored, sodium carbonate followed by magnesium sulfate and sodium sulfate were the most effective at rock disintegration, as was a mixture of Na<sub>2</sub>CO<sub>3</sub> and MgSO<sub>4</sub>. These weathering effects were cumulative, with a large portion of damage occurring between the 40th and 60th cycle.

The relative humidity of the environment in which a porous medium is maintained is also an important environmental factor and affects the location of salt crystallization by promoting either efflorescence (surface crystallization) or subflorescence (intraporous crystallization).<sup>[361]</sup> In cases where salts have multiple hydrated forms, the relative humidity can also determine mineral speciation. Crystallization of NaCl and sodium sulfate (mirabilite, Na<sub>2</sub>SO<sub>4</sub>·10H<sub>2</sub>O and thenardite, Na<sub>2</sub>SO<sub>4</sub>) under controlled humidity within a number of microsystems (droplets, capillaries, and stone), and in a macro-scale setup comparable to that of Goudie<sup>[405]</sup> showed that halite

has a preference for efflorescence, while both sodium sulfate phases are prone to subflorescence.<sup>[361]</sup> Halite growth caused little damage to limestone whereas both mirabilite and thenardite produce substantial damage regardless of the relative humidity. As seen in optical microscope and SEM images, halite forms cubic crystals that are characteristic of growth at lower supersaturations.<sup>[408]</sup> This is then consistent with low crystallization pressures and the lack of damage caused by the crystallization of halite in the microporous network.<sup>[361,391]</sup> Halite can therefore only cause significant damage when it is combined with other salts such as gypsum<sup>[402]</sup> or if higher supersaturations can be achieved.

Halite's preference for efflorescence has also been explored using X-ray computed microtomography,<sup>[364,409]</sup> where this technique can be used to perform in situ analysis of crystallization within porous media (**Figure 32**). Precipitation within NaCl-saturated sandstones was studied following a number of wetting-drying cycles, where humidity cycling occurs in many climates, and is often associated with the formation of large crystals and severe damage.<sup>[409]</sup> After initial drying, the stones were brought into contact with either liquid water or water vapor until fully saturated, and they were then dried again at either 20% or 50% relative humidity. These cycles were then repeated. Regardless of the relative humidity, some salt crystals remained after rewetting with water. These then act as nucleation sites for the formation of new crystals in the subsequent evaporation step. Large, cauliflower-like crystal assemblages form at the surface of the stone, where this is attributed to the transport of salt through the porous network of the stone (**Figure 32b**). If the rewetting occurs by deliquescence (water vapor) the drying and recrystallization dynamics are quite different. As this process is slow, a very homogeneous saturated solution permeates through the porous network, transporting salt to the interior of the sandstone sample, where large cubic NaCl crystals form. This demonstrates that halite can exhibit subflorescence under specific conditions.

Sodium sulfate minerals, in contrast, are highly damaging to building materials and natural rocks.<sup>[12,403,404,406]</sup> Although this is often associated with the volume change occurring on hydration of thenardite to mirabilite,<sup>[361]</sup> a more complex picture has emerged involving the build-up of crystallization pressure.<sup>[12,361]</sup> Magnetic resonance imaging (MRI) and optical microscopy of wetting-drying cycles of Na<sub>2</sub>SO<sub>4</sub> saturated sandstones and crystallization within a rectangular glass capillary showed that anhydrous thenardite crystals formed in cycle 1 only partially dissolved upon rewetting in cycle 2.<sup>[12]</sup> As thenardite is more soluble than the hydrated mirabilite phase, their partial dissolution generates a supersaturated solution with respect to mirabilite, and the remaining crystals act as nucleation sites for the subsequent rapid growth of mirabilite. This increase in supersaturation also gives rise to an increase in the crystallization pressure to levels where it exceeds the tensile strength of the sandstone.<sup>[12]</sup>

### 11.4. Model Porous Media

A significant challenge facing studies of crystallization in natural and man-made porous media is the inhomogeneity of their structures, where they can contain combinations of pores

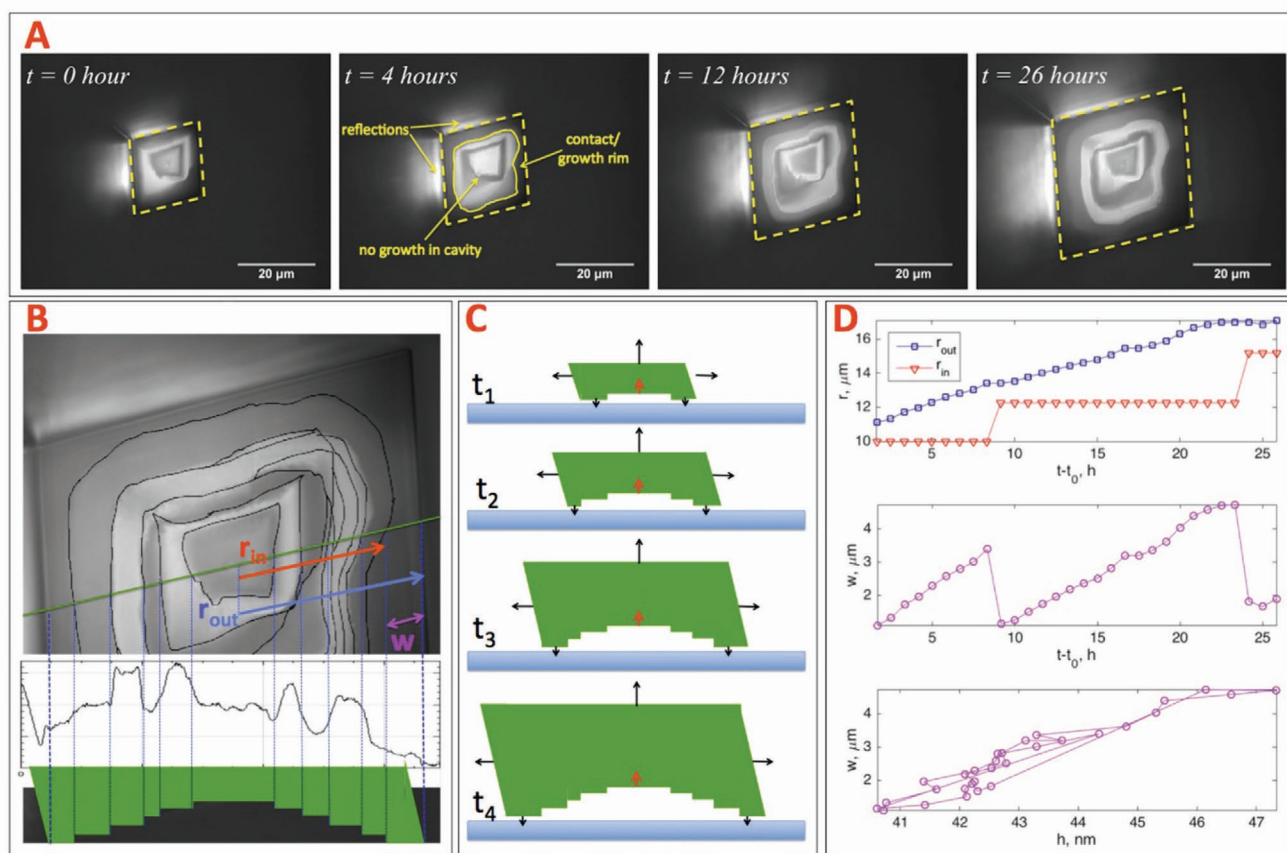
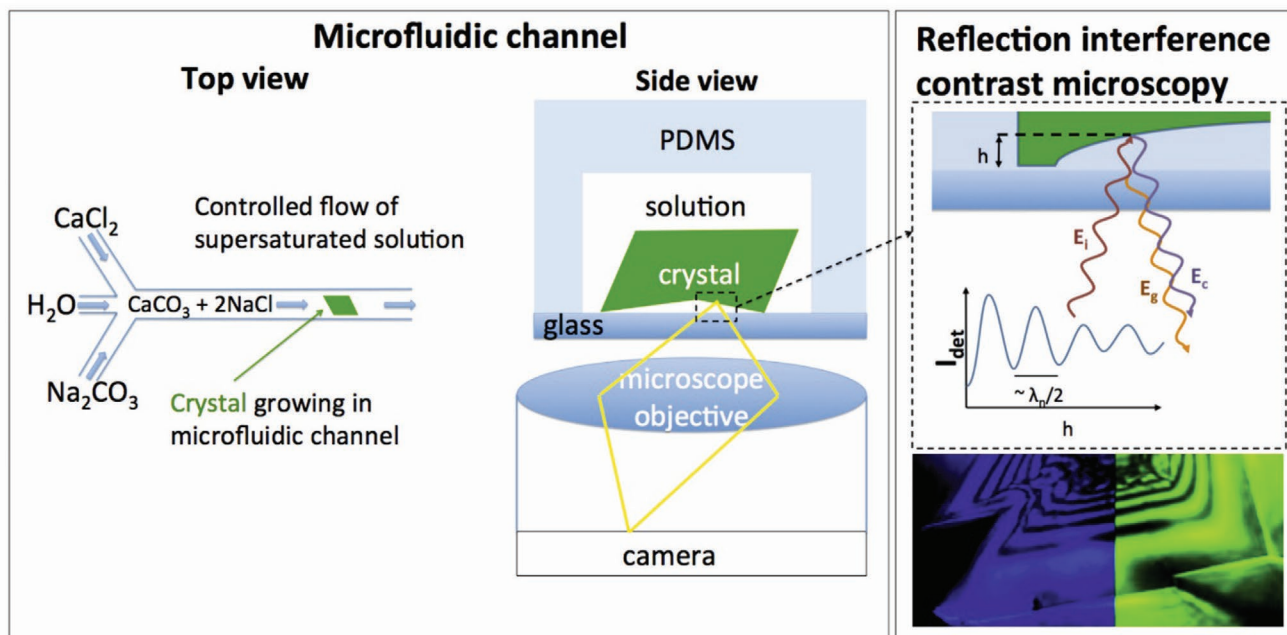


**Figure 31.** Top: diagram of the microfluidic channel and setup on the reflection interference contrast microscopy (RICM). The principle of RICM is illustrated at the top right. The detected intensity is dependent on the height difference between the two interfaces and the wavelength of the light. The use of both blue and green LEDs to illuminate a calcite crystal shows the fringes align near the rim, but differ as the distance increases toward the core. Bottom: A) in situ imaging of crystal growth along the  $10\bar{1}4$  surface of calcite. B) Calculating the height between the crystal and interface as a function of the intensity. C) Interpretation of the growth sequence in (A). D) Top: the radii (inner and outer) as a function of time. Middle: the width of the rim as a function of time. Bottom: the rim width versus the height difference to the glass surface. Top image and (A) to (D): Reproduced with permission.<sup>[401]</sup> Copyright 2012, Elsevier.

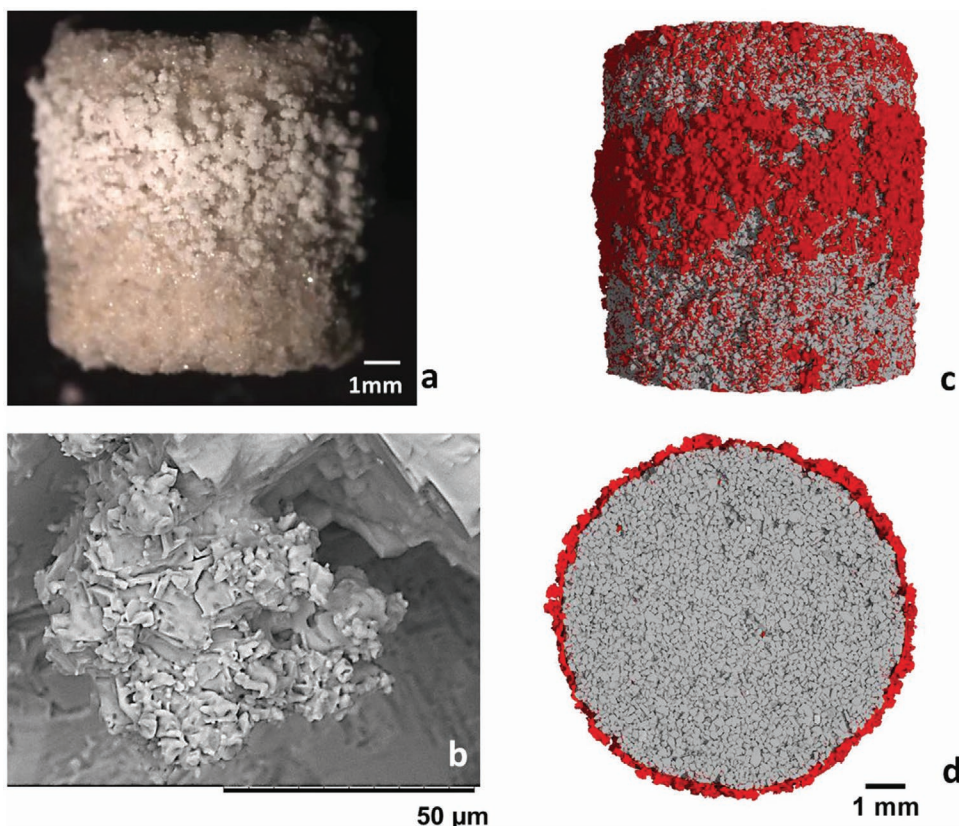


**Figure 32.** Dissolution–drying cycles lead to recrystallization. a) Optical photograph of sample. b) SEM image of the microcrystallites forming cauliflower structures at the surface of the sample. c,d) X-ray computed microtomography highlighting in red the NaCl on the surface and in the middle (core) of the sample. a–d) Reproduced with permission.<sup>[409]</sup> Copyright 2015, American Institute of Physics.

that vary in size across multiple length scales, and diverse interconnectivity. This makes it highly challenging to simulate flow through these media, and to correlate these data with the observed crystallization behavior. A range of model porous media with well-defined structures have therefore been developed, which provide the opportunity for systematic studies.

Packed glass beads provide a convenient model system, where it offers uniformity in structure, optical transparency, and the possibility of modifying the surface chemistry of the beads using silanization.<sup>[367,410–412]</sup> As an example of this approach, magnetic resonance imaging (MRI) and microcomputed X-ray tomography ( $\mu$ -CT) was used to investigate calcium carbonate precipitation within a model porous medium comprising packed 200  $\mu$ m glass beads.<sup>[413]</sup> MRI generate 3D maps of flow through the porous medium, while  $\mu$ -CT should be used to visualize the growing crystals in 3D. In combination, these techniques can provide a powerful means of characterizing precipitation reactions in porous media.  $\mu$ -CT was also used to study barium sulfate precipitation within packed glass beads.<sup>[412]</sup> Measurement of the growth rate as a function of time suggested that the rate was comparable to that on free surfaces provided that the growth is not transport limited and that the rate is normalized with respect to the surface area of the crystals.

An array of glass beads was also used to study the dissolution and recrystallization behavior of NaCl crystals within porous media (Figure 33). A model system was constructed in

which single crystals of NaCl were entrapped within a close-packed array of 230  $\mu$ m glass beads within a narrow flat capillary (Figure 33a).<sup>[411]</sup> The filled capillary was then sintered and one end was sealed. This design therefore enables the initial size and positioning of the halite crystals to be controlled, and the beads can be treated to change the surface chemistry from hydrophilic to hydrophobic. Deliquescence was studied by maintaining the capillaries at a controlled relative humidity RH greater than the equilibrium relative humidity above a saturated NaCl solution, and the process of water infiltration was studied using optical microscopy. With hydrophilic surfaces, water started to form around the NaCl crystals, causing them to start to dissolve. Solution then entered the neighboring pores, invading the small pores first and leading to full dissolution of the crystals. These samples were then exposed to low humidity levels. Drying occurred first in the large pores, and then continued to yield multiple small crystallites in the small pores. A different pattern of behavior was observed with the hydrophobic beads. There, solution preferentially entered the large pores and the subsequent drying cycle started in the small pores. In this system, crystals then form in the large pores where they were originally located.

A related model was also created by forming a packed column of controlled pore glass (CPG) beads.<sup>[385]</sup> This generates a system with a bimodal pore size distribution corresponding to the nanopores within the beads, and macropores

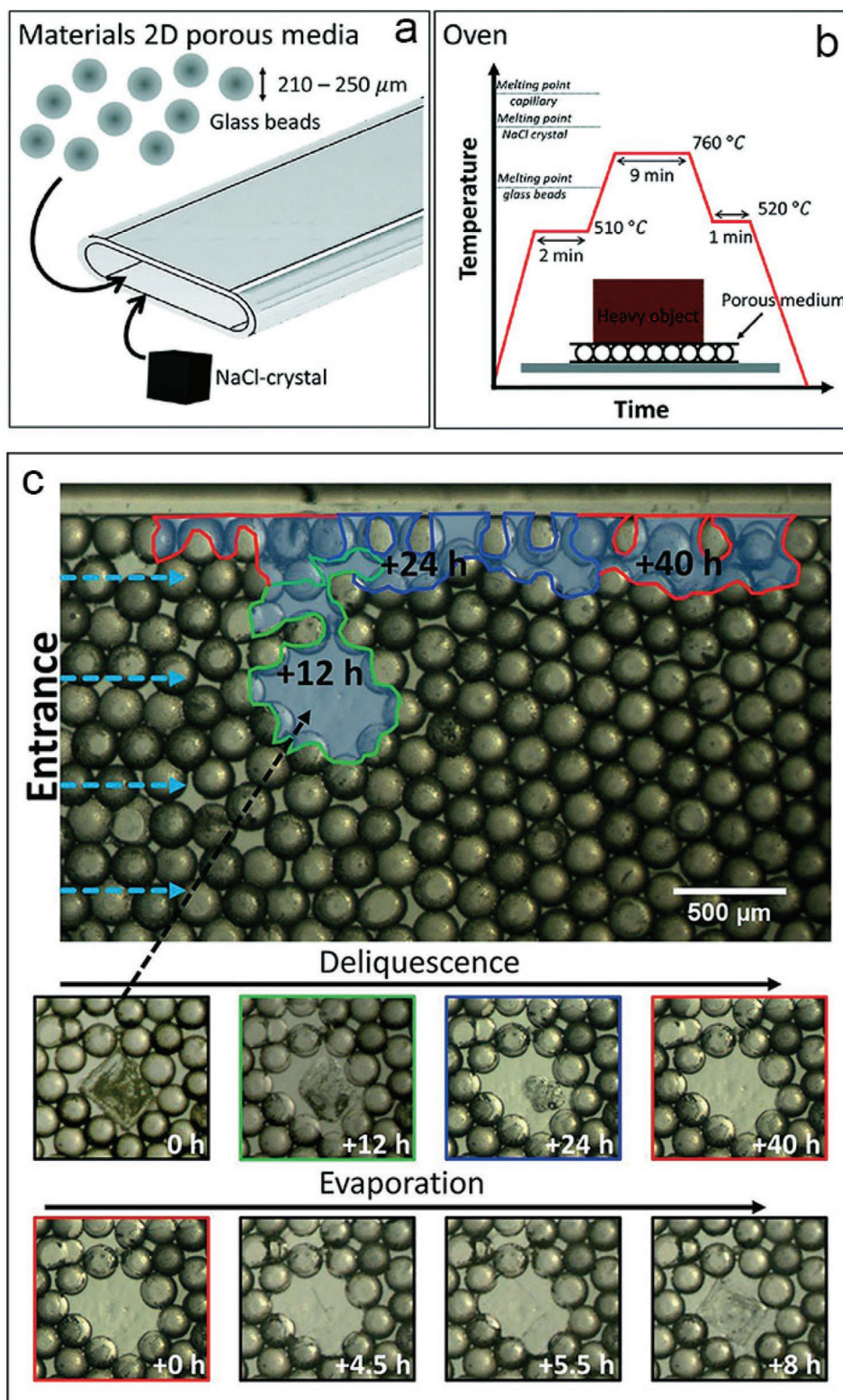


**Figure 33.** a) A model porous medium was formed by filling a rectangular capillary with a monolayer of glass beads, together with a single NaCl crystal. b) Schematic of the process used to anneal the sample and achieve contact between the beads and both sides of the capillary. c) Optical microscopy images of a hydrophobic 2D porous medium after deliquescence. The areas marked in green, blue and red represent the evolution of the liquid clusters after 12, 24, and 40 h. The images below show the crystal during the deliquescence (first row) and evaporation (second row) processes. a–c) Reproduced with permission.<sup>[41]</sup> Copyright 2018, Royal Society of Chemistry.

between the beads. X-ray scattering measurements, modeling, and electron microscopies were used to study the kinetics of calcium carbonate precipitation within these environments, where CPGs were employed in their native state, and functionalized with self-assembled monolayers with anhydride terminal groups. Precipitation only occurred in the macropores in the native CPG columns, while calcium carbonate precipitated both within the nanopores and the macropores when the CPGs had been functionalized. The failure of calcium carbonate to precipitate within the nanopores in the native CPGs was proposed to arise from unequal concentrations of calcium and carbonate ions within the nanopores, where these could be act as chemically selective membranes under the solution conditions.

An additional way of studying crystallization within model porous media is the construction of micromodels, where these are fabricated to represent a network of interconnected pores in the 10–100  $\mu\text{m}$  size regime.<sup>[414–417]</sup> These network models have been extensively used to study fluid flows in porous media,<sup>[417]</sup> but can also be fabricated to facilitate experimental analysis of crystallization. Kim et al. used microfabrication techniques to fabricate optically transparent microfluidic devices containing: i) single straight channels with isolated pores, ii) a regular grid-like network of microchannels, and iii) channels mimicking native porous media.<sup>[416]</sup> NaCl precipitation was studied within these devices under conditions relevant to  $\text{CO}_2$  sequestration in saline aquifers, where  $\text{CO}_2$  and brine were flowed through the microfluidic networks, and the flow, pH, and NaCl precipitation monitored using optical and fluorescence microscopy. Two principal forms of salt crystals were observed, where large crystals formed at early times within the NaCl solution, and polycrystalline aggregates developed later in the evaporation process. These two forms of salt deposits acted together to block pores and reduce the potential carbon storage capacity.

Although used to study calcium carbonate dissolution under conditions relevant to oil/gas recovery and  $\text{CO}_2$  sequestration, it is also worth highlighting a rather elegant approach used by Song et al. to create a micromodel etched into the surface of a calcite ( $\text{CaCO}_3$ ) crystal.<sup>[414]</sup> A thick section was cut from a large calcite crystal, and its surface was coated with a thin layer of beeswax. The desired network pattern was then etched into the wax using a laser cutter, and the surface was exposed to HCl to etch the pattern into the calcite. The wax was then removed, inlet and outlet holes were drilled, and the cleaned surface was bonded to a glass slide. This effectively generated a microfluidic device in the surface of the crystal, where the transparency of the calcite substrate is such that dissolution, or the growth of new material, can be studied using optical microscopy.

## 12. Crystallization of Colloidal Particles in Confinement

It is well-recognized that colloidal particles with narrow size distributions can self-assemble into crystalline arrays under appropriate solution conditions.<sup>[418]</sup> With the ability to perform in situ analysis of the assembly of sub-micrometer particles using techniques such as confocal fluorescence microscopy, these systems are widely used as analogues of atomic and molecular crystals, and provide unique insight into colloidal

interactions.<sup>[419–421]</sup> That methods of nanoparticle synthesis have now evolved to the point where many can be produced with very narrow size distributions has also opened the door to the crystallization of these species into superlattices, with the promise of generating new materials.<sup>[422,423]</sup> Confined systems have been explored as a method of controlling this assembly process. Encapsulation of nanoparticles within emulsions, and extraction/loss of the internal solvent can lead to the formation of supercrystals with uniform sizes and shapes, and a range of structures have been observed.<sup>[423–426]</sup> Microfluidic devices have also been used to screen for optimal evaporation-driven or destabilization-driven (addition of a suitable precipitant) conditions for the assembly of nanoparticles.<sup>[427,428]</sup>

The behavior of colloidal particles in solution attracts considerable attention, as these provide a model of many complex fluids of great practical importance. These systems have been extensively treated by both theory and experiment, where individual micrometer-scale particles can be readily imaged using optical microscopy techniques, and their motion followed in real-time.<sup>[429–431]</sup> The assembly of spheres into condensed phases also offers unique insight into the formation of many structures in nature including ionic and molecular crystals. While the face-centered cubic (FCC) structure is the optimal packing for an infinite number of spheres, finite numbers of spheres can exhibit a range of structures that are not consistent with FCC packing.<sup>[432]</sup> Finite-size effects originating from confined geometries also make the picture more complex and can give rise to different packings.<sup>[433,434]</sup>

### 12.2. Crystallization between Parallel Plates or Wedge

The effects of confinement on the crystallization of colloidal particles have been investigated experimentally by studying the assembly of micrometer-scale polymer particles between parallel plates or in a wedge geometry,<sup>[433,435]</sup> where these studies show that the structure of the colloidal crystal builds from a monolayer to multilayers of 2D crystalline layers with increasing dimensions of the confining system. The wedge geometry in particular allows the effects of extreme confinement to be investigated, where this is defined as being in the order of the diameter of a single sphere.

Optical microscopy studies of the crystallization of polystyrene spheres between glass surfaces have revealed a structural evolution with increasing surface separation from a monolayer with triangular symmetry (symbolized as  $\Delta$ ), to a bilayer comprising stacked square layers (symbolized as  $\square$ ).<sup>[435]</sup> The full progression of structures was described as

$$n\Delta \rightarrow (n+1)\square \rightarrow (n+1)\Delta \dots, \quad \text{where } n = 1, 2, 3, \dots$$

This sequence can be rationalized by considering how the spheres can achieve optimal packing density,  $\Phi$ , in the confined volume.<sup>[433,436]</sup> The first monolayer exhibits hexagonal packing as this is more efficient than the packing in the square layer. With increasing separation of the surfaces, the colloidal crystal alternates in structure between triangular and square symmetries. Two competing factors govern the crystal packing adopted for a given surface separation: the height of  $n$  square layers is smaller than that of  $n$  triangular layers, while the

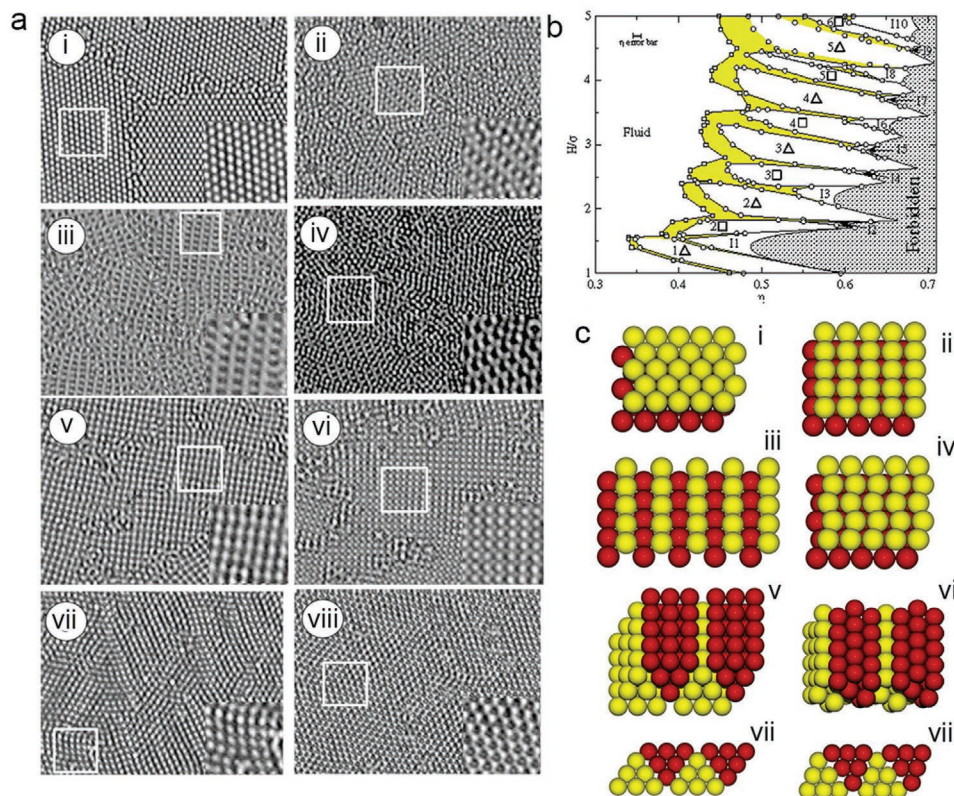


**Figure 34.** a) Images of structures taken for the equilibrated colloids sample at the transition from a monolayer to a bilayer; image width ( $47.2 \times 35.4$ )  $\mu\text{m}^2$ . The white squares indicate the position of the fourfold enlargements shown bottom right in the images. The following structures are observed with increased plate separation: i)  $1\Delta$ ; ii–iv) B; v,vi)  $2\Box$ ; vii)  $2R\Delta$ ; viii)  $2\Delta$ . B is a buckled phase and R is a rhombic phase. a) Reproduced with permission.<sup>[437]</sup> Copyright 2005, IOP Publishing. b) The equilibrium phase diagram of hard spheres with diameter  $\sigma$  confined between two parallel hard walls with plate separation  $H$ : packing fraction  $\eta$  representation. The white, shaded (yellow) and dotted regions indicate the stable one-phase region, the two-phase coexistence region, and the forbidden region, respectively. c) Stable solid structures of confined hard spheres. i) The triangular phase  $2\Delta$ . ii) The square phase  $2\Box$ . iii) The buckling phase  $2B$ . iv) The rhombic phase  $2R$ . v,vi) The prism phase with square symmetry  $3P\Box$ . vi,viii) The prism phase with triangular symmetry  $3P\Delta$ . In (i)–(vi), the point of view is at an angle of  $30^\circ$  to the  $z$  direction. In (vii) and (viii), the point of view is at an angle of  $90^\circ$ . Different colors indicate particles in different planes ((i)–(iv)), or particles belonging to different prism structures ((v)–(viii)). b,c) Reproduced with permission.<sup>[436]</sup> Copyright 2006, IOP Publishing.

triangular layers pack more efficiently than the square layers. As  $\Phi$  decreases when the layers do not fully fill the confining volume, the square stack is the first to fit between the wall, and is replaced by the triangular stack as the surface separation increases in order to preserve a high  $\Phi$ .<sup>[433]</sup>

Further detailed experimental investigation of this phenomenon reveals that the evolution in structure of this system is actually rather more complex and that a large number of intermediate phases can form between the defined phases described above (Figure 34).<sup>[433,437]</sup> These are generated when the available gap falls between that required for the sequential structures, which gives rise to an increase in the packing density. A range of intermediate structures form according to the number of layers present, including buckled, prism, and rhombic phases (Figure 34c). This behavior has also been rationalized using simulations of the behavior of high densities of colloidal particles between parallel plates with separations between 1 and 5 sphere diameters.<sup>[436]</sup> The existence of 26 thermodynamically stable crystal structures was demonstrated, which is in good agreement with the experimental data (Figure 34a,b). These calculations also revealed that a high density of particles undergo

freezing and melting transitions as the separations of the confining surfaces are changed.

## 12.2. Crystallization within Evaporating Droplets

A fundamentally different approach was used to study the assembly of small numbers of colloidal spheres in spherical confinement.<sup>[432]</sup> Clusters of polymer spheres were generated by creating oil droplets in water in which a defined number ( $n$ ) of micrometer-sized spheres are strongly bound at the droplet surface by surface tension. On evaporation of the oil the spheres are brought closer together on the droplet surface until a mechanically stable intermediate is generated when the spheres touch. Removal of further oil then causes the droplet to distort, giving rise to capillary forces that cause the spheres to rearrange. As the final oil is removed the spheres de-swell and van der Waals attractions increase, causing the particles to pack together in a cluster of a defined number of spheres.

Each cluster containing the same number of spheres exhibits identical structures, with small clusters showing

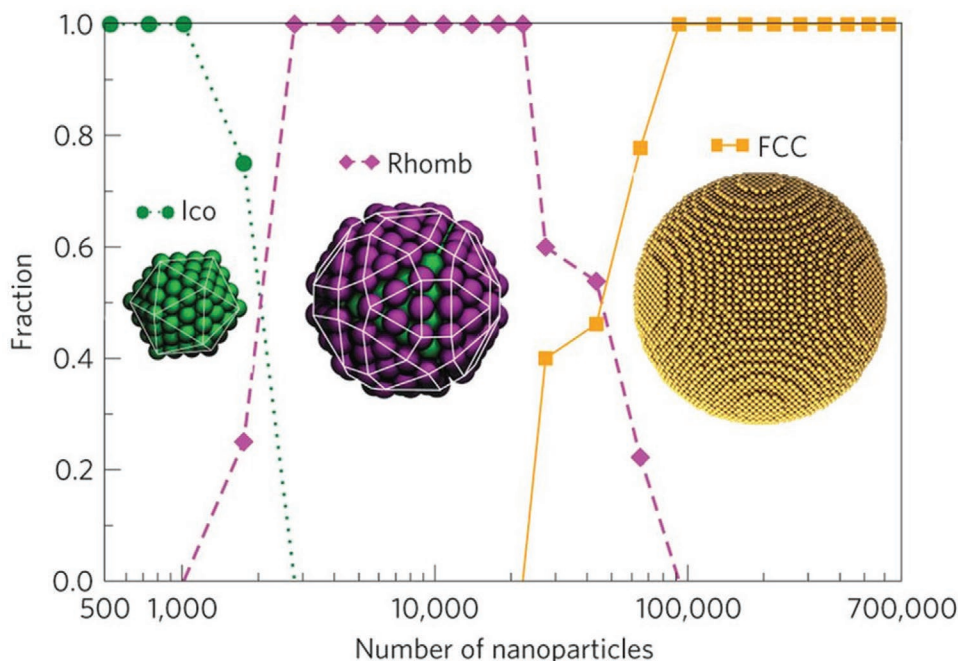


**Figure 35.** Size dependence of the cluster structure. Structural transition from a Mackay icosahedron (Ico) to an anti-Mackay rhombicosidodecahedron (Rhomb) to a face-centered cubic (FCC) cluster, as observed for supraparticles consisting of nanoparticles. The fraction of structures, based on 121 supraparticles, is plotted as a function of the number of nanoparticles per supraparticle. 14 icosahedra, 63 rhombicosidodecahedra, and 44 FCC clusters were observed. Reproduced with permission.<sup>[426]</sup> Copyright 2015, Springer Nature.

triangular ( $n = 3$ ), tetrahedral ( $n = 4$ ), triangular bipyramidal ( $n = 5$ ), and octahedral ( $n = 6$ ) morphologies, all of which are elements of an FCC lattice. Larger clusters containing between 7 and 10 spheres exhibited unusual structures, termed convex deltahedra, that cannot be broken down into regular tetrahedra or octahedra, and which cannot be close-packed to fill space. These structures cannot be attributed to a minimization of potential energy or volume, but instead correspond to a minimization of the second moment of the mass distribution (a measure of optimal packing). The structures of these clusters are therefore be considered to originate from the collapse of the shells of spheres on the surface of the droplets.

A similar methodology has been used to investigate the structure adopted by nanoparticles in spherical confinement.<sup>[424–426]</sup> 6 nm gold nanoparticles functionalized with dodecanethiol were dispersed in surfactant-stabilized oil/water emulsions, and the oil phase was slowly evaporated.<sup>[425]</sup> Supraparticles of up to  $\approx 100$  nm in size were formed and exhibited decahedral and icosahedral morphologies. In situ analysis of their formation using surface plasmon spectroscopy and small angle X-ray scattering (SAXS) demonstrated that these structures were not templated by the droplet surface, suggesting instead that the formation of these geometries is driven by free energy minimization.

The assembly of large numbers of particles under spherical confinement has also been studied.<sup>[426]</sup> Up to 100 000 particles were suspended in oil-in-water droplets, and the oil was then slowly evaporated to induce assembly. Particles that fell into two size regimes were employed: cobalt iron oxide nanoparticles with a core diameter of 6.0 nm and a shell of oleic acid, core/shell semiconductor particles with diameters of 12 nm and

1.3  $\mu\text{m}$  fluorescently labeled core/shell silica particles. These were assembled into supraparticles with diameters of between 75 and 785 nm, and their internal structures were determined using electron tomography for the nanoparticles,<sup>[438]</sup> and confocal fluorescence microscopy for the micrometer-sized particles. The supraparticles exhibited different structures according to their size, and those generated from nanoparticles were almost invariably crystalline (Figure 35). Supraparticles containing up to 1000 particles exhibited icosahedral morphologies, with twelve vertices and twenty triangular (111) faces on the surface. These structures can be regarded as multiply-twinned crystals with 5-fold symmetry. An increase in the number of particles to between 1000 and 3000 led to the formation of supraparticles with rhombicosidodecahedral morphologies comprising 12 pentagonal faces, 20 triangular faces, and 30 rectangular faces. Finally, a transition to a purely FCC structure occurred between 25 000 and 90 000 particles. The supraparticles formed from the colloids were only partially ordered and adopted either of the icosahedral forms. The FCC structure was not observed, potentially due to the effects of gravitational sedimentation of the larger particles.

Icosahedral symmetries are found in many systems including short-range structures in liquids and clusters of some atoms and metals.<sup>[439–441]</sup> A basic icosahedron comprises a central particle surrounded by a further 12 particles and can be considered as 20 tetrahedra sharing a common vertex. This structure minimizes short-range (Lennard–Jones) type attractions and is entropically favored, but is non space-filling so does not provide a building block for bulk crystals. The importance of the icosahedron in structural chemistry was first recognized by Mackay,<sup>[442]</sup> who described its relationship with

CCP structures. Addition of further concentric shells of atoms to the icosahedral unit following FCC packing leads to larger icosahedra whose faces show FCC (111) packing. The cluster of 55 atoms (2 concentric shells) is particularly common and is termed the Mackay icosahedron.<sup>[439,442]</sup> Addition of atoms to the (111) faces can also occur by HCP packing. This anti-Mackay overgrowth corresponds to a packing fault and generates a hierarchical structure. Both structures therefore originate from the same icosahedral core, but have different surface terminations. The smaller clusters formed correspond to Mackay icosahedra, while the larger rhombicosidodecahedra are anti-Mackay clusters.

Molecular dynamics simulations of the behavior of hard spheres (which have zero interaction energy unless they come into contact) in shrinking spherical confinement gave excellent agreement with the experimental data, supporting the observation that the structures formed were not specific to the particle type. This provides strong evidence that the formation of these icosahedral structure is entropy-driven. Simulations were also performed to investigate the evolution in structure of the supraparticles. Consideration of 16 000 hard spheres in spherical confinement showed that crystallization starts at the surface of the particles, forming two to three ordered layers. Crystallization then proceeds inward, and as the interior crystallizes the surface becomes less ordered. Finally, the interior completely crystallizes and the tetrahedral units that are components of the Mackay icosahedron.

The shape of the particles also dictates how they assemble under spherical confinement.<sup>[434,443]</sup> Oleic acid functionalized magnetite ( $\text{Fe}_3\text{O}_4$ ) nanocubes with sharp edges (size 23 nm) and  $\text{Fe}_x\text{O}/\text{CoFe}_2\text{O}_4$  nanocubes with rounded edges (10 nm) were assembled within shrinking emulsion droplets.<sup>[443]</sup> The sharp nanocubes assembled as a simple cubic lattice in the core of the supraparticles, and were aligned with their flat faces parallel to its surface. The rounded nanoparticles, in contrast, assemble to form a supraparticle whose core exhibits Mackay icosahedral symmetry, while particles located on the surface form a defect-rich hexagonal array. Simulations supported these observations and revealed a change in structure from HCP or FCC packing for rounded particles, to a structure comprising wedges of HCP/FCC and cubic-packed particles as the edges of the particles become sharper, to wedges with cubic symmetry and finally a cubic core surrounded by spherical shells. The competing effects of flat faces tending to align the particles and sharp corners acting to separate the particles contribute to the formation of these different structures.

Further investigation into the influence of particle shapes on their assembly was performed by running Monte Carlo Simulations of the assembly of up to 60 particles of the Platonic solids (the tetrahedron, cube, octahedron, dodecahedron, and icosahedron) in spherical confinement.<sup>[434]</sup> A wide range of structures were observed, and for many values of  $N$  (the number of constituent particles) the icosahedra and dodecahedra pack into clusters comparable to those formed from the same number of spheres. The clusters formed from cubes and octahedra also resembled the clusters of spheres for some values of  $N$ , while no such relationship was found for tetrahedral particles. In contrast to packing in bulk solids where the particle morphology determines the packing geometry, this

influence is significantly reduced in spherical confinement. The simulations also show that certain numbers of particles—termed “magic numbers”—give rise to clusters with high densities, but that these can exhibit different structures according to the shape of the particles. These results highlight the possibility of combining confinement effects with different particle morphologies to generate clusters with a wide range of structures.

### 13. Summary and Perspective

This article provides a review of crystallization in confined volumes, where we demonstrate that confinement can influence virtually every aspect of crystal nucleation and growth. Information is dispersed across the literature in relation to fields as diverse as ice nucleation, biomineralization, nucleation kinetics, nanomaterial synthesis, pharmaceuticals, and geochemistry, where each of these has a somewhat different focus. For example, studies of ice nucleation address the freezing of water in nanopores, where this has relevance to ice nucleation in the atmosphere, while arrays of droplets offer multiple identical, impurity-free environments, and are invaluable for studying nucleation kinetics. Crystallization in porous media lies at the heart of geochemical phenomena such as weathering and the formation of ore deposits. Together, this body of literature shows how confinement affects the crystallization of different substances in environments with different length scales and geometries.

Significant effects can be observed on crystal nucleation and growth. Growth within a constrained volume can limit the growth of a crystal such that its morphology is defined by the environment. This can yield complex 3D morphologies that could not be formed using conventional additive-based approaches. Similarly, competitive growth of crystals with anisotropic structures within anisotropic environments lead to strong orientation effects. Crystals within porous media can also continue to grow even when they have filled the pore when a thin fluid film is present between the crystal and substrate. This leads to the development of a crystallization pressure.

Perhaps the most fascinating effects occur at nucleation, however. An influence on nucleation is easily rationalized within environments that have dimensions comparable to the size of a critical nucleus (typically a few nanometers). Thus, crystallization within carbon nanotubes can generate crystals with distorted lattices, structures not seen under analogous bulk conditions, and even new crystal phases. Many organic compounds form as amorphous rather than crystalline phases within very small pores, and polymorph selectivity may occur when the confining environment can only accommodate critical nuclei of certain polymorphs. Polymorph selectivity can also be observed within finite volumes that contain just enough ions to form a critical nucleus, due to the different solubilities of different polymorphs.

Interestingly, strong effects on nucleation are also seen at length scales far larger than a critical nucleus. Significant stabilization of metastable polymorphs is commonly observed, and increases with increased confinement. This effect is predominantly kinetic in origin and has been attributed to reduced



diffusion rates within small pores, and the formation of very high supersaturations. The surface chemistry of the confining medium may also play a role in selecting polymorph, where it may directly favor one polymorph over another, or influence the ionic composition within a nanopore. Once formed, metastable polymorphs would also be expected to be slow to transform due to the reduced nucleation rates associated with small volumes.

Finally, vastly reduced nucleation rates are observed in small volumes, where this has been attributed to a number of effects including the reduced probability of nucleation in small volumes, and the elimination of the impurities that promote nucleation in bulk solution. Notably, these effects even operate in droplets that are hundreds of micrometers in diameter. The consumption of ions that accompanies the formation of a crystal nucleus within a small, finite volume also gives rise to a continuous depletion of the supersaturation, and thus the driving force for nucleation.

This range of effects demonstrates the scale of the challenge of understanding crystallization in natural environments such as porous rocks and building materials, where these often present pores ranging from the nanometer- to the macroscale and possess a wide range of interconnectivities and even chemical compositions. Crystallization within porous media is also intimately linked to flow through the network, where the system is dynamic and evolves with time as growing crystals begin to block pores and change the interconnectivity. Significant efforts are therefore being made to develop reactive transport models that can describe the dynamic behavior of large-scale systems.<sup>[444,445]</sup> These need to be supported by experimental data obtained from in situ characterization to evaluate the relationship between flow profiles and crystallization.

The technique of X-ray tomography is well-suited to the study of crystallization in situ within natural stones and model porous systems.<sup>[370,412]</sup> However, resolution is generally limited to around the micrometer level such that it is impossible to simultaneously investigate the role played by nanopores and macropores. Electron tomography, in contrast, has the resolution to characterize nanoscale pores but can only be performed on thin slices of material such that macropores cannot be studied.<sup>[446–448]</sup> It is also currently not possible to perform time-resolved studies of crystal nucleation and growth. It is envisaged that the development of cutting-edge imaging techniques such as X-ray ptychography, which can currently achieve resolutions of tens of nanometers, be used to study relatively large specimens and even be coupled with spectroscopy techniques,<sup>[449–451]</sup> may ultimately be able to address this problem.

Well-defined model systems are therefore invaluable in studying confinement effects on crystallization. These ideally possess well-defined geometries and it should be possible to systematically change the dimensions. A limiting factor is again the ability to characterize the system, and ideally perform time-resolved, in situ analysis. However, this is somewhat more straightforward in a well-defined system, where microscopy-based techniques can be selected to target the particular length scale under investigation. Well-defined, uniform environments are also well-suited to time-resolved spectroscopic studies, where methods such as “Classic” NMR could be used to simultaneously study the evolution of both the liquid and solid

phases.<sup>[452,453]</sup> It is also expected that the continued development of cutting-edge methods such as liquid-phase TEM<sup>[454,455]</sup> will ultimately make it possible to study the process of crystal nucleation and growth in situ in nanoscale environments.

A significant barrier to understanding confinement effects in nanoscale volumes is the lack of knowledge of the distribution of ions within small pores, and how this is governed by the surface chemistry. While this could be expected to have a significant effect on nucleation—and may be the origin of some of the observed size-dependent changes in polymorph—this cannot be determined experimentally, and therefore relies on theoretical prediction. It is also well-recognized that liquids are typically more ordered adjacent to a surface than in bulk,<sup>[456–459]</sup> where this structure is maintained for a few molecular layers before rapidly decaying to the bulk structure.<sup>[460]</sup> A substantial portion of the liquid in pores with diameters of a few nanometers, or surfaces separated by a few nanometers would therefore exhibit a different structure from the bulk. This may again influence crystal nucleation and growth. Techniques such as NMR or neutron scattering have been used to analyze the structure of liquids and solids in nanoporous glasses,<sup>[43]</sup> and could potentially be employed to further probe the relationship between the surface chemistry of the confining media, the structure of the confined liquid and the structure of the product crystal.

Further recognizing the important role played by surfaces in directing crystal nucleation, it is well-known that solid state organic thin films often exhibit crystal structures that differ from those of the corresponding bulk materials.<sup>[459]</sup> Illustrating with the important, and much-studied organic semiconductor pentacene,<sup>[461–463]</sup> this compound has five recognized polymorphs that comprise layers of molecules packed in a herringbone arrangement. In the bulk crystal structure the individual molecules are tilted within the layers. In contrast, thin films with thicknesses of under 100 nm that have been vapor-deposited on substrates including amorphous silica and various polymers exhibit an alternative polymorph in which the molecules only exhibit a small tilt. In contrast, the molecules in monolayers of pentacene lie perpendicular to the substrate.<sup>[464]</sup> Molecular dynamics simulations suggest that formation of this new polymorph is governed by the intralayer molecular interactions rather than interactions of the pentacene molecules with the substrate.<sup>[465]</sup> This raises the interesting possibility that similar effects may give rise to changes in polymorph in confined systems exhibiting large surface to volume ratios.

It is also difficult to determine where nucleation occurs within nanopores. While one might assume that the nucleation barrier is reduced on the pore wall, it is noted that crystallization within porous/confined media is often associated with the presence of a fluid layer between the crystal and the adjacent substrate. This has been clearly demonstrated both in micrometer-scale pores in relation to the development of crystallization pressure,<sup>[365,389,397]</sup> and also in nanopores in association with studies of melting/freezing phenomena.<sup>[56,58,64–67]</sup> However, little is known about the crystal/substrate interface for crystals grown from solution in small volumes. This raises questions about whether nucleation is homogeneous or heterogeneous in these systems, or indeed whether crystals can nucleate on a substrate without full displacement of bound water molecules.

The development of a superior understanding of the effects of confinement on crystallization will ultimately enable us to control and profit from this phenomenon. The weathering and decay of rocks and construction materials could potentially be reduced by treating their surfaces to eliminate the fluid layer lying between the crystal and pore wall. This will prevent further crystal growth and a concomitant build-up of stress. It may facilitate the development of strategies to promote crystallization within porous media for contaminant sequestration and remediation,<sup>[350]</sup> and could be used to screen for polymorphs or generate pharmaceuticals in an amorphous form. An understanding of confinement effects is also essential when using liquid-phase TEM, where crystallization within this confined flow cell is expected to be modified as compared with bulk solution.<sup>[348]</sup> An appreciation of confinement effects also allows us to view processes such as biomineralization—which invariably occur within constrained volumes—from a different perspective. While the lion's share of attention has focused on the role of soluble organic additives and insoluble matrices in directing features including the crystal polymorph, morphology, and orientation,<sup>[16]</sup> it is clear that confinement may also play a major role in controlling mineralization. Finally, studying crystallization in confinement may also afford us the opportunity to gain a superior understanding of crystal nucleation, where the extremely high surface/volume ratios of nanoporous media offers a unique chance to investigate the interaction between the crystal and substrate.

## Acknowledgements

The authors acknowledge the European Research Council (ERC) under the project DYNAMIN, grant agreement number 788968, and the Engineering and Physical Sciences Research Council (EPSRC) Programme Grant (grant EP/R018820/1) which funds the Crystallization in the Real World consortium (FCM and CO), an EPSRC Platform Grant EP/N002423/1 (FCM).

## Conflict of Interest

The authors declare no conflict of interest.

## Keywords

biomineralization, colloidal crystallization, geochemistry, porous media

Received: February 14, 2020

Revised: March 26, 2020

Published online: June 25, 2020

- [1] J. J. De Yoreo, P. Gilbert, N. Sommerdijk, R. L. Penn, S. Whitlam, D. Joester, H. Z. Zhang, J. D. Rimer, A. Navrotsky, J. F. Banfield, A. F. Wallace, F. M. Michel, F. C. Meldrum, H. Colfen, P. M. Dove, *Science* **2015**, 349, aaa6760.
- [2] X. C. Ye, M. R. Jones, L. B. Frechette, Q. Chen, A. S. Powers, P. Ercius, G. Dunn, G. M. Rotskoff, S. C. Nguyen, V. P. Adiga, A. Zettl, E. Rabani, P. L. Geissler, A. P. Alivisatos, *Science* **2016**, 354, 874.

- [3] A. E. S. Van Driessche, T. M. Stawski, M. Kellermeier, *Chem. Geol.* **2019**, 530, 119274.
- [4] M. Jehannin, A. Rao, H. Colfen, *J. Am. Chem. Soc.* **2019**, 141, 10120.
- [5] D. Gebauer, S. E. Wolf, *J. Am. Chem. Soc.* **2019**, 141, 4490.
- [6] M. J. Van Vleet, T. T. Weng, X. Y. Li, J. R. Schmidt, *Chem. Rev.* **2018**, 118, 3681.
- [7] A. G. Shtukenberg, M. D. Ward, B. Kahr, *Chem. Rev.* **2017**, 117, 14042.
- [8] R. Deshmukh, M. Niederberger, *Chem. - Eur. J.* **2017**, 23, 8542.
- [9] H. Ping, H. Xie, Z. Y. Fu, *J. Materiomics* **2017**, 3, 83.
- [10] J. Lee, J. Yang, S. G. Kwon, T. Hyeon, *Nat. Rev. Mater.* **2016**, 1, 16034.
- [11] R. M. Espinosa-Marzal, G. W. Scherer, *Acc. Chem. Res.* **2010**, 43, 897.
- [12] N. Shahidzadeh-Bonn, J. Desarnaud, F. Bertrand, X. Chateau, D. Bonn, *Phys. Rev. E* **2010**, 81, 066110.
- [13] I. C. Bourg, L. E. Beckingham, D. J. DePaolo, *Environ. Sci. Technol.* **2015**, 49, 10265.
- [14] Y. F. Liang, S. Tsuji, J. H. Jia, T. Tsuji, T. Matsuoka, *Acc. Chem. Res.* **2017**, 50, 1530.
- [15] E. Ruiz-Agudo, C. V. Putnis, A. Putnis, *Chem. Geol.* **2014**, 383, 132.
- [16] S. Mann, *Biomineralization, Principles and Concepts in Bioinorganic Materials Chemistry*, Oxford University Press, Oxford, UK **2001**.
- [17] E. Beniash, J. Aizenberg, L. Addadi, S. Weiner, *Proc. R. Soc. London, Ser. B* **1997**, 264, 461.
- [18] M. J. Olszta, X. G. Cheng, S. S. Jee, R. Kumar, Y. Y. Kim, M. J. Kaufman, E. P. Douglas, L. B. Gower, *Mater. Sci. Eng., R* **2007**, 58, 77.
- [19] A. Komeili, *FEMS Microbiol. Rev.* **2012**, 36, 232.
- [20] F. C. Meldrum, H. Colfen, *Chem. Rev.* **2008**, 108, 4332.
- [21] Y. D. Liu, J. Goebel, Y. D. Yin, *Chem. Soc. Rev.* **2013**, 42, 2610.
- [22] K. J. C. van Bommel, A. Friggeri, S. Shinkai, *Angew. Chem., Int. Ed.* **2003**, 42, 980.
- [23] N. Anton, J. P. Benoit, P. Saulnier, *J. Controlled Release* **2008**, 128, 185.
- [24] W. Lee, S. J. Park, *Chem. Rev.* **2014**, 114, 7487.
- [25] N. B. J. Hetherington, A. N. Kulak, Y. Y. Kim, E. H. Noel, D. Snoswell, M. Butler, F. C. Meldrum, *Adv. Funct. Mater.* **2011**, 21, 948.
- [26] W. C. Yoo, S. Kumar, R. L. Penn, M. Tsapatsis, A. Stein, *J. Am. Chem. Soc.* **2009**, 131, 12377.
- [27] C. Li, L. M. Qi, *Angew. Chem., Int. Ed.* **2008**, 47, 2388.
- [28] E. J. W. Crossland, N. Noel, V. Sivaram, T. Leijtens, J. A. Alexander-Webber, H. J. Snaith, *Nature* **2013**, 495, 215.
- [29] W. B. Yue, W. Z. Zhou, *J. Mater. Chem.* **2007**, 17, 4947.
- [30] W. Yue, W. Z. Zhou, *Chem. Mater.* **2007**, 19, 2359.
- [31] R. J. Park, F. C. Meldrum, *Adv. Mater.* **2002**, 14, 1167.
- [32] R. J. Park, F. C. Meldrum, *J. Mater. Chem.* **2004**, 14, 2291.
- [33] B. Wucher, W. B. Yue, A. N. Kulak, F. C. Meldrum, *Chem. Mater.* **2007**, 19, 1111.
- [34] W. B. Yue, A. N. Kulak, F. C. Meldrum, *J. Mater. Chem.* **2006**, 16, 408.
- [35] E. Loste, F. C. Meldrum, *Chem. Commun.* **2001**, 901.
- [36] E. Loste, R. J. Park, J. Warren, F. C. Meldrum, *Adv. Funct. Mater.* **2004**, 14, 1211.
- [37] A. S. Finmore, M. R. J. Scherer, R. Langford, S. Mahajan, S. Ludwigs, F. C. Meldrum, U. Steiner, *Adv. Mater.* **2009**, 21, 3928.
- [38] Y. Y. Kim, N. B. J. Hetherington, E. H. Noel, R. Kroger, J. M. Charnock, H. K. Christenson, F. C. Meldrum, *Angew. Chem., Int. Ed.* **2011**, 50, 12572.
- [39] E. Beniash, R. A. Metzler, R. S. K. Lam, P. Gilbert, *J. Struct. Biol.* **2009**, 166, 133.
- [40] J. H. E. Cartwright, A. G. Checa, J. D. Gale, D. Gebauer, C. I. Sainz-Diaz, *Angew. Chem., Int. Ed.* **2012**, 51, 11960.

- [41] S. Weiner, L. Addadi, in *Annual Review of Materials Research*, Vol. 41 (Eds: D. R. Clarke, P. Fratzl), Annual Reviews, Palo Alto, CA, USA **2011**, p. 21.
- [42] A. Akiva, M. Neder, K. Kahil, R. Gavriel, I. Pinkas, G. Goobes, T. Mass, *Nat. Commun.* **2018**, 9, 1880.
- [43] H. K. Christenson, *J. Phys.: Condens. Matter* **2001**, 13, R95.
- [44] M. Alcoutlabi, G. B. McKenna, *J. Phys.: Condens. Matter* **2005**, 17, R461.
- [45] P. Huber, *J. Phys.: Condens. Matter* **2015**, 27, 103102.
- [46] C. Alba-Simionesco, B. Coasne, G. Dosseh, G. Dudziak, K. E. Gubbins, R. Radhakrishnan, M. Sliwinska-Bartkowiak, *J. Phys.: Condens. Matter* **2006**, 18, R15.
- [47] D. Enke, F. Janowski, W. Schwieger, *Microporous Mesoporous Mater.* **2003**, 60, 19.
- [48] B. Schafer, D. Balszunat, W. Langel, B. Asmussen, *Mol. Phys.* **1996**, 89, 1057.
- [49] D. W. Brown, P. E. Sokol, S. N. Ehrlich, *Phys. Rev. Lett.* **1998**, 81, 1019.
- [50] D. Wallacher, P. Huber, K. Knorr, *J. Low Temp. Phys.* **1998**, 113, 19.
- [51] J. C. Dore, M. Dunn, T. Hasebe, J. H. Strange, *Colloids Surf.* **1989**, 36, 199.
- [52] C. L. Jackson, G. B. McKenna, *J. Chem. Phys.* **1990**, 93, 9002.
- [53] C. Alba-Simionesco, G. Dosseh, E. Dumont, B. Frick, B. Geil, D. Morineau, V. Teboul, Y. Xia, *Eur. Phys. J. E* **2003**, 12, 19.
- [54] D. C. Steytler, J. C. Dore, C. J. Wright, *J. Phys. Chem.* **1983**, 87, 2458.
- [55] D. C. Steytler, J. C. Dore, *Mol. Phys.* **1985**, 56, 1001.
- [56] J. M. Baker, J. C. Dore, P. Behrens, *J. Phys. Chem. B* **1997**, 101, 6226.
- [57] T. Takamuku, M. Yamagami, H. Wakita, Y. Masuda, T. Yamaguchi, *J. Phys. Chem. B* **1997**, 101, 5730.
- [58] K. Morishige, *J. Phys. Chem. C* **2018**, 122, 5013.
- [59] T. L. Malkin, B. J. Murray, C. G. Salzmann, V. Molinero, S. J. Pickering, T. F. Whale, *Phys. Chem. Chem. Phys.* **2015**, 17, 60.
- [60] K. Morishige, H. Uematsu, *J. Chem. Phys.* **2005**, 122, 044711.
- [61] E. B. Moore, E. de la Llave, K. Welke, D. A. Scherlis, V. Molinero, *Phys. Chem. Chem. Phys.* **2010**, 12, 4124.
- [62] E. B. Moore, V. Molinero, *Phys. Chem. Chem. Phys.* **2011**, 13, 20008.
- [63] M. K. Lee, C. Tien, E. V. Charnaya, H. S. Sheu, Y. A. Kumzerov, *Phys. Lett. A* **2010**, 374, 1570.
- [64] K. Overloop, L. Vangerven, *J. Magn. Reson., Ser. A* **1993**, 101, 179.
- [65] K. Morishige, K. Nobuoka, *J. Chem. Phys.* **1997**, 107, 6965.
- [66] D. W. Aksnes, L. Gjerdaker, *J. Mol. Struct.* **1999**, 475, 27.
- [67] C. Gutt, B. Asmussen, I. Krasnov, W. Press, W. Langel, R. Kahn, *Phys. Rev. B* **1999**, 59, 8607.
- [68] P. Laval, A. Crombez, J. B. Salmon, *Langmuir* **2009**, 25, 1836.
- [69] B. Vonnegut, *J. Colloid Sci.* **1948**, 3, 563.
- [70] D. Selzer, C. Frank, M. Kind, *J. Cryst. Growth* **2019**, 517, 39.
- [71] D. Kashchiev, G. M. van Rosmalen, *Cryst. Res. Technol.* **2003**, 38, 555.
- [72] P. Cubillas, M. W. Anderson, in *Zeolites and Catalysis: Synthesis, Reactions and Applications*, Vol. 1 (Eds: J. Cejka, A. Corma, S. Zones), Wiley-VCH, Weinheim, Germany **2010**, p. 1.
- [73] J. J. De Yoreo, P. G. Vekilov, in *Biomineralization*, Vol. 54 (Eds: P. M. Dove, J. J. DeYoreo, S. Weiner), Mineralogical Society of America, Washington, DC, USA **2003**, p. 57.
- [74] D. W. Oxtoby, *J. Phys.: Condens. Matter* **1992**, 4, 7627.
- [75] J. W. Gibbs, *Trans. Connect. Acad. Arts Sci.* **1878**, 16, 343.
- [76] J. W. Gibbs, *Trans. Connect. Acad. Sci.* **1876**, 108, 3.
- [77] R. Becker, W. Doring, *Ann. Phys.* **1935**, 416, 719.
- [78] M. Volmer, A. Weber, *Z. Phys. Chem.* **1926**, 119, 277.
- [79] D. Erdemir, A. Y. Lee, A. S. Myerson, *Acc. Chem. Res.* **2009**, 42, 621.
- [80] R. P. Sear, *Int. Mater. Rev.* **2012**, 57, 328.
- [81] D. Gebauer, P. Raiteri, J. D. Gale, H. Colfen, *Am. J. Sci* **2018**, 318, 969.
- [82] B. E. Mokross, *Mater. Phys. Mech.* **2003**, 6, 13.
- [83] T. L. Hill, *Thermodynamics of Small Systems*, Dover Publications, Mineola, NY, USA **2013**.
- [84] M. Bohenek, A. S. Myerson, W. M. Sun, *J. Cryst. Growth* **1997**, 179, 213.
- [85] P. Laval, J. B. Salmon, M. Joanicot, *J. Cryst. Growth* **2007**, 303, 622.
- [86] R. Grossier, Z. Hammadi, R. Morin, S. Veessler, *Phys. Rev. Lett.* **2011**, 107, 025504.
- [87] C. E. Nicholson, C. Chen, B. Mendis, S. J. Cooper, *Cryst. Growth Des.* **2011**, 11, 363.
- [88] F. Schweitzer, L. Schimanskygeier, *J. Colloid Interface Sci.* **1987**, 119, 67.
- [89] P. Andrezza, F. Lefaucheux, B. Mutaftschiev, *J. Cryst. Growth* **1988**, 92, 415.
- [90] A. S. Shirinyan, M. Wautelet, *Mater. Sci. Eng., C* **2006**, 26, 735.
- [91] D. Reguera, R. K. Bowles, Y. Djikaev, H. Reiss, *J. Chem. Phys.* **2003**, 118, 340.
- [92] R. Grossier, S. Veessler, *Cryst. Growth Des.* **2009**, 9, 1917.
- [93] P. G. Vekilov, *Nanoscale* **2010**, 2, 2346.
- [94] P. R. ten Wolde, D. Frenkel, *Science* **1997**, 277, 1975.
- [95] P. G. Vekilov, *Cryst. Growth Des.* **2010**, 10, 5007.
- [96] O. Galkin, K. Chen, R. L. Nagel, R. E. Hirsch, P. G. Vekilov, *Proc. Natl. Acad. Sci. USA* **2002**, 99, 8479.
- [97] O. Galkin, P. G. Vekilov, *Proc. Natl. Acad. Sci. USA* **2000**, 97, 6277.
- [98] A. M. Streets, S. R. Quake, *Phys. Rev. Lett.* **2010**, 104.
- [99] S. Chattopadhyay, D. Erdemir, J. M. B. Evans, J. Ilavsky, H. Amenitsch, C. U. Segre, A. S. Myerson, *Cryst. Growth Des.* **2005**, 5, 523.
- [100] P. E. Bonnett, K. J. Carpenter, S. Dawson, R. J. Davey, *Chem. Commun.* **2003**, 698.
- [101] A. F. Wallace, L. O. Hedges, A. Fernandez-Martinez, P. Raiteri, J. D. Gale, G. A. Waychunas, S. Whitelam, J. F. Banfield, J. J. De Yoreo, *Science* **2013**, 341, 885.
- [102] T. H. Zhang, X. Y. Liu, *J. Am. Chem. Soc.* **2007**, 129, 13520.
- [103] J. R. Savage, A. D. Dinsmore, *Phys. Rev. Lett.* **2009**, 102, 198302.
- [104] D. Gebauer, H. Coelfen, *Nano Today* **2011**, 6, 564.
- [105] D. Gebauer, A. Voelkel, H. Coelfen, *Science* **2008**, 322, 1819.
- [106] P. J. M. Smeets, A. R. Finney, W. Habraken, F. Nudelman, H. Friedrich, J. Laven, J. J. De Yoreo, P. M. Rodger, N. Sommerdijk, *Proc. Natl. Acad. Sci. USA* **2017**, 114, E7882.
- [107] R. Demichelis, P. Raiteri, J. D. Gale, D. Quigley, D. Gebauer, *Nat. Commun.* **2011**, 2, 590.
- [108] W. J. E. M. Habraken, J. Tao, L. J. Brylka, H. Friedrich, L. Bertinetti, A. S. Schenk, A. Verch, V. Dmitrovic, P. H. H. Bomans, P. M. Frederik, J. Laven, P. van der Schoot, B. Aichmayer, G. de With, J. J. DeYoreo, N. A. J. M. Sommerdijk, *Nat. Commun.* **2013**, 4, 1507.
- [109] A. S. Posner, F. Betts, *Acc. Chem. Res.* **1975**, 8, 273.
- [110] J. Baumgartner, A. Dey, P. H. H. Bomans, C. Le Coadou, P. Fratzl, N. Sommerdijk, D. Faivre, *Nat. Mater.* **2013**, 12, 310.
- [111] D. Turnbull, *J. Chem. Phys.* **1952**, 20, 411.
- [112] Z. Hammadi, R. Grossier, S. Zhang, A. Ikni, N. Candoni, R. Morin, S. Veessler, *Faraday Discuss.* **2015**, 179, 489.
- [113] A. Scheeline, R. L. Behrens, *Biophys. Chem.* **2012**, 165–166, 1.
- [114] E. J. Davis, *Aerosol Sci. Technol.* **1997**, 26, 212.
- [115] L. Hennet, V. Cristiglio, J. Kozaily, I. Pozdnyakova, H. E. Fischer, A. Bytchkov, J. W. E. Drewitt, M. Leydier, D. Thiaudière, S. Gruner, S. Brassamin, D. Zanghi, G. J. Cuello, M. Koza, S. Magazù, G. N. Greaves, D. L. Price, *Eur. Phys. J. Spec. Top.* **2011**, 196, 151.
- [116] S. E. Wolf, J. Leiterer, M. Kappl, F. Emmerling, W. Tremel, *J. Am. Chem. Soc.* **2008**, 130, 12342.
- [117] N. D. Draper, S. F. Bakhroum, A. E. Haddrell, G. R. Agnes, *J. Am. Chem. Soc.* **2007**, 129, 11364.
- [118] I. Weidinger, J. Klein, P. Stockel, H. Baumgartel, T. Leisner, *J. Phys. Chem. B* **2003**, 107, 3636.
- [119] B. Kramer, O. Hubner, H. Vortisch, L. Woste, T. Leisner, M. Schwell, E. Ruhl, H. Baumgartel, *J. Chem. Phys.* **1999**, 111, 6521.
- [120] D. Selzer, N. Tullmann, A. Kiselev, T. Leisner, M. Kind, *Cryst. Growth Des.* **2018**, 18, 4896.

- [121] A. Sarfraz, M. C. Schlegel, J. Wright, F. Emmerling, *Chem. Commun.* **2011**, 47, 9369.
- [122] M. Klimakow, J. Leiterer, J. Kneipp, E. Rossler, U. Panne, K. Rademann, F. Emmerling, *Langmuir* **2010**, 26, 11233.
- [123] D. Knezic, J. Zaccaro, A. S. Myerson, *J. Phys. Chem. B* **2004**, 108, 10672.
- [124] S. Rehder, J. X. Wu, J. Laackmann, H. U. Moritz, J. Rantanen, T. Rades, C. S. Leopold, *Eur. J. Pharm. Sci.* **2013**, 48, 97.
- [125] J. Schenk, L. Trobs, F. Emmerling, J. Kneipp, U. Panne, M. Albrecht, *Anal. Methods* **2012**, 4, 1252.
- [126] T. Gnutzmann, Y. N. Thi, K. Rademann, F. Emmerling, *Cryst. Growth Des.* **2014**, 14, 6445.
- [127] S. Lee, H. S. Wi, W. Jo, Y. C. Cho, H. H. Lee, S. Y. Jeong, Y. I. Kim, G. W. Lee, *Proc. Natl. Acad. Sci. USA* **2016**, 113, 13618.
- [128] G. Hermann, Y. Zhang, B. Wassermann, H. Fischer, M. Quennet, E. Ruhl, *J. Phys. Chem. A* **2017**, 121, 6790.
- [129] R. P. Sear, *CrystEngComm* **2014**, 16, 6506.
- [130] L. Geneviciute, N. Florio, S. Lee, *Cryst. Growth Des.* **2011**, 11, 4440.
- [131] S. Lee, P. J. Sanstead, J. M. Wiener, R. Bebawee, A. G. Hilario, *Langmuir* **2010**, 26, 9556.
- [132] R. Grossier, A. Magnaldo, S. Veessler, *J. Cryst. Growth* **2010**, 312, 487.
- [133] Z. Hammadi, N. Candoni, R. Grossier, M. Ildefonso, R. Morin, S. Veessler, *C. R. Phys.* **2013**, 14, 192.
- [134] I. Rodriguez-Ruiz, S. Veessler, J. Gomez-Morales, J. M. Delgado-Lopez, O. Grauby, Z. Hammadi, N. Candoni, J. M. Garcia-Ruiz, *Cryst. Growth Des.* **2014**, 14, 792.
- [135] J. Leng, J. B. Salmon, *Lab Chip* **2009**, 9, 24.
- [136] H.-H. Shi, Y. Xiao, S. Ferguson, X. Huang, N. Wang, H.-X. Hao, *Lab Chip* **2017**, 17, 2167.
- [137] M. A. Levenstein, C. Anduix-Canto, Y. Y. Kim, M. A. Holden, C. G. Nino, D. C. Green, S. E. Foster, A. N. Kulak, L. Govada, N. E. Chayen, S. Day, C. C. Tang, B. Weinhausen, M. Burghammer, N. Kapur, F. C. Meldrum, *Adv. Funct. Mater.* **2019**, 29, 1808172.
- [138] L. Frenz, A. El Harrak, M. Pauly, S. Begin-Colin, A. D. Griffiths, J. C. Baret, *Angew. Chem., Int. Ed.* **2008**, 47, 6817.
- [139] S. B. Li, M. L. Zeng, T. Gaule, M. J. McPherson, F. C. Meldrum, *Small* **2017**, 13, 2372.
- [140] B. Zheng, L. S. Roach, R. F. Ismagilov, *J. Am. Chem. Soc.* **2003**, 125, 11170.
- [141] B. Zheng, J. D. Tice, L. S. Roach, R. F. Ismagilov, *Angew. Chem., Int. Ed.* **2004**, 43, 2508.
- [142] C. J. Gerdt, V. Tereshko, M. K. Yadav, I. Dementieva, F. Collart, A. Joachimiak, R. C. Stevens, P. Kuhn, A. Kossiakoff, R. F. Ismagilov, *Angew. Chem., Int. Ed.* **2006**, 45, 8156.
- [143] R. D. Dombrowski, J. D. Litster, N. J. Wagner, Y. He, *Chem. Eng. Sci.* **2007**, 62, 4802.
- [144] J. S. I. Kwon, M. Nayhouse, G. Orkoulas, P. D. Christofides, *Chem. Eng. Sci.* **2014**, 119, 30.
- [145] P. Laval, C. Giroux, J. Leng, J. B. Salmon, *J. Cryst. Growth* **2008**, 310, 3121.
- [146] Y. Teshima, M. Maeki, K. Yamashita, M. Miyazaki, *CrystEngComm* **2013**, 15, 9874.
- [147] M. Ildefonso, E. Revalor, P. Punniam, J. B. Salmon, N. Candoni, S. Veessler, *J. Cryst. Growth* **2012**, 342, 9.
- [148] S. Nitahara, M. Maeki, H. Yamaguchi, K. Yamashita, M. Miyazaki, H. Maeda, *Analyst* **2012**, 137, 5730.
- [149] V. Verma, B. K. Hodnett, *CrystEngComm* **2018**, 20, 5551.
- [150] D. Mangin, F. Puel, S. Veessler, *Org. Process Res. Dev.* **2009**, 13, 1241.
- [151] A. Yashina, F. Meldrum, A. deMello, *Biomicrofluidics* **2012**, 6, 022001.
- [152] D. L. Chen, C. J. Gerdt, R. F. Ismagilov, *J. Am. Chem. Soc.* **2005**, 127, 9672.
- [153] Y. Xiao, J. K. Wang, X. Huang, H. H. Shi, Y. A. Zhou, S. Y. Zong, H. X. Hao, Y. Baa, Q. X. Yin, *Cryst. Growth Des.* **2018**, 18, 540.
- [154] E. C. dos Santos, A. Ladosz, G. M. Maggioni, P. R. von Rohr, M. Mazzotti, *Chem. Eng. Res. Des.* **2018**, 138, 444.
- [155] M. Ildefonso, N. Candoni, S. Veessler, *Cryst. Growth Des.* **2011**, 11, 1527.
- [156] L. Goh, K. J. Chen, V. Bhamidi, G. W. He, N. C. S. Kee, P. J. A. Kenis, C. F. Zukoski, R. D. Braatz, *Cryst. Growth Des.* **2010**, 10, 2515.
- [157] S. Teychene, B. Biscans, *Cryst. Growth Des.* **2011**, 11, 4810.
- [158] H. H. Shi, Y. Xiao, X. Huang, Y. Bao, C. Xie, H. X. Hao, *Ind. Eng. Chem. Res.* **2018**, 57, 12784.
- [159] Y. Vitry, S. Teychene, S. Charton, F. Lamadie, B. Biscans, *Chem. Eng. Sci.* **2015**, 133, 54.
- [160] J. Cavanaugh, M. L. Whittaker, D. Joester, *Chem. Sci.* **2019**, 10, 5039.
- [161] B. Spiegel, A. Kafer, M. Kind, *Cryst. Growth Des.* **2018**, 18, 3307.
- [162] C. A. Stan, G. F. Schneider, S. S. Shevkopyas, M. Hashimoto, M. Ibanescu, B. J. Wiley, G. M. Whitesides, *Lab Chip* **2009**, 9, 2293.
- [163] G. M. Pound, V. K. La Mer, *J. Am. Chem. Soc.* **1952**, 74, 2323.
- [164] M. Ildefonso, N. Candoni, S. Veessler, *Cryst. Growth Des.* **2013**, 13, 2107.
- [165] M. Maeki, H. Yamaguchi, K. Yamashita, H. Nakamura, M. Miyazaki, H. Maeda, *Chem. Lett.* **2011**, 40, 825.
- [166] N. Jiang, Z. Z. Wang, L. P. Dang, H. Y. Wei, *J. Cryst. Growth* **2016**, 446, 68.
- [167] J. L. Hilden, C. E. Reyes, M. J. Kelm, J. S. Tan, J. G. Stowell, K. R. Morris, *Cryst. Growth Des.* **2003**, 3, 921.
- [168] J. Desarnaud, H. Derluyn, J. Carmeliet, D. Bonn, N. Shahidzadeh, *J. Phys. Chem. Lett.* **2018**, 9, 2961.
- [169] J. Desarnaud, H. Derluyn, J. Carmeliet, D. Bonn, N. Shahidzadeh, *J. Phys. Chem. Lett.* **2014**, 5, 890.
- [170] M. J. Qazi, R. W. Liefferink, S. J. Schlegel, E. H. G. Backus, D. Bonn, N. Shahidzadeh, *Langmuir* **2017**, 33, 4260.
- [171] C. J. Stephens, Y. Y. Kim, S. D. Evans, F. C. Meldrum, H. K. Christenson, *J. Am. Chem. Soc.* **2011**, 133, 5210.
- [172] J. Ihli, J. N. Clark, A. S. Cote, Y. Y. Kim, A. S. Schenk, A. N. Kulak, T. P. Comyn, O. Chammas, R. J. Harder, D. M. Duffy, I. K. Robinson, F. C. Meldrum, *Nat. Commun.* **2016**, 7, 11878.
- [173] A. Y. Lee, I. S. Lee, A. S. Myerson, *Chem. Eng. Technol.* **2006**, 29, 281.
- [174] A. Y. Lee, I. S. Lee, S. S. Dettet, J. Boerner, A. S. Myerson, *J. Am. Chem. Soc.* **2005**, 127, 14982.
- [175] I. S. Lee, K. T. Kim, A. Y. Lee, A. S. Myerson, *Cryst. Growth Des.* **2008**, 8, 108.
- [176] I. S. Lee, A. Y. Lee, A. S. Myerson, *Pharm. Res.* **2008**, 25, 960.
- [177] K. Kim, A. Centrone, T. A. Hatton, A. S. Myerson, *CrystEngComm* **2011**, 13, 1127.
- [178] K. Kim, I. S. Lee, A. Centrone, T. A. Hatton, A. S. Myerson, *J. Am. Chem. Soc.* **2009**, 131, 18212.
- [179] A. Singh, I. S. Lee, A. S. Myerson, *Cryst. Growth Des.* **2009**, 9, 1182.
- [180] N. Sanandaji, A. Oko, D. B. Haviland, E. A. Tholen, M. S. Hedenqvist, U. W. Gedde, *Eur. Polym. J.* **2013**, 49, 203.
- [181] P. A. Melendez, K. M. Kane, C. S. Ashvar, M. Albrecht, P. A. Smith, *J. Pharm. Sci.* **2008**, 97, 2619.
- [182] A. B. M. Buanz, R. Telford, I. J. Scowen, S. Gaisford, *CrystEngComm* **2013**, 15, 1031.
- [183] A. Buanz, M. Gurung, S. Gaisford, *CrystEngComm* **2019**, 21, 2212.
- [184] A. B. M. Buanz, S. Gaisford, *Cryst. Growth Des.* **2017**, 17, 1245.
- [185] M. P. Pileni, *Cryst. Res. Technol.* **1998**, 33, 1155.
- [186] S. N. Khadzhiev, K. M. Kadiev, G. P. Yampolskaya, M. K. Kadieva, *Adv. Colloid Interface Sci.* **2013**, 197–198, 132.
- [187] J. Eastoe, M. J. Hollamby, L. Hudson, *Adv. Colloid Interface Sci.* **2006**, 128–130, 5.
- [188] K. Holmberg, *J. Colloid Interface Sci.* **2004**, 274, 355.
- [189] M. P. Pileni, *Nat. Mater.* **2003**, 2, 145.
- [190] D. G. Shchukin, G. B. Sukhorukov, *Adv. Mater.* **2004**, 16, 671.
- [191] V. Uskokovic, M. Drogenik, *Surf. Rev. Lett.* **2005**, 12, 239.

- [192] Y. Chen, Q. S. Wu, Y. Dingibi, *Eur. J. Inorg. Chem.* **2007**, 2007, 4906.
- [193] G. D. Rees, R. Evans-Gowing, S. J. Hammond, B. H. Robinson, *Langmuir* **1999**, 15, 1993.
- [194] J. D. Hopwood, S. Mann, *Chem. Mater.* **1997**, 9, 1819.
- [195] M. Li, S. Mann, *Adv. Funct. Mater.* **2002**, 12, 773.
- [196] C. E. Nicholson, S. J. Cooper, *Crystals* **2011**, 1, 195.
- [197] C. Chen, O. Cook, C. E. Nicholson, S. J. Cooper, *Cryst. Growth Des.* **2011**, 11, 2228.
- [198] C. Beato, M. S. Fernandez, S. Fermani, M. Reggi, A. Neira-Carrillo, A. Rao, G. Falini, J. L. Arias, *CrystEngComm* **2015**, 17, 5953.
- [199] P. Wan, Y. Zhao, H. Tong, Z. Y. Yang, Z. H. Zhu, X. Y. Shen, J. M. Hu, *Mater. Sci. Eng., C* **2009**, 29, 222.
- [200] S. Mann, J. P. Hannington, *J. Colloid Interface Sci.* **1988**, 122, 326.
- [201] S. Mann, J. P. Hannington, R. J. P. Williams, *Nature* **1986**, 324, 565.
- [202] C. Faure, M. E. Meyre, S. Trepout, O. Lambert, E. Lebraud, *J. Phys. Chem. B* **2009**, 113, 8552.
- [203] W. Y. Chen, C. I. Yang, C. J. Lin, S. J. Huang, J. C. C. Chan, *J. Phys. Chem. C* **2014**, 118, 12022.
- [204] B. R. Heywood, E. D. Eanes, *Calcif. Tissue Int.* **1987**, 41, 192.
- [205] B. R. Heywood, E. D. Eanes, *Calcif. Tissue Int.* **1992**, 50, 149.
- [206] C. C. Tester, R. E. Brock, C. H. Wu, M. R. Krejci, S. Weigand, D. Joester, *CrystEngComm* **2011**, 13, 3975.
- [207] C. C. Tester, D. Joester, in *Research Methods in Biomineralization Science*, Vol. 532 (Ed: J. J. D. Yoreo), Academic Press, San Diego, CA, USA **2013**, p. 257.
- [208] C. C. Tester, M. L. Whittaker, D. Joester, *Chem. Commun.* **2014**, 50, 5619.
- [209] C. C. Tester, C. H. Wu, S. Weigand, D. Joester, *Faraday Discuss.* **2012**, 159, 345.
- [210] O. Sohnel, *J. Cryst. Growth* **1982**, 57, 101.
- [211] O. Sohnel, J. W. Mullin, *J. Cryst. Growth* **1978**, 44, 377.
- [212] Q. Hu, M. H. Nielsen, C. L. Freeman, L. M. Hamm, J. Tao, J. R. I. Lee, T. Y. J. Han, U. Becker, J. H. Harding, P. M. Dove, J. J. De Yoreo, *Faraday Discuss.* **2012**, 159, 509.
- [213] B. D. Hamilton, J. M. Ha, M. A. Hillmyer, M. D. Ward, *Acc. Chem. Res.* **2012**, 45, 414.
- [214] Q. Jiang, M. D. Ward, *Chem. Soc. Rev.* **2014**, 43, 2066.
- [215] R. R. Meyer, J. Sloan, R. E. Dunin-Borkowski, A. I. Kirkland, M. C. Novotny, S. R. Bailey, J. L. Hutchison, M. L. H. Green, *Science* **2000**, 289, 1324.
- [216] J. Sloan, M. C. Novotny, S. R. Bailey, G. Brown, C. Xu, V. C. Williams, S. Friedrichs, E. Flahaut, R. L. Callender, A. P. E. York, K. S. Coleman, M. L. H. Green, R. E. Dunin-Borkowski, J. L. Hutchison, *Chem. Phys. Lett.* **2000**, 329, 61.
- [217] M. Hulman, H. Kuzmany, P. Costa, S. Friedrichs, M. L. H. Green, *Appl. Phys. Lett.* **2004**, 85, 2068.
- [218] H. Kim, M. J. Kaufman, W. M. Sigmund, D. Jacques, R. Andrews, *J. Mater. Res.* **2003**, 18, 1104.
- [219] R. Carter, J. Sloan, A. I. Kirkland, R. R. Meyer, P. J. D. Lindan, G. Lin, M. L. H. Green, A. Vlandas, J. L. Hutchison, J. Harding, *Phys. Rev. Lett.* **2006**, 96, 215501.
- [220] E. Flahaut, J. Sloan, S. Friedrichs, A. I. Kirkland, K. S. Coleman, V. C. Williams, N. Hanson, J. L. Hutchison, M. L. H. Green, *Chem. Mater.* **2006**, 18, 2059.
- [221] L. H. Guan, K. Suenaga, Z. J. Shi, Z. N. Gu, S. Iijima, *Nano Lett.* **2007**, 7, 1532.
- [222] S. Iijima, *Nature* **1991**, 354, 56.
- [223] T. W. Ebbesen, P. M. Ajayan, *Nature* **1992**, 358, 220.
- [224] E. Dujardin, T. W. Ebbesen, H. Hiura, K. Tanigaki, *Science* **1994**, 265, 1850.
- [225] P. M. Ajayan, S. Iijima, *Nature* **1993**, 361, 333.
- [226] C. Guerret-Piecourt, Y. Lebouar, A. Loiseau, H. Pascard, *Nature* **1994**, 372, 761.
- [227] C. H. Kiang, J. S. Choi, T. T. Tran, A. D. Bacher, *J. Phys. Chem. B* **1999**, 103, 7449.
- [228] S. C. Tsang, Y. K. Chen, P. J. F. Harris, M. L. H. Green, *Nature* **1994**, 372, 159.
- [229] P. M. Ajayan, O. Stephan, P. Redlich, C. Colliex, *Nature* **1995**, 375, 564.
- [230] J. Mittal, M. Monthieux, H. Allouche, O. Stephan, *Chem. Phys. Lett.* **2001**, 339, 311.
- [231] S. Friedrichs, R. R. Meyer, J. Sloan, A. I. Kirkland, J. L. Hutchison, M. L. H. Green, *Chem. Commun.* **2001**, 929.
- [232] S. Friedrichs, J. Sloan, M. L. H. Green, J. L. Hutchison, R. R. Meyer, A. I. Kirkland, *Phys. Rev. B* **2001**, 64, 045406.
- [233] M. Liu, J. M. Cowley, *Carbon* **1995**, 33, 225.
- [234] M. Terrones, W. K. Hsu, A. Schilder, H. Terrones, N. Grobert, J. P. Hare, Y. Q. Zhu, M. Schwoerer, K. Prassides, H. W. Kroto, D. R. M. Walton, *Appl. Phys. A: Mater. Sci. Process.* **1998**, 66, 307.
- [235] D. Ugarte, A. Chatelain, W. A. deHeer, *Science* **1996**, 274, 1897.
- [236] J. Sloan, J. Cook, A. Chu, M. Zwiefka-Sibley, M. L. H. Green, J. L. Hutchison, *J. Solid State Chem.* **1998**, 140, 83.
- [237] W. K. Hsu, W. Z. Li, Y. Q. Zhu, N. Grobert, M. Terrones, H. Terrones, N. Yao, J. P. Zhang, S. Firth, R. J. H. Clark, A. K. Cheetham, J. P. Hare, H. W. Kroto, D. R. M. Walton, *Chem. Phys. Lett.* **2000**, 317, 77.
- [238] J. Sloan, S. Friedrichs, R. R. Meyer, A. I. Kirkland, J. L. Hutchison, M. L. H. Green, *Inorg. Chim. Acta* **2002**, 330, 1.
- [239] M. Monthieux, *Carbon* **2002**, 40, 1809.
- [240] S. Sandoval, G. Tobias, E. Flahaut, *Inorg. Chim. Acta* **2019**, 492, 66.
- [241] W. Q. Han, C. W. Chang, A. Zettl, *Nano Lett.* **2004**, 4, 1355.
- [242] A. N. Enyashin, R. Kreizman, G. Seifert, *J. Phys. Chem. C* **2009**, 113, 13664.
- [243] S. Y. Hong, R. Kreizman, R. Rosentsveig, A. Zak, J. Sloan, A. N. Enyashin, G. Seifert, M. L. H. Green, R. Tenne, *Eur. J. Inorg. Chem.* **2010**, 2010, 4233.
- [244] S. Y. Hong, R. Popovitz-Biro, G. Tobias, B. Ballesteros, B. G. Davis, M. L. H. Green, R. Tenne, *Nano Res.* **2010**, 3, 170.
- [245] M. Wilson, *J. Chem. Phys.* **2002**, 116, 3027.
- [246] M. Wilson, P. A. Madden, *J. Am. Chem. Soc.* **2001**, 123, 2101.
- [247] M. Wilson, *Chem. Phys. Lett.* **2002**, 366, 504.
- [248] K. Urita, Y. Shiga, T. Fujimori, T. Iiyama, Y. Hattori, H. Kanoh, T. Ohba, H. Tanaka, M. Yudasaka, S. Iijima, I. Moriguchi, F. Okino, M. Endo, K. Kaneko, *J. Am. Chem. Soc.* **2011**, 133, 10344.
- [249] S. N. Wang, D. Yin, Z. Y. Li, J. L. Yang, *J. Phys. Chem. Lett.* **2012**, 3, 2154.
- [250] C. G. Xu, J. Sloan, G. Brown, S. Bailey, V. C. Williams, S. Friedrichs, K. S. Coleman, E. Flahaut, J. L. Hutchison, R. E. Dunin-Borkowski, M. L. H. Green, *Chem. Commun.* **2000**, 2427.
- [251] J. Sloan, S. J. Grosvenor, S. Friedrichs, A. I. Kirkland, J. L. Hutchison, M. L. H. Green, *Angew. Chem., Int. Ed.* **2002**, 41, 1156.
- [252] E. Philp, J. Sloan, A. I. Kirkland, R. R. Meyer, S. Friedrichs, J. L. Hutchison, M. L. H. Green, *Nat. Mater.* **2003**, 2, 788.
- [253] X. Fan, E. C. Dickey, P. C. Eklund, K. A. Williams, L. Grigorian, R. Buczko, S. T. Pantelides, S. J. Pennycook, *Phys. Rev. Lett.* **2000**, 84, 4621.
- [254] P. M. F. J. Costa, S. Friedrichs, J. Sloan, M. L. H. Green, *Chem. Mater.* **2005**, 17, 3122.
- [255] G. Chen, J. Qiu, H. X. Qiu, *Scr. Mater.* **2008**, 58, 457.
- [256] R. Senga, H. P. Komsa, Z. Liu, K. Hirose-Takai, A. V. Krasheninnikov, K. Suenaga, *Nat. Mater.* **2014**, 13, 1050.
- [257] H. Muramatsu, T. Hayashi, Y. A. Kim, D. Shimamoto, M. Endo, M. Terrones, M. S. Dresselhaus, *Nano Lett.* **2008**, 8, 237.
- [258] V. Meunier, H. Muramatsu, T. Hayashi, Y. A. Kim, D. Shimamoto, H. Terrones, M. S. Dresselhaus, M. Terrones, M. Endo, B. G. Sumpter, *Nano Lett.* **2009**, 9, 1487.
- [259] G. Schmid, *J. Mater. Chem.* **2002**, 12, 1231.
- [260] C. R. Martin, *Chem. Mater.* **1996**, 8, 1739.

- [261] A. M. M. Jani, D. Losic, N. H. Voelcker, *Prog. Mater. Sci.* **2013**, *58*, 636.
- [262] C. Bae, H. Yoo, S. Kim, K. Lee, J. Kim, M. A. Sung, H. Shin, *Chem. Mater.* **2008**, *20*, 756.
- [263] S. J. Hurst, E. K. Payne, L. D. Qin, C. A. Mirkin, *Angew. Chem., Int. Ed.* **2006**, *45*, 2672.
- [264] A. Kolmakov, M. Moskovits, *Annu. Rev. Mater. Res.* **2004**, *34*, 151.
- [265] H. Q. Cao, Y. Xu, J. M. Hong, H. B. Liu, G. Yin, B. L. Li, C. Y. Tie, Z. Xu, *Adv. Mater.* **2001**, *13*, 1393.
- [266] Z. Miao, D. S. Xu, J. H. Ouyang, G. L. Guo, X. S. Zhao, Y. Q. Tang, *Nano Lett.* **2002**, *2*, 717.
- [267] Y. B. Mao, S. S. Wong, *J. Am. Chem. Soc.* **2004**, *126*, 15245.
- [268] H. J. Zhou, S. S. Wong, *ACS Nano* **2008**, *2*, 944.
- [269] Y. Mao, F. Zhang, S. S. Wong, *Adv. Mater.* **2006**, *18*, 1895.
- [270] F. Zhang, S. S. Wong, *ACS Nano* **2010**, *4*, 99.
- [271] J. M. Ha, M. A. Hillmyer, M. D. Ward, *J. Phys. Chem. B* **2005**, *109*, 1392.
- [272] B. D. Hamilton, I. Weissbuch, M. Lahav, M. A. Hillmyer, M. D. Ward, *J. Am. Chem. Soc.* **2009**, *131*, 2588.
- [273] B. Cantaert, E. Beniash, F. C. Meldrum, *Chem. - Eur. J.* **2013**, *19*, 14918.
- [274] C. V. Thompson, *Annu. Rev. Mater. Sci.* **2000**, *30*, 159.
- [275] H. Bishara, S. Berger, *J. Mater. Sci.* **2019**, *54*, 4619.
- [276] Q. Jiang, H. Hu, M. D. Ward, *J. Am. Chem. Soc.* **2013**, *135*, 2144.
- [277] B. D. Hamilton, M. A. Hillmyer, M. D. Ward, *Cryst. Growth Des.* **2008**, *8*, 3368.
- [278] J. M. Ha, J. H. Wolf, M. A. Hillmyer, M. D. Ward, *J. Am. Chem. Soc.* **2004**, *126*, 3382.
- [279] K. Zong, Y. C. Ma, K. Shayan, J. Ly, E. Renjilian, C. H. Hu, S. Strauf, A. Briseno, S. S. Lee, *Cryst. Growth Des.* **2019**, *19*, 3461.
- [280] G. Graubner, G. T. Rengarajan, N. Anders, N. Sonnenberger, D. Enke, M. Beiner, M. Steinhart, *Cryst. Growth Des.* **2014**, *14*, 78.
- [281] J. M. Ha, B. D. Hamilton, M. A. Hillmyer, M. D. Ward, *Cryst. Growth Des.* **2012**, *12*, 4494.
- [282] D. Yadlovker, S. Berger, *J. Appl. Phys.* **2007**, *101*, 034304.
- [283] J. Xu, N. Petkov, X. Wu, D. Iacopino, A. J. Quinn, G. Redmond, T. Bein, M. A. Morris, J. D. Holmes, *ChemPhysChem* **2007**, *8*, 235.
- [284] J. Xu, X. H. Liu, Y. D. Li, *Mater. Chem. Phys.* **2004**, *86*, 409.
- [285] D. Routkevitch, T. Bigioni, M. Moskovits, J. M. Xu, *J. Phys. Chem.* **1996**, *100*, 14037.
- [286] A. Henschel, P. Kumar, T. Hofmann, K. Knorr, P. Huber, *Phys. Rev. E* **2009**, *79*, 4.
- [287] B. Cantaert, E. Beniash, F. C. Meldrum, *J. Mater. Chem. B* **2013**, *1*, 6586.
- [288] S. Weiner, W. Traub, H. D. Wagner, *J. Struct. Biol.* **1999**, *126*, 241.
- [289] N. Reznikov, M. Bilton, L. Lari, M. M. Stevens, R. Kroger, *Science* **2018**, *360*, eaao2189.
- [290] F. Nudelman, K. Pieterse, A. George, P. H. H. Bomans, H. Friedrich, L. J. Brylka, P. A. J. Hilbers, G. de With, N. Sommerdijk, *Nat. Mater.* **2010**, *9*, 1004.
- [291] M. J. Olszta, X. Cheng, S. S. Jee, R. Kumar, Y.-Y. Kim, M. J. Kaufman, E. P. Douglas, L. B. Gower, *Mater. Sci. Eng. R* **2007**, *58*, 77.
- [292] H. Orikasa, J. Karoji, K. Matsui, T. Kyotani, *Dalton Trans.* **2007**, 3757.
- [293] M. Beiner, G. T. Rengarajan, S. Pankaj, D. Enke, M. Steinhart, *Nano Lett.* **2007**, *7*, 1381.
- [294] G. T. Rengarajan, D. Enke, M. Steinhart, M. Beiner, *J. Mater. Chem.* **2008**, *18*, 2537.
- [295] G. T. Rengarajan, D. Enke, M. Steinhart, M. Beiner, *Phys. Chem. Chem. Phys.* **2011**, *13*, 21367.
- [296] C. L. Jackson, G. B. McKenna, *Chem. Mater.* **1996**, *8*, 2128.
- [297] J. M. Ha, B. D. Hamilton, M. A. Hillmyer, M. D. Ward, *Cryst. Growth Des.* **2009**, *9*, 4766.
- [298] Z. B. Zhang, D. Gekhtman, M. S. Dresselhaus, J. Y. Ying, *Chem. Mater.* **1999**, *11*, 1659.
- [299] S. Ma, S. H. Kim, B. Jeong, H. C. Kwon, S. C. Yun, G. Fang, H. Yang, C. Park, D. Lee, J. Moon, *Small* **2019**, *15*, 1900219.
- [300] S. Lee, J. Feldman, S. S. Lee, *Cryst. Growth Des.* **2016**, *16*, 4744.
- [301] C. Anduix-Canto, Y. Y. Kim, Y. W. Wang, A. Kulak, F. C. Meldrum, H. K. Christenson, *Cryst. Growth Des.* **2016**, *16*, 5403.
- [302] A. S. Schenk, E. J. Albarracin, Y. Y. Kim, J. Ihli, F. C. Meldrum, *Chem. Commun.* **2014**, *50*, 4729.
- [303] A. Verch, A. S. Cote, R. Darkins, Y. Y. Kim, R. van de Locht, F. C. Meldrum, D. M. Duffy, R. Kroger, *Small* **2014**, *10*, 2697.
- [304] L. B. Gower, *Chem. Rev.* **2008**, *108*, 4551.
- [305] M. L. Zeng, Y. Y. Kim, C. Anduix-Canto, C. Frontera, D. Laundry, N. Kapur, H. K. Christenson, F. C. Meldrum, *Proc. Natl. Acad. Sci. USA* **2018**, *115*, 7670.
- [306] Y. J. Diao, R. M. Espinosa-Marzal, *Proc. Natl. Acad. Sci. USA* **2016**, *113*, 12047.
- [307] A. Kirch, S. M. Mutisya, V. M. Sanchez, J. M. de Almeida, C. R. Miranda, *J. Phys. Chem. C* **2018**, *122*, 6117.
- [308] B. S. Kim, Y. G. Jeong, K. Shin, *J. Phys. Chem. B* **2013**, *117*, 5978.
- [309] I. Lee, H. Han, S. Y. Lee, *J. Cryst. Growth* **2010**, *312*, 1741.
- [310] Q. Jiang, X. H. Zhou, Z. Wen, *Appl. Surf. Sci.* **2002**, *195*, 38.
- [311] K. E. Bremmell, C. A. Prestidge, *Drug Dev. Ind. Pharm.* **2019**, *45*, 349.
- [312] A. Maleki, H. Kettiger, A. Schoubben, J. M. Rosenholm, V. Ambrogi, M. Hamidi, *J. Controlled Release* **2017**, *262*, 329.
- [313] C. A. McCarthy, R. J. Ahern, R. Dontireddy, K. B. Ryan, A. M. Crean, *Expert Opin. Drug Delivery* **2016**, *13*, 93.
- [314] K. K. Qian, R. H. Bogner, *J. Pharm. Sci.* **2012**, *101*, 444.
- [315] M. Van Speybroeck, V. Barillaro, T. Do Thi, R. Mellaerts, J. Martens, J. Van Humbeeck, J. Vermant, P. Annaert, G. Van Den Mooter, P. Augustijns, *J. Pharm. Sci.* **2009**, *98*, 2648.
- [316] T. Azais, G. Hartmeyer, S. Quignard, G. Laurent, F. Babonneau, *J. Phys. Chem. C* **2010**, *114*, 8884.
- [317] E. Skorupska, A. Jeziorna, P. Paluch, M. J. Potrzebowski, *Mol. Pharmaceutics* **2014**, *11*, 1512.
- [318] K. P. Nartowski, D. Malhotra, L. E. Hawarden, J. Sibik, D. Iuga, J. A. Zeidler, L. Fabian, Y. Z. Khimyak, *Angew. Chem., Int. Ed.* **2016**, *55*, 8904.
- [319] K. P. Nartowski, J. Tedder, D. E. Braun, L. Fabian, Y. Z. Khimyak, *Phys. Chem. Chem. Phys.* **2015**, *17*, 24761.
- [320] J. Israelachvili, Y. Min, M. Akbulut, A. Alig, G. Carver, W. Greene, K. Kristiansen, E. Meyer, N. Pesika, K. Rosenberg, H. Zeng, *Rep. Prog. Phys.* **2010**, *73*, 036601.
- [321] T. Grunewald, L. Dahne, C. A. Helm, *J. Phys. Chem. B* **1998**, *102*, 4988.
- [322] J. Dziadkowiec, B. Zareepolgardani, D. K. Dysthe, A. Royné, *Sci. Rep.* **2019**, *9*, 8948.
- [323] J. Dziadkowiec, S. Jayadi, J. E. Bratvold, O. Nilsen, A. Royné, *Langmuir* **2018**, *34*, 7248.
- [324] J. Hogberget, A. Royné, D. K. Dysthe, E. Jettestuen, *Phys. Rev. E* **2016**, *94*, 023005.
- [325] L. Gagliardi, O. Pierre-Louis, *Phys. Rev. E* **2018**, *97*, 012802.
- [326] C. J. Stephens, S. F. Ladden, F. C. Meldrum, H. K. Christenson, *Adv. Funct. Mater.* **2010**, *20*, 2108.
- [327] Y. W. Wang, M. L. Zeng, F. C. Meldrum, H. K. Christenson, *Cryst. Growth Des.* **2017**, *17*, 6787.
- [328] Y. W. Wang, H. K. Christenson, F. C. Meldrum, *Chem. Mater.* **2014**, *26*, 5830.
- [329] J. Ihli, Y. W. Wang, B. Cantaert, Y. Y. Kim, D. C. Green, P. H. H. Bomans, N. Sommerdijk, F. C. Meldrum, *Chem. Mater.* **2015**, *27*, 3999.
- [330] Y. W. Wang, H. K. Christenson, F. C. Meldrum, *Adv. Funct. Mater.* **2013**, *23*, 5615.
- [331] J. Kawano, N. Shimobayashi, A. Miyake, M. Kitamura, *J. Phys.: Condens. Matter* **2009**, *21*, 425102.
- [332] J. Ihli, A. N. Kulak, F. C. Meldrum, *Chem. Commun.* **2013**, *49*, 3134.

- [333] H. S. Lee, T. H. Ha, K. Kim, *Mater. Chem. Phys.* **2005**, *93*, 376.
- [334] J. Ihli, W. C. Wong, E. H. Noel, Y. Y. Kim, A. N. Kulak, H. K. Christenson, M. J. Duer, F. C. Meldrum, *Nat. Commun.* **2014**, *5*, 3169.
- [335] M. Kellermeier, A. Picker, A. Kempter, H. Colfen, D. Gebauer, *Adv. Mater.* **2014**, *26*, 752.
- [336] A. E. S. Van Driessche, L. G. Benning, J. D. Rodriguez-Blanco, M. Ossorio, P. Bots, J. M. Garcia-Ruiz, *Science* **2012**, *336*, 69.
- [337] D. E. Kile, D. D. Eberl, *Am. Mineral.* **2003**, *88*, 1514.
- [338] M. Hajir, R. Graf, W. Tremel, *Chem. Commun.* **2014**, *50*, 6534.
- [339] J. M. Campbell, H. K. Christenson, *Phys. Rev. Lett.* **2018**, *120*, 165701.
- [340] J. M. Campbell, F. C. Meldrum, H. K. Christenson, *Proc. Natl. Acad. Sci. USA* **2017**, *114*, 810.
- [341] A. J. Page, R. P. Sear, *Phys. Rev. Lett.* **2006**, *97*, 065701.
- [342] A. J. Page, R. P. Sear, *J. Am. Chem. Soc.* **2009**, *131*, 17550.
- [343] Y. F. Bi, B. X. Cao, T. S. Li, *Nat. Commun.* **2017**, *8*, 15372.
- [344] X. Q. Gong, Y. W. Wang, J. Ihli, Y. Y. Kim, S. B. Li, R. Walshaw, L. Chen, F. C. Meldrum, *Adv. Mater.* **2015**, *27*, 7395.
- [345] Y. Y. Kim, C. L. Freeman, X. Q. Gong, M. A. Levenstein, Y. W. Wang, A. Kulak, C. Anduix-Canto, P. A. Lee, S. B. Li, L. Chen, H. K. Christenson, F. C. Meldrum, *Angew. Chem., Int. Ed.* **2017**, *56*, 11885.
- [346] L. Y. Wang, M. H. Lee, J. Barton, L. Hughes, T. W. Odom, *J. Am. Chem. Soc.* **2008**, *130*, 2142.
- [347] L. E. Englade-Franklin, G. Morrison, S. D. Verberne-Sutton, A. L. Francis, J. Y. Chan, J. C. Garno, *ACS Appl. Mater. Interfaces* **2014**, *6*, 15942.
- [348] R. Kröger, A. Verch, *Minerals* **2018**, *8*, 21.
- [349] M. H. Nielsen, S. Aloni, J. J. De Yoreo, *Science* **2014**, *345*, 1158.
- [350] A. G. Stack, *Rev. Mineral. Geochem.* **2015**, *80*, 165.
- [351] A. Putnis, *Rev. Miner. Geochem.* **2015**, *80*, 1.
- [352] Y. Wang, *Chem. Geol.* **2014**, *378–379*, 1.
- [353] A. Putnis, H. Austrheim, *Geofluids* **2010**, *10*, 254.
- [354] R. F. Krueger, *J. Pet. Technol.* **1986**, *38*, 131.
- [355] S. Kumar, T. K. Naiya, T. Kumar, *J. Pet. Sci. Eng.* **2018**, *169*, 428.
- [356] E. D. Skouras, V. Sygouni, G. N. Constantinides, C. A. Paraskeva, *Cryst. Growth Des.* **2016**, *16*, 6230.
- [357] J. Moghadasi, H. Müller-Steinhagen, M. Jamialahmadi, A. Sharif, *J. Pet. Sci. Eng.* **2004**, *43*, 201.
- [358] A. Putnis, G. Mauthe, *Geofluids* **2001**, *1*, 37.
- [359] N. I. Prasianakis, E. Curti, G. Kosakowski, J. Poonosamy, S. V. Churakov, *Sci. Rep.* **2017**, *7*, 13765.
- [360] M. Prieto, A. Putnis, L. Fernandez-Diaz, *Geol. Mag.* **1990**, *127*, 485.
- [361] C. Rodriguez-Navarro, E. Doehne, *Earth Surf. Processes Landforms* **1999**, *24*, 191.
- [362] M. Steiger, *Transport and Reactivity of Solutions in Confined Hydrosystems*, Springer, Netherlands **2014**.
- [363] E. Doehne, *Spec. Publ. - Geol. Soc. London* **2002**, *205*, 51.
- [364] C. Noiriel, F. Renard, M. L. Doan, J. P. Gratier, *Chem. Geol.* **2010**, *269*, 197.
- [365] G. W. Scherer, *Cem. Concr. Res.* **1999**, *29*, 1347.
- [366] R. J. Flatt, *J. Cryst. Growth* **2002**, *242*, 435.
- [367] S. M. Ghaderi, R. Kharrat, H. A. Tahmasebi, *Oil Gas Sci. Technol. - Rev. l'IFP* **2009**, *64*, 489.
- [368] A. Haghtalab, M. J. Kamali, A. Shahrabadi, H. Golghanddashti, *Chem. Eng. Commun.* **2015**, *202*, 1221.
- [369] M. Kamalipour, S. A. Mousavi Dehghani, A. Naseri, S. Abbasi, *J. Nat. Gas Sci. Eng.* **2017**, *46*, 738.
- [370] V. Cnudde, M. N. Boone, *Earth-Sci. Rev.* **2013**, *123*, 1.
- [371] V. Cnudde, J. Dewanckele, M. Boone, T. de Kock, M. Boone, L. Brabant, M. Duser, M. de Ceukelaire, H. de Clercq, R. Hayen, P. Jacobs, *Microsc. Res. Tech.* **2011**, *74*, 1006.
- [372] J. R. A. Godinho, L. Ma, Y. Chai, M. Storm, T. L. Burnett, *Minerals* **2019**, *9*, 480.
- [373] J. R. A. Godinho, P. J. Withers, *Geochim. Cosmochim. Acta* **2018**, *222*, 156.
- [374] J. Dewanckele, T. De Kock, M. A. Boone, V. Cnudde, L. Brabant, M. N. Boone, G. Fronteau, L. Van Hoorebeke, P. Jacobs, *Sci. Total Environ.* **2012**, *416*, 436.
- [375] M. Prieto, C. Viedma, V. Lopez-Acevedo, J. L. Martin-Vivaldi, S. Lopez-Andres, *J. Cryst. Growth* **1988**, *92*, 61.
- [376] M. Prieto, L. Fernández-Díaz, S. Lopez-Andres, *J. Cryst. Growth* **1989**, *98*, 447.
- [377] M. Prieto, A. Putnis, L. Fernández-Díaz, S. López-Andrés, *J. Cryst. Growth* **1994**, *142*, 225.
- [378] A. Putnis, M. Prieto, L. Fernandez-Diaz, *Geol. Mag.* **1995**, *132*, 1.
- [379] L. Fernandez-Diaz, A. Putnis, M. Prieto, C. V. Putnis, *J. Sediment. Res.* **1996**, *66*, 482.
- [380] M. Prieto, A. Fernández-González, A. Putnis, L. Fernández-Díaz, *Geochim. Cosmochim. Acta* **1997**, *61*, 3383.
- [381] F. C. Meldrum, S. T. Hyde, *J. Cryst. Growth* **2001**, *231*, 544.
- [382] K. J. Davis, P. M. Dove, J. J. De Yoreo, *Science* **2000**, *290*, 1134.
- [383] A. Fernández González, V. B. Pedreira, M. Prieto, *J. Cryst. Growth* **2008**, *310*, 4616.
- [384] M. Prieto, *Mineral. Mag.* **2014**, *78*, 1437.
- [385] A. G. Stack, J. L. Bañuelos, G. Rother, L. M. Anovitz, A. Fernandez-Martinez, L. F. Allard, D. R. Cole, G. A. Waychunas, *Environ. Sci. Technol.* **2014**, *48*, 6177.
- [386] S. Emmanuel, B. Berkowitz, *Geophys. Res. Lett.* **2007**, *34*, L06404.
- [387] G. F. Becker, A. L. Day, *Proc. Washington Acad. Sci.* **1905**, *7*, 283.
- [388] G. F. Becker, A. L. Day, *J. Geol.* **1916**, *24*, 313.
- [389] C. W. Correns, W. Steinborn, *Z. Kristal.* **1939**, *101*, 117.
- [390] C. W. Correns, *Discuss. Faraday Soc.* **1949**, *5*, 267.
- [391] M. Steiger, *J. Cryst. Growth* **2005**, *282*, 455.
- [392] M. Steiger, *J. Cryst. Growth* **2005**, *282*, 470.
- [393] R. J. Flatt, M. Steiger, G. W. Scherer, *Environ. Geol.* **2007**, *52*, 187.
- [394] P. Xie, J. J. Beaudoin, *Cement Concrete Res.* **1992**, *22*, 631.
- [395] D. H. Everett, *Trans. Faraday Soc.* **1961**, *57*, 1541.
- [396] K. S. Pitzer, *Ionic Interaction Approach: Theory and Data Correlation*, CRC Press, Boca Raton **1991**.
- [397] J. Desarnaud, D. Bonn, N. Shahidzadeh, *Sci. Rep.* **2016**, *6*, 23.
- [398] A. Naillon, P. Joseph, M. Prat, *Phys. Rev. Lett.* **2018**, *120*, 34502.
- [399] K. Sekine, A. Okamoto, K. Hayachi, *Am. Mineral.* **2011**, *96*, 1012.
- [400] A. Royne, D. K. Dysthe, *J. Cryst. Growth* **2012**, *346*, 89.
- [401] L. Li, F. Kohler, A. Røyne, D. C. Dysthe, *Crystals* **2017**, *7*, 316.
- [402] D. A. Robinson, R. B. G. Williams, *Earth Surf. Processes Landforms* **2000**, *25*, 1309.
- [403] M. Steiger, S. Asmussen, *Geochim. Cosmochim. Acta* **2008**, *72*, 4291.
- [404] R. J. Flatt, F. Caruso, A. M. A. Sanchez, G. W. Scherer, *Nat. Commun.* **2014**, *5*, 4823.
- [405] A. S. Goudie, *Earth Surface Processes Landforms* **1986**, *11*, 275.
- [406] M. Schiro, E. Ruiz-Agudo, C. Rodriguez-Navarro, *Phys. Rev. Lett.* **2012**, *109*, 265503.
- [407] S. Siegesmund, A. Török, A. Hüpers, C. Müller, W. Klemm, *Environ. Geol.* **2007**, *52*, 385.
- [408] I. Sunagawa, *Bull. Mineral.* **1981**, *104*, 81.
- [409] J. Desarnaud, N. Shahidzadeh, H. Derluyn, V. Cnudde, L. Molari, S. De Miranda, *J. Appl. Phys.* **2015**, *118*, 114901.
- [410] H. Eloukabi, N. Sghaier, S. Ben Nasrallah, M. Prat, *Int. J. Heat Mass Transfer* **2013**, *56*, 80.
- [411] R. W. Lieferrink, A. Naillon, D. Bonn, M. Prat, N. Shahidzadeh, *Lab Chip* **2018**, *18*, 1094.
- [412] J. R. A. Godinho, K. M. Gerke, A. G. Stack, P. D. Lee, *Sci. Rep.* **2016**, *6*, 33086.
- [413] J. M. Bray, E. G. Lauchnor, G. D. Redden, R. Gerlach, Y. Fujita, S. L. Codd, J. D. Seymour, *Environ. Sci. Technol.* **2017**, *51*, 1562.
- [414] W. Song, T. W. de Haas, H. Fadaei, D. Sinton, *Lab Chip* **2014**, *14*, 4382.

- [415] A. Rufai, J. Crawshaw, *Phys. Fluids* **2017**, *29*, 126603.
- [416] M. Kim, A. Sell, D. Sinton, *Lab Chip* **2013**, *13*, 2508.
- [417] J. B. Laurindo, M. Prat, *Chem. Eng. Sci.* **1998**, *53*, 2257.
- [418] F. Li, D. P. Josephson, A. Stein, *Angew. Chem., Int. Ed.* **2011**, *50*, 360.
- [419] U. Gasser, *J. Phys.: Condens. Matter* **2009**, *21*, 203101.
- [420] V. J. Anderson, H. N. W. Lekkerkerker, *Nature* **2002**, *416*, 811.
- [421] A. Yethiraj, *Soft Matter* **2007**, *3*, 1099.
- [422] M. A. Boles, M. Engel, D. V. Talapin, *Chem. Rev.* **2016**, *116*, 11220.
- [423] T. Wang, D. LaMontagne, J. Lynch, J. Q. Zhuang, Y. C. Cao, *Chem. Soc. Rev.* **2013**, *42*, 2804.
- [424] F. Bai, D. S. Wang, Z. Y. Huo, W. Chen, L. P. Liu, X. Liang, C. Chen, X. Wang, Q. Peng, Y. D. Li, *Angew. Chem., Int. Ed.* **2007**, *46*, 6650.
- [425] J. Lacava, P. Born, T. Kraus, *Nano Lett.* **2012**, *12*, 3279.
- [426] B. de Nijs, S. Dussi, F. Smalenburg, J. D. Meeldijk, D. J. Groenendijk, L. Filion, A. Imhof, A. van Blaaderen, M. Dijkstra, *Nat. Mater.* **2015**, *14*, 56.
- [427] M. I. Bodnarchuk, L. Li, A. Fok, S. Nachtergaele, R. F. Ismagilov, D. V. Talapin, *J. Am. Chem. Soc.* **2011**, *133*, 8956.
- [428] F. K. Bian, L. Y. Sun, L. J. Cai, Y. Wang, Y. T. Wang, Y. J. Zhao, *Small* **2020**, *16*, 1903931.
- [429] H. Lowen, *J. Phys.: Condens. Matter* **2009**, *21*, 474203.
- [430] A. Reinmuller, E. Oguz, R. Messina, H. Lowen, H. J. Schope, T. Palberg, *Eur. Phys. J. Spec. Top.* **2013**, *222*, 3011.
- [431] H. Lowen, E. C. Oguz, L. Assoud, R. Messina, in *Advances in Chemical Physics*, Vol. 148 (Eds: S. A. Rice, A. R. Dinner), Wiley-Blackwell, Malden **2012**, p. 225.
- [432] V. N. Manoharan, M. T. Elsesser, D. J. Pine, *Science* **2003**, *301*, 483.
- [433] S. Naser, C. Bechinger, P. Leiderer, T. Palberg, *Phys. Rev. Lett.* **1997**, *79*, 2348.
- [434] E. G. Teich, G. van Anders, D. Klotsa, J. Dshemuchadse, S. C. Glotzer, *Proc. Natl. Acad. Sci. USA* **2016**, *113*, E669.
- [435] P. Pieranski, L. Strzelecki, B. Pansu, *Phys. Rev. Lett.* **1983**, *50*, 900.
- [436] A. Fortini, M. Dijkstra, *J. Phys.: Condens. Matter* **2006**, *18*, L371.
- [437] A. B. Fontecha, H. J. Schope, H. Konig, T. Palberg, R. Messina, H. Lowen, *J. Phys.: Condens. Matter* **2005**, *17*, S2779.
- [438] D. Zanaga, F. Bleichrodt, T. Altantzis, N. Winckelmans, W. J. Palenstijn, J. Sijbers, B. de Nijs, M. A. van Huis, A. Sanchez-Iglesias, L. M. Liz-Marzan, A. van Blaaderen, K. J. Batenburg, S. Bals, G. Van Tendeloo, *Nanoscale* **2016**, *8*, 292.
- [439] K. H. Kuo, *Struct. Chem.* **2002**, *13*, 221.
- [440] E. G. Noya, J. P. K. Doye, D. J. Wales, A. Aguado, *Eur. Phys. J. D* **2007**, *43*, 57.
- [441] J. W. Wang, C. F. Mbah, T. Przybilla, B. A. Zubiri, E. Spiecker, M. Engel, N. Vogel, *Nat. Commun.* **2018**, *9*, 5259.
- [442] A. L. Mackay, *Acta Crystallogr.* **1962**, *15*, 916.
- [443] D. Wang, M. Hermes, R. Kotni, Y. T. Wu, N. Tasios, Y. Liu, B. de Nijs, E. B. van der Wee, C. B. Murray, M. Dijkstra, A. van Blaaderen, *Nat. Commun.* **2018**, *9*, 2228.
- [444] B. Berkowitz, I. Dror, S. K. Hansen, H. Scher, *Rev. Geophys.* **2016**, *54*, 930.
- [445] Q. R. Xiong, T. G. Baychev, A. P. Jivkov, *J. Contam. Hydrol.* **2016**, *192*, 101.
- [446] S. Bals, S. Van Aert, G. Van Tendeloo, *Curr. Opin. Solid State Mater. Sci.* **2013**, *17*, 107.
- [447] P. Ercius, O. Alaidi, M. J. Rames, G. Ren, *Adv. Mater.* **2015**, *27*, 5638.
- [448] R. Leary, P. A. Midgley, J. M. Thomas, *Acc. Chem. Res.* **2012**, *45*, 1782.
- [449] A. M. Wise, J. N. Weker, S. Kalirai, M. Farmand, D. A. Shapiro, F. Meirer, B. M. Weckhuysen, *ACS Catal.* **2016**, *6*, 2178.
- [450] F. Pfeiffer, *Nat. Photonics* **2018**, *12*, 9.
- [451] A. P. Hitchcock, *J. Electron Spectrosc. Relat. Phenom.* **2015**, *200*, 49.
- [452] C. E. Hughes, P. A. Williams, K. D. M. Harris, *Angew. Chem., Int. Ed.* **2014**, *53*, 8939.
- [453] C. E. Hughes, P. A. Williams, B. M. Kariuki, K. D. M. Harris, *ChemPhysChem* **2018**, *19*, 3341.
- [454] J. J. De Yoreo, N. A. J. M. Sommerdijk, *Nat. Rev. Mater.* **2016**, *1*, 16035.
- [455] G. M. Zhu, H. Reiner, H. Colfen, J. J. De Yoreo, *Micron* **2019**, *118*, 35.
- [456] W. D. Kaplan, Y. Kauffmann, *Annu. Rev. Mater. Res.* **2006**, *36*, 1.
- [457] C. M. Fang, H. Men, Z. Fan, *Metall. Mater. Trans. A* **2018**, *49*, 6231.
- [458] K. Voitchovsky, D. Giofre, J. J. Segura, F. Stellacci, M. Ceriotti, *Nat. Commun.* **2016**, *7*, 9.
- [459] A. O. F. Jones, B. Chattopadhyay, Y. H. Geerts, R. Resel, *Adv. Funct. Mater.* **2016**, *26*, 2233.
- [460] J. N. Israelachvili, *Intermolecular and Surface Forces*, Academic Press, Waltham, MA, USA **1985**.
- [461] C. D. Dimitrakopoulos, A. R. Brown, A. Pomp, *J. Appl. Phys.* **1996**, *80*, 2501.
- [462] R. Ruiz, D. Choudhary, B. Nickel, T. Toccoli, K. C. Chang, A. C. Mayer, P. Clancy, J. M. Blakely, R. L. Headrick, S. Iannotta, G. G. Malliaras, *Chem. Mater.* **2004**, *16*, 4497.
- [463] H. Chung, Y. Diao, *J. Mater. Chem. C* **2016**, *4*, 3915.
- [464] S. C. B. Mannsfeld, A. Virkar, C. Reese, M. F. Toney, Z. N. Bao, *Adv. Mater.* **2009**, *21*, 2294.
- [465] M. Yoneya, M. Kawasaki, M. Ando, *J. Phys. Chem. C* **2012**, *116*, 791.